



저작자표시-비영리-변경금지 2.0 대한민국

이용자는 아래의 조건을 따르는 경우에 한하여 자유롭게

- 이 저작물을 복제, 배포, 전송, 전시, 공연 및 방송할 수 있습니다.

다음과 같은 조건을 따라야 합니다:



저작자표시. 귀하는 원저작자를 표시하여야 합니다.



비영리. 귀하는 이 저작물을 영리 목적으로 이용할 수 없습니다.



변경금지. 귀하는 이 저작물을 개작, 변형 또는 가공할 수 없습니다.

- 귀하는, 이 저작물의 재이용이나 배포의 경우, 이 저작물에 적용된 이용허락조건을 명확하게 나타내어야 합니다.
- 저작권자로부터 별도의 허가를 받으면 이러한 조건들은 적용되지 않습니다.

저작권법에 따른 이용자의 권리는 위의 내용에 의하여 영향을 받지 않습니다.

이것은 [이용허락규약\(Legal Code\)](#)을 이해하기 쉽게 요약한 것입니다.

[Disclaimer](#)

공학박사학위논문

산화환원 반응 설계를 통한
전이금속 산화물의 산화상태 제어의
광전기화학적 에너지 변환 응용

CONTROL OF OXIDATION STATE OF TRANSITION METAL
OXIDES BY DESIGNING REDOX REACTION FOR
PHOTOELECTROCHEMICAL ENERGY CONVERSION

2018년 8월

서울대학교 대학원

재료공학부

강 호 영

ABSTRACT

Control of Oxidation State of Transition Metal Oxides by Designing Redox Reaction for Photoelectrochemical Energy Conversion

Ho-Young Kang

Department of Materials Science and Engineering

The Graduate School

Seoul National University

Transition metals have various oxidation states because they have electrons in the d-orbital, which has small energy differences. Therefore, transition metals have the redox property that electrons can easily be lost and obtained. These metals can also bond with various anions, forming oxides, nitrides and sulfides with various compositions showing various material properties. Especially, transition metal oxides are widely used for photoelectrochemical catalyst because they show various band structures according to the oxidation states. The oxidation states in transition metal oxides is crucial for the selectivity and the activity of catalyst because they are related to the potential of photogenerated electrons, which is determined by the position of energy band. Among the photoelectrochemical energy conversion reactions, the CO₂ reduction reaction is greatly affected by the electron potential of photogenerated electrons for its selectivity and efficiency. Because, in performing the reduction of CO₂ in an aqueous condition, which is the requirement of mimicking natural photosynthesis process, the reduction of

CO₂ has to compete with the hydrogen evolution reaction. Making the CO₂ reduction more dominant was difficult because the rate-determining step of CO₂ reduction has a higher redox potential than that of hydrogen evolution reaction, which requires the precise control of active materials.

The objective of this thesis is precisely controlling the oxidation state of transition metal oxide to selectively perform the photoelectrochemical CO₂ reduction and designing the nanostructure to optimize the activity and stability of active materials.

Firstly, 1-D nanostructured mono-phase Cu₂O nanofiber photocathode for selective photoelectrochemical CO₂ reduction was fabricated using electrospinning method and thermodynamically programmed calcination. The phase of Cu₂O nanofiber should be precisely controlled to mono-phase without the impurity phase as CuO to selectively perform the photoelectrochemical CO₂ reduction over hydrogen evolution reaction. Until now, the atmosphere during the calcination process was not precisely controlled either oxidative atmosphere by atmospheric pressure, or reductive atmosphere by Ar or H₂ gas resulting mixing with CuO. The phase of copper oxide nanofibers was controlled by the nanoscale gas-solid reaction considering thermodynamics and kinetics. The driving force of the phase transformation between the different oxidation states of copper oxide is calculated by comparing the Gibbs free energy of each of the oxidation states. From the calculation, the kinetically processable window for the fabrication of Cu₂O in which mono-phase Cu₂O can be fabricated in a reasonable reaction time scale is discovered. Also, a hierarchical structure of Cu₂O thin film underlayer and TiO₂ passivation layer is developed to optimize the photoactivity and stability of Cu₂O nanofiber electrode. By controlling the oxidation state of copper oxide nanofiber electrode and designing the appropriate nanostructure, a faradic efficiency of 93% for CO₂ conversion to alcohol was achieved in an aqueous media.

The second focus is to control oxidation state in nanostructured hematite (α -Fe₂O₃) and to develop hierarchically structured photoanode for effective oxygen evolution reaction (OER), which is the counter reaction of photoelectrochemical CO₂ reduction. One of the most important challenges of hematite photoanode for water oxidation is the improvement of the electrical conductivity. To date, the conventional approach to overcome the drawback has been to identify heterogeneous dopants. We systematically controlled oxygen vacancy as a new intrinsic dopant source and investigated the interplay with external dopant, such as tin (Sn). Based on this understanding, we demonstrate that controlled generation of oxygen vacancies can activate the photoactivity of hematite significantly. Also we developed hierarchical structure that consists of undoped Fe₂O₃ underlayer, Ti-doped Fe₂O₃ nanorod, β -FeOOH overlayer to optimize the photoactivity of hematite. Undoped hematite underlayer negatively shifted the onset potential by 40 mV (0.84 V vs. RHE) and β -FeOOH overlayer enhanced the photocurrent density to 1.83 mA cm⁻² at 1.4 V vs. RHE.

This study provides useful information for understanding the methodology to precisely control the oxidation state of transition metal oxide and rational design of nanostructured electrodes, and their effects on activity and selectivity of photoelectrochemical reactions.

Keywords: CO₂ reduction, water oxidation, cuprous oxide, iron oxide, thermodynamic calculation, phase control, hierarchical structure, nanostructure

Student Number: 2012-24154

Table of Contents

Abstract.....	i
Table of contents.....	iv
List of Tables.....	viii
List of Figures.....	ix

Chapter 1. Introduction

1.1. Materials for photoelectrochemical CO ₂ reduction	1
1.2. Phase and structural issues of photoelectrode materials	6
1.2.1. Cu ₂ O photocathodes for CO ₂ reduction	6
1.2.2. Fe ₂ O ₃ photoanodes for water oxidation	12
1.3. Objective of the thesis	16
1.4. Organization of the thesis	20

Chapter 2. Theoretical Background

2.1. Semiconductor photoelectrochemistry	21
2.1.1. Energy band and Fermi level	21
2.1.2. Semiconductor/electrolyte interface	26
2.1.3. Potential distributions at the interface	30

2.1.4. Photoelectrochemical process	38
2.1.5. Recombination of carriers	44
2.2. Photoelectrochemical CO ₂ reduction	50
2.2.1. Theory of photoelectrochemical CO ₂ reduction	50
2.2.2. Summary of CO ₂ reduction catalyst and performances	53
2.3. Photoelectrochemical water oxidation	56
2.3.1. Theory of photoelectrochemical water oxidation	56
2.3.2. Trends in water oxidation activity of catalyst	60

Chapter 3. Experimental Procedures

3.1. Sample preparation	63
3.1.1. Fabrication of Cu ₂ O photocathode	63
3.1.2. Fabrication of Fe ₂ O ₃ photoanode	65
3.2. Photoelectrochemical analysis	68
3.3. Microstructural and chemical analysis	70

Chapter 4. Design and Fabrication of Cu₂O Nanofiber Photocathode

4.1. Introduction	71
4.2. Fabrication of mono-phase Cu ₂ O nanofiber	75
4.2.1. Optimization of the electrospinning process	75
4.2.2. Design of the reaction path	81
4.2.3. Design of the reaction parameter	85
4.3. Fabrication of the hierarchical structure	94
4.3.1. Optimization of Cu ₂ O thin film underlayer	95

4.3.3. Optimization of TiO ₂ passivation layer	98
4.4. Summary	107

Chapter 5. Photoelectrochemical performance of Cu₂O photocathode

5.1. Introduction	108
5.2. Photoelectrochemical performances	109
5.2.1. Effects of Cu ₂ O thin film underlayer	109
5.2.2. Effects of TiO ₂ passivation layer	112
5.2.3. Effects of the phase of copper oxide	119
5.3. Summary	128

Chapter 6. Generation of Oxygen Vacancies in Fe₂O₃ Photoanode

6.1. Introduction	129
6.2. Characterization of spray-coated Fe ₂ O ₃ films	132
6.2.1. Microstructure of Fe ₂ O ₃ films	132
6.2.2. Phase of Fe ₂ O ₃ films during annealing	135
6.3. Effects of oxygen vacancy generation on photoactivity	138
6.3.1. Generation of oxygen vacancy	138
6.3.2. Interplay with the external dopant	140
6.3.3. Effects on photoelectrochemical performance	144
6.4. Summary	156

Chapter 7. Development of Hierarchically Structured Fe₂O₃ Photoanode

7.1. Introduction	157
-------------------	-----

7.2. Fabrication of hierarchically nanostructured Fe ₂ O ₃	161
7.3. Effects of hierarchical structure on photocurrent density	168
7.4. Effects of β-FeOOH on charge transfer kinetics	175
7.4.1. Investigation of the transient photocurrent	175
7.4.2. Analysis by electrochemical impedance spectroscopy	178
7.5. Summary	181

Chapter 8. Conclusion

8.1. Summary of Results	182
8.2. Future work and suggested research	185

References	186
Abstract (In Korean)	206
Curriculum Vitae	209

LIST OF TABLES

- Table 2.1** Summary of CO₂ reduction photocatalyst materials and corresponding performances.
- Table 4.1** SEM micrograph of (A) cross-section of FTO substrate coated with precursor solution, and (B) electrospun nanofiber on the substrate.
- Table 4.2** Comparison between calculated equilibrium chemical potential of oxygen for the phase transformation of CuO to Cu₂O and Cu₂O to Cu.
- Table 7.1** Donor density and flat band potential from Mott-Schottky plot.

LIST OF FIGURES

- Figure 1.1** (A) Schematic for photoelectrochemical cell that reduces CO₂ into methanol at a photocathode, and oxidizes water to oxygen at a photoanode. (B) Z-scheme of photoelectrochemical cell coupled by photoanode and photocathode.
- Figure 1.2** Energy band positions of material candidates for the photocathode and photoanode.
- Figure 1.3** (A) Phase diagram of Cu-O system showing compound of copper and oxygen: CuO and Cu₂O. (B) Crystal structure of Cu₂O and CuO; pink balls indicate Cu, and red balls indicate O.
- Figure 1.4** Band diagram of CuO and Cu₂O showing that Cu₂O could perform CO₂ reduction reaction whereas CuO prefers hydrogen evolution reaction.
- Figure 1.5** Scheme for the typical process of fabrication of nanostructured Cu₂O. Nanostructured Cu₂O is highly metastable and difficult to be fabricated as mono-phase.
- Figure 1.6** Schematics for the advantages of nanostructured electrode.
- Figure 1.7** Drawbacks of Cu₂O photocathode and overcoming strategy for the photoelectrochemical CO₂ reduction.
- Figure 1.8** The unit cell of hematite showing the octahedral face-sharing Fe₂O₉ dimers forming chains in the c direction. A detailed view of one Fe₂O₉ dimer the Fe³⁺ cations produce long (light grey) and short (dark grey) Fe-O bonds.

- Figure 1.9** Polaron hopping conduction mechanism in hematite. Electron is transported as the form of Fe^{2+}
- Figure 1.10** Drawbacks of Fe_2O_3 photoanode and overcoming strategy for the photoelectrochemical water oxidation.
- Figure 1.11** Drawbacks of Fe_2O_3 photoanode and overcoming strategy for the photoelectrochemical water oxidation.
- Figure 2.1** (A) Density of states (DOS) for a typical semiconductor. (B) Parabolic approximation near band edges. (C) Simplified band diagram used in this chapter.
- Figure 2.2** Band diagrams for intrinsic and doped semiconductors, showing the position of the Fermi level.
- Figure 2.3** Band diagrams for n-type semiconductor/metal and n-type semiconductor/electrolyte.
- Figure 2.4** Distribution of charge, electrical field, electrical potential, and band energies showing the depletion condition that is developed when an n-type semiconductor is brought into contact with a redox electrolyte with a lower Fermi level.
- Figure 2.5** Formation of the electron double layer at the interface between the semiconductor and electrolyte. The Helmholtz layer and the potential distribution is demonstrated.
- Figure 2.6** Schematic Mott-Schottky plots for the same material doped p-type and n-type. It shows how the flat band potentials are related to the Fermi energies and the band energies.

- Figure 2.7** Diode behavior of the n-type semiconductor/redox electrolyte junction in the dark. The junction blocks electron flow from right to left under reverse bias, but passes an electron current from left to right as forward bias reduces band bending.
- Figure 2.8** Splitting of the Fermi energies brought about by illumination in n-type semiconductor. The Fermi energy of the minority carriers (holes) is strongly affected by illumination, whereas the Fermi energy of majority carriers remains the same.
- Figure 2.9** Characteristic length scales considered in the derivation of the Gartner equation. W_{SC} is the width of the space charge region and $1/\alpha$ is the wavelength dependent penetration depth of the incident light.
- Figure 2.10** Current-voltage curves for an n-type semiconductor in the dark and under illumination. The photocurrent for the illuminated electrode was calculated using the Gartner equation. The dark current increases exponentially with forward bias. At open circuit in the dark, the electrode potential is determined by the equilibrium potential of the redox system. Under illumination, the open circuit potential is determined by the condition $j = 0$. The change in potential brought about by illumination corresponds to the photovoltage.
- Figure 2.11** Delayed onset of photocurrent arising from recombination, either in the space charge region or at the surface. j_G is the current predicted by the Gartner equation, j_{photo} is the experimental photocurrent, and j_{rec} is the recombination current.

- Figure 2.12** Scheme of kinetic that describes the competition between charge transfer and surface recombination.
- Figure 2.13** Normalized plots of transient photocurrent and corresponding surface hole concentration for $k_{tr} = k_{rec}$. The exponential decay time constant $(k_{tr} + k_{rec})^{-1}$ and the ratio of the steady state current to the spike $= k_{tr}/(k_{tr} + k_{rec})$, allowing k_{tr} and k_{rec} to be determined.
- Figure 2.14** Band edge positions of various semiconductors relative to the redox potentials at pH 1 of compounds involved in CO₂ reduction.
- Figure 2.15** CO₂ reduction mechanism following (A) formaldehyde route, (B) carbene route, and (C) glyoxal route.
- Figure 2.16** Schematic plot of the Gibbs free energy of the reactive species and intermediates in the oxygen evolution reaction versus the reaction coordinate. Solid lines indicate the energetics of a real catalyst and dotted lines indicate that of an ideal catalyst.
- Figure 2.17** Schematic plot of the Gibbs free energy of the reactive species and intermediates in the oxygen evolution reaction versus the reaction coordinate. Solid lines indicate the energetics of a real catalyst and dotted lines indicate that of an ideal catalyst.
- Figure 2.18** Schematic plot of the Gibbs free energy of the reactive species and intermediates in the oxygen evolution reaction versus the reaction coordinate. Solid lines indicate the energetics of a real catalyst and dotted lines indicate that of an ideal catalyst.

- Figure 3.1** Schematic illustration of fabrication process of mono-phase Cu_2O nanofiber with hierarchical structure consists of Cu_2O thin film underlayer and TiO_2 passivation layer.
- Figure 3.2** (A) Schematic for the process of spray pyrolysis that fabricates nanostructured Fe_2O_3 electrode. (B) Novel annealing process to effectively generate the oxygen vacancies in the hematite photoanode.
- Figure 3.3** The procedure to fabricate a hierarchically structured hematite photoanode using hydrothermal synthesis.
- Figure 4.1** Four strategies to optimize the adhesion of nanofiber to the FTO substrate. The ineffective strategy and the effective strategy were divided into red box and blue box.
- Figure 4.2** SEM micrograph of (A) ITO nanorods (B) Ni foams, showing vertical and porous nanostructure, respectively. Delamination of nanofiber from the (C) ITO nanorods and (D) Ni foams.
- Figure 4.3** SEM micrograph of (A) cross-section of FTO substrate coated with precursor solution, and (B) electrospun nanofiber on the substrate.
- Figure 4.4** Photograph of nanofiber on FTO glass with varying the solvent of an electrospinning solution.
- Figure 4.5** Photograph of nanofiber on FTO glass with varying the electrospinning time from 30 s to 10 min. 5 min of electrospinning showed optimum thickness.
- Figure 4.6** Ellingham diagram that shows the oxidation tendency of a phase according to the temperature and the chemical potential of oxygen.

The reaction paths of transforming as-spun nanofibers into mono-phase Cu_2O are demonstrated.

- Figure 4.7** Morphology of nanofiber after calcination by three reaction paths: (A) direct oxidation path, (B) reduction/oxidation path, and (C) oxidation/reduction path. Only at the oxidation/reduction path, the uniform copper oxide nanofiber structure is formed.
- Figure 4.8** Heat treatment profile of calcination of as-spun nanofiber according to the reaction paths; red line, blue line, and green line indicates oxidation/reduction path, direct oxidation path, and reduction/oxidation path, respectively.
- Figure 4.9** Diagram of chemical potential of oxygen showing the stable regions of CuO , Cu_2O , and Cu , according to the temperature. The experimental conditions of oxygen partial pressure are indicated.
- Figure 4.10** Diagram of chemical potential of oxygen showing the stable regions of CuO , Cu_2O , and Cu , according to the temperature. The experimental conditions of oxygen partial pressure are indicated.
- Figure 4.11** XRD pattern of copper oxides that are annealed at $500\text{ }^\circ\text{C}$ for 3 hours at $p\text{O}_2$ of $250\text{ }\mu\text{Torr}$, $50\text{ }\mu\text{Torr}$, $10\text{ }\mu\text{Torr}$, and $1\text{ }\mu\text{Torr}$. Fraction of phases are quantified by Rietveld analysis.
- Figure 4.12** XRD pattern for the CuO nanofibers which are annealed at (A) $1\text{ }\mu\text{Torr}$, (B) $10\text{ }\mu\text{Torr}$, (C) $50\text{ }\mu\text{Torr}$, and (D) $250\text{ }\mu\text{Torr}$ for 1 – 12 hours, respectively.
- Figure 4.13** Transformation curve of reduction of CuO nanofiber according to the $p\text{O}_2$ of $250\text{ }\mu\text{Torr}$, $50\text{ }\mu\text{Torr}$, $10\text{ }\mu\text{Torr}$, and $1\text{ }\mu\text{Torr}$ at $500\text{ }^\circ\text{C}$

showing the kinetically processable window of mono-phase Cu_2O fabrication.

- Figure 4.14** Calculation of the Gibbs free energy of CuO , Cu_2O and Cu according to the $p\text{O}_2$ of 50 μTorr , 10 μTorr , and 1 μTorr at 500 °C, indicating the driving force of phase transformation which is the difference in the Gibbs free energy between copper oxides.
- Figure 4.15** Schematic of the hierarchical structure of the Cu_2O nanofiber.
- Figure 4.16** Morphology of the Cu_2O underlayer with respect to the thickness of (A) 0 nm, (B) 20 nm, (C) 50nm, and (D) 100nm.
- Figure 4.17** Phase of the Cu_2O underlayer with respect to the thickness of 20 nm to 100 nm.
- Figure 4.18** (A) SEM micrograph of the photocathode. (B) TEM image of the Cu_2O nanofiber after depositing 5 nm of TiO_2 by ALD. Diffraction pattern for (C) Cu_2O nanofiber and (D) TiO_2 passivation layer.
- Figure 4.19** (A) HAADF image of Cu_2O nanofiber with TiO_2 passivation layer. Image of EDS mapping of TiO_2 -coated Cu_2O nanofiber. (B) Electron image, (C) mapping for Cu, and (D) mapping for Ti.
- Figure 4.20** Raman spectrum of a TiO_2 -coated nanofiber with varying annealing temperatures from 400 °C to 500 °C. The crystallization of TiO_2 begin at 450 °C.
- Figure 4.21** Morphology of nanofiber with post-annealed TiO_2 layer. Thickness of TiO_2 and annealing temperatures are varied from 2 nm – 10 nm and 400 °C – 500 °C, respectively.
- Figure 4.22** (A) X-ray photoelectron spectroscopy (XPS) profile for the Cu_2O nanofiber coated with 5 nm TiO_2 , which was annealed at 450 °C for

1 hour at pO_2 of 10 μ Torr. (B) Phase of the electrode before and after the post-annealing of TiO_2 passivation layer; both showing monophase Cu_2O .

Figure 4.23 X-ray photoelectron spectroscopy (XPS) profile for the Cu_2O nanofiber coated with 5 nm TiO_2 , which was annealed at 450 °C for 1 hour at pO_2 of 10 μ Torr. It shows Ti^{3+} state which is the active site for CO_2 reduction.

Figure 4.24 Band diagram of the Cu_2O/TiO_2 system equilibrated at 0.4 V vs. RHE with different thickness of the TiO_2 passivation layer. (A) Cu_2O nanofiber passivated with 5 nm thick TiO_2 , and (B) with 30 nm thick TiO_2 .

Figure 4.25 UV-visible spectra for the CuO and Cu_2O nanofiber showing band gaps of 1.57 eV and 2.46 eV, respectively for the CuO and Cu_2O .

Figure 5.1 The effect of the underlayer on the photocurrent density. Underlayer enhances photoactivity of the nanofiber by blocking the electron leakage.

Figure 5.2 Photocurrent density curve for the 20 nm and 100 nm thick Cu_2O underlayer. Both film effectively blocks the electron leakage from FTO.

Figure 5.3 Photocurrent density curve for the 20 nm and 100 nm thick Cu_2O underlayer. Both film effectively blocks the electron leakage from FTO.

Figure 5.4 Photocurrent density curve for the thickness variation of TiO_2 passivation layer. TiO_2 with 5 nm thickness showed best performances.

- Figure 5.5** GIXRD pattern of Cu_2O electrode with 5 nm TiO_2 passivation layer before and after bulk electrolysis at 0.4 V vs. RHE.
- Figure 5.6** Faradic efficiency for the 5-nm TiO_2 coating and 30-nm TiO_2 coating on Cu_2O nanofiber.
- Figure 5.7** Equivalent circuit model for the photocathode.
- Figure 5.8** Nyquist plot for bare Cu_2O nanofiber, Cu_2O nanofiber with 5 nm TiO_2 overlayer, and Cu_2O nanofiber with 30 nm TiO_2 overlayer.
- Figure 5.9** Mott-Schottky plot for the $\text{Cu}_2\text{O}/\text{TiO}_2$ system with different thickness of the TiO_2 passivation layer.
- Figure 5.10** X-ray photoelectron spectroscopy (XPS) depth profile of $\text{TiO}_2/\text{Cu}_2\text{O}$ electrode after post-annealing according to the thickness of TiO_2 ; 5 nm, and 30 nm.
- Figure 5.11** Photoelectrochemical performances for the Cu_2O photocathode: photocurrent density curve according to the phase of copper oxides.
- Figure 5.12** Photocurrent density curve of CuO annealed at high vacuum, showing low photoactivity due to the interfering of light absorption by Cu .
- Figure 5.13** Plots of the photocurrent density for previously reported data of CO_2 reduction and H_2 evolution by Cu_2O photoelectrode. Black solid line indicates CO_2 reduction, black dotted line indicates H_2 evolution, and red solid line indicates CO_2 reduction by this paper.
- Figure 5.14** Gas Chromatography (GC) spectra after bulk electrolysis by mono-phase Cu_2O electrode.
- Figure 5.15** Nuclear Magnetron Resonance (NMR) spectra after bulk electrolysis by mono-phase Cu_2O electrode.

- Figure 5.16** Faradic efficiency for the CO₂ reduction and the water reduction after bulk electrolysis at 0.4 V vs. RHE with the Cu₂O/TiO₂ system with TiO₂ thicknesses of 5 nm and 30 nm, and according to the phase of the copper oxides.
- Figure 5.17** (A) Band diagram of CuO with 5 nm TiO₂ overlayer. (B) Mott-schottky plot for bare CuO nanofiber and CuO with 5 nm TiO₂ overlayer.
- Figure 5.18** Partial current density for the major products of the CO₂ reduction by the mono-phase Cu₂O electrode. Inset is the faradic efficiency according to the applied bias.
- Figure 6.1** The aerosol spray pyrolysis method for the preparation of hematite films.
- Figure 6.2** SEM images of (A) the FTO substrate and the hematite films formed by the spraying of an FeCl₃ solution with a volume of (B) 30 ml, (C) 60 ml, and (D) 90 ml. (E) Cross-sectional SEM of hematite films formed by the spraying of the 90ml-solution.
- Figure 6.3** X-ray diffraction (XRD) spectra of hematite films after thermal reduction and oxidative annealing under various oxygen partial pressure.
- Figure 6.4** Annealing process and ambients for pO₂-controlled annealing and for normal annealing. Photographs for reduced magnetite films prepared from the different precursors and after vacuum annealing: FeCl₃, Fe(acac)₃, and Fe(NO₃)₃
- Figure 6.5** (A) XPS spectra of hematite films after thermal reduction and oxidative annealing under various pO₂. (B) The area values for the

Fe²⁺ satellite peak (715.7 eV) are normalized to the value for the reduced film under high vacuum..

- Figure 6.6** (A) Electrical conductance of post-annealed hematite films on quartz substrate with various Sn-concentration. (B) Schematic diagram that demonstrates the effects of doping and of pO_2 on the electrical conductivity of post-annealed hematite films.
- Figure 6.7** (A) Photocurrent density-voltage curves of a hematite film after pO_2 -controlled annealing under simulated solar illumination (solid line) and in the dark (dashed line), respectively. (B) Photocurrent density at 1.6 V vs. RHE for undoped hematite as a function of pO_2 .
- Figure 6.8** XPS spectra measured from the as-coated hematite (red) and from the hematite after thermal reduction and oxidative annealing at ambient air (black)
- Figure 6.9** (A) Photocurrent density-voltage curves for Sn-doped hematite films and (B) photocurrent density at 1.6 V vs. RHE as a function of the doping concentration after pO_2 -controlled annealing in ambient air (solid line, full markers) and for after normal annealing (dash-dotted line, empty markers).
- Figure 6.10** Photocurrent density at 1.6 V vs. RHE for hematite films as a function of the Sn concentration after pO_2 -controlled annealing under various pO_2 atmospheres. Inset: Enlarged graph situated between 0 ~ 1 at.% of Sn concentration.
- Figure 6.11** Photocurrent curves for various hematite films.

- Figure 6.12** Optical property of hematite films in the various pO_2 and Sn concentration, which shows the absorption coefficient as a function of wavelength.
- Figure 6.13** Photocurrent density for 1at.-%-Sn-doped hematite film annealed at ambient air in various amount of precursor solution. Inset: photographs for hematite photoanode prepared by ASP using 30 ml, 50 ml, 70 ml, and 90 ml of precursor solution.
- Figure 6.14** Photocurrent onset potential for hematite films as a function of the Sn concentration after pO_2 -controlled annealing under various pO_2 atmospheres.
- Figure 7.1** (A), (B) Scheme for a photoanode that consists of Ti-doped hematite nanorod arrays, an undoped hematite underlayer, and β -FeOOH-branched nanorods for a catalyst. (C) Cross-sectional images from the scanning electron microscope (SEM) for the photoanode with nanostructured triple layers that was synthesized by hydrothermal synthesis.
- Figure 7.2** SEM top-view images of the hydrothermal-synthesized (A) undoped hematite underlayer, (B) Ti-doped hematite nanorods, and (C) β -FeOOH-branched nanorods. (D) SEM cross-sectional image of the Ti-doped hematite nanorods. (E) TEM image of the β -FeOOH-branched nanorods and (F) a higher resolution image.
- Figure 7.3** XPS spectra for (A) Fe2p, (B) Ti2p, and (C) O1s cores for undoped (black lines) and Ti-doped (red lines) hematite.
- Figure 7.4** XRD patterns of β -FeOOH and hematite synthesized using hydrothermal method. The black line indicates hematite that has a

preferred orientation of (110), and the red line indicates β -FeOOH that has a (211) orientation. The green dots indicate peaks from the FTO substrate.

Figure 7.5 SEM images of hydrothermally synthesized hematite nanorods after additional hydrothermal synthesis for 50 min.

Figure 7.6 (A) Plots of the photocurrent for the undoped hematite nanorod array, DH, U/DH and U/DH/A with respect to the applied potential on the electrode. The photocurrent from the hematite film prepared by spray pyrolysis (dash-dotted line) is presented to show the effect of nanostructuring. (B) Current density for DH, U/DH, and U/DH/A measured in the dark.

Figure 7.7 Mott-Schottky plot of DH, U/DH, U/DH/A, and undoped hematite nanorods measured under dark condition.

Figure 7.8 Absorbance of DH, U/DH, and U/DH/A from UV-visible spectroscopy.

Figure 7.9 *J-E* curve during the chopping illumination for (A) without β -FeOOH catalyst branches and (B) with β -FeOOH catalyst branches. The *J-E* curves under constant illumination (red dashed line) and in the dark (green dash-dotted line) during the linear sweep are indicated. The transient curve of the photocurrent when the light is turned on and turned off at (C) 1.03 V vs. RHE and (D) 1.23 V vs. RHE.

Figure 7.10 (A) Equivalent circuit for a hematite photoanode in aqueous electrolyte. Nyquist plots for DH, U/DH, and U/DH/A at (B) 1.03 V and (C) 1.23 V vs. RHE. (D) R_s (black symbols), R_{rec} (red symbols),

and R_{ss} (blue symbols); (E) C_{ss} values; (F) Mott-Schottky plots from C_{bulk} for DH (closed square), U/DH (opened circle), and U/DH/A (half-opened diamond).

CHAPTER 1

Introduction

1.1. Materials for photoelectrochemical CO₂ reduction

As economies and energy demand are rapidly growing in the past decades, global warming has been regarded as the serious problem of future generation that causes the climate change and ocean acidification [1.1, 2]. To reduce greenhouse gas by sustainable energy source, photoelectrochemical cell (PEC) which is one of a solar energy conversion system has been intensively investigated over decades [1.3]. PEC mimics Z-scheme in natural photosynthesis process by coupling photocathode of p-type semiconducting material and photoanode of n-type semiconducting material [1.4].

Figure 1.1 A shows the schematic for photoelectrochemical cell that performs the photoelectrochemical CO₂ reduction reaction. At a photocathode, CO₂ is reduced to other value-added carbon compounds such as carbon monoxide, methane, and methanol, etc [1.5]. The reaction is proceeded by photogenerated electrons at a photocathode and the electron potential of photogenerated electrons are related to the selectivity and activity of reactions [1.6]. At a photoanode, water is oxidized to O₂, which is the counter reaction of CO₂ reduction, by the photogenerated holes at the photoanode. Also,

Chapter 1: Introduction

photogenerated holes at a photocathode and photogenerated electrons at a photoanode are recombined through an external circuit (displayed as ohmic contact in Figure 1.1 B). Operating the cell without an external bias is an ideal case, however, the overpotentials at the surfaces of photoelectrodes and slow reaction kinetics requires an external bias at the external circuit. To minimize the overpotentials at the electrodes and supply electrons with high electron potential at the photoelectrode, materials at the photoelectrode should be chosen carefully.

In Figure 1.2, the energy band positions of material candidates for the photoelectrode are displayed [1.7]. A material that has negative conduction band edge position is suitable for the photocathode, and that has positive valence band edge position is suitable for the photoanode to satisfy Z-scheme. Photogenerated electrons with high electron potential at the photocathode are able to perform reducing electrochemical reaction with small overpotential and photogenerated holes with low electron potential at the photoanode are able to perform oxidizing electrochemical reaction with small overpotential. Also, the materials for the photoelectrode should have small band gap energy that can utilize the visible light of sunlight spectrum because most portion of the solar light is irradiated to earth as visible light while the portion of ultraviolet light is only 8 %.

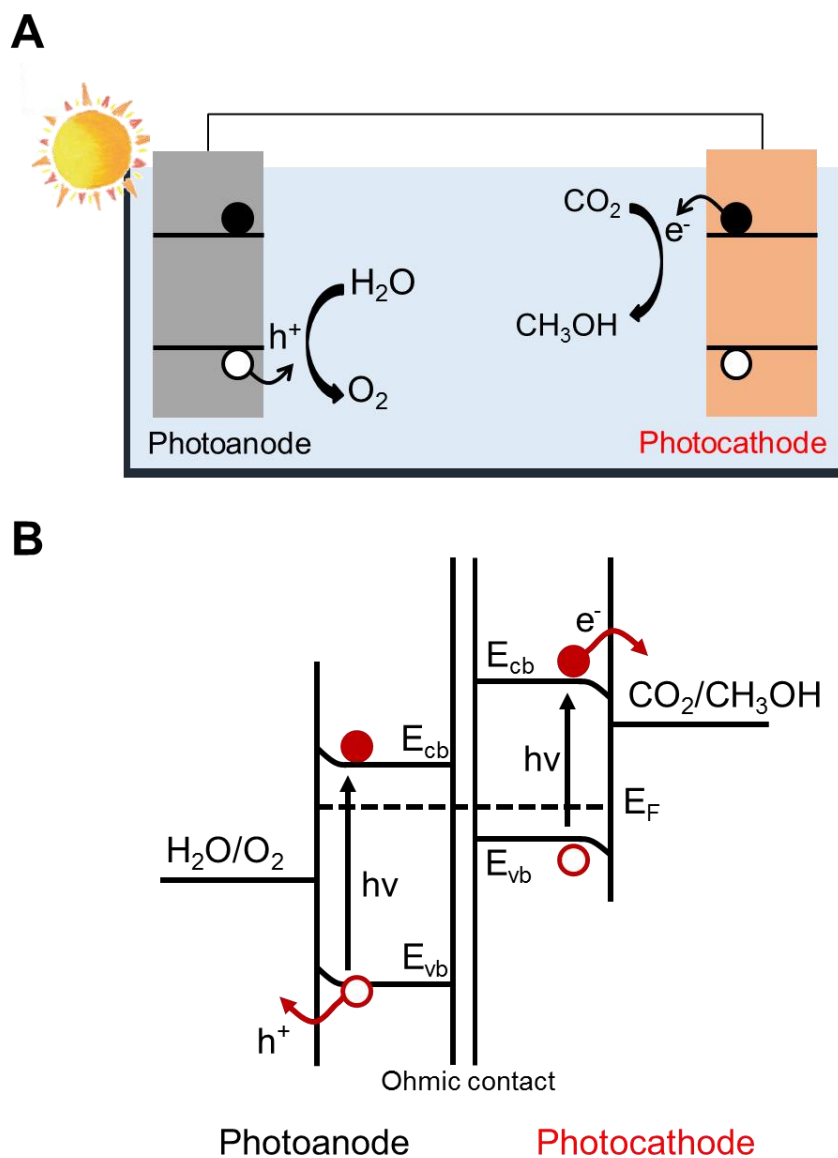


Figure 1.1 (A) Schematic for photoelectrochemical cell that reduces CO_2 into methanol at a photocathode, and oxidizes water to oxygen at a photoanode. (B) Z-scheme of photoelectrochemical cell coupled by photoanode and photocathode.

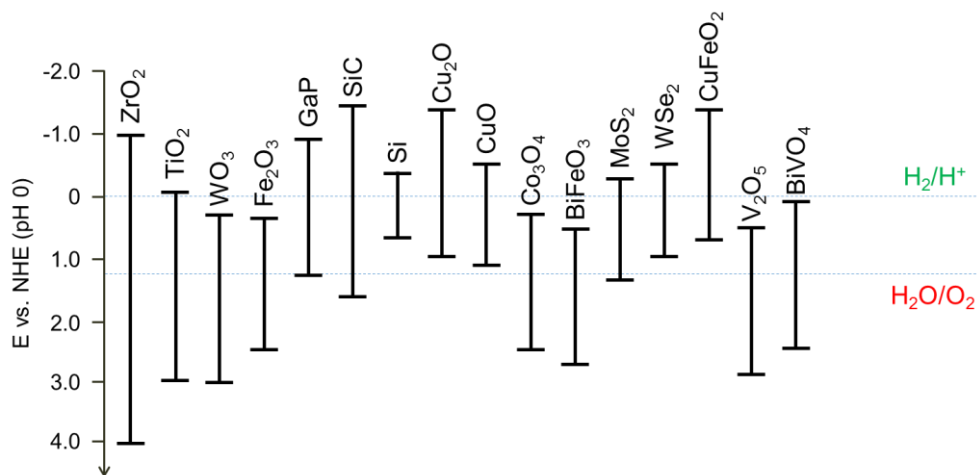


Figure 1.2 Energy band positions of material candidates for the photocathode and photoanode.

Transition metal oxides are commonly used as photoelectrode due to their semiconducting characteristics, processability, and abundances [1.8]. Among numerous candidates, we have studied the Cu₂O as a photocathode, and Fe₂O₃ as a photoanode. Cu₂O has received considerable attention as a photocathode for photoelectrochemical CO₂ reduction because Cu₂O has a band gap of approximately 2.4 eV that can utilize the visible light of the sunlight spectrum and has a negative conduction band edge position, which generates high energy photogenerated electrons, and moreover, it is earth-abundant and non-toxic, which makes it environmentally friendly [1.9]. Also, iron is one of the most abundant elements on the earth and can be processed or recycled via environmentally benign methods. In nature, iron readily exists as oxides, which have been regarded as useless materials. However, hematite (α -Fe₂O₃), the most common form of iron oxide, has recently attracted attention for photoelectrochemical water oxidation as a

photoanode material due to its small bandgap of approximately 2.0 eV that can absorb visible light and its excellent chemical stability in aqueous solutions [1.10].

Although these materials satisfy the selection rules of photoelectrode, however, the materials cannot perform photoelectrochemical CO₂ reduction itself without an external bias though we put the photocathode and photoanode together [1.8]. Because many factors limit the photoactivity such as the small diffusion length of minority carrier *i. e.*, electrons in p-type photocathode and holes in n-type photoanode, absorption length of photoelectrode, and reaction kinetics at the surface.

Therefore, it is important to control the oxidation state of material precisely to optimize the photoactivity and selectivity of reaction since it is the property of material itself, and to design the structure of electrode because it could enhance the carrier transport property and light absorption by external modification.

Following sections describe the details of recently rising issues in terms of microstructure, phase and overview of novel designing strategies for electrodes suggested by the thesis for high performance PEC.

1.2. Phase and structural issues of photoelectrode materials

1.2.1. Cu₂O photocathodes for CO₂ reduction

Transition metal oxides are typically used as photoelectrode, however, most of the materials are n-type due to the oxygen vacancies they have naturally. Copper oxide has been used as a photocathode for photoelectrochemical reaction by its p-type semiconducting character [1.11, 12]. As shown in the phase diagram of Cu and O (Figure 1.3), copper oxide mainly exists as two forms; cupric oxide (CuO) and cuprous oxide (Cu₂O) [1.13]. CuO has a monoclinic structure with the band gap of approximately 1.4 eV, and Cu₂O has a cubic structure with the band gap of approximately 2.4 eV [1.7].

Although Cu₂O has negative conduction band edge position, and small band gap that can utilize the visible light, however, in CO₂ reduction by Cu₂O, few studies are reported in an aqueous electrolyte, and the studies observed low selectivity [1.14-16], which is mainly because the Cu₂O photocathode is usually mixed with other impurity phases such as CuO and Cu [1.12, 14-18]. As can be seen in Figure 1.4, when the Cu₂O phase is mixed with the CuO phase, CO₂ reduction is less favored because photogenerated electrons located at the conduction band edge of Cu₂O can overcome the activation energy barrier of the CO₂ reduction while that of CuO cannot [1.7]. Also, the Cu impurity phase would interfere the light absorption of Cu₂O if the Cu is present at the surface, and could cause electron leakage from the current collector if the conduction path from current collector to the electrolyte is formed by Cu.

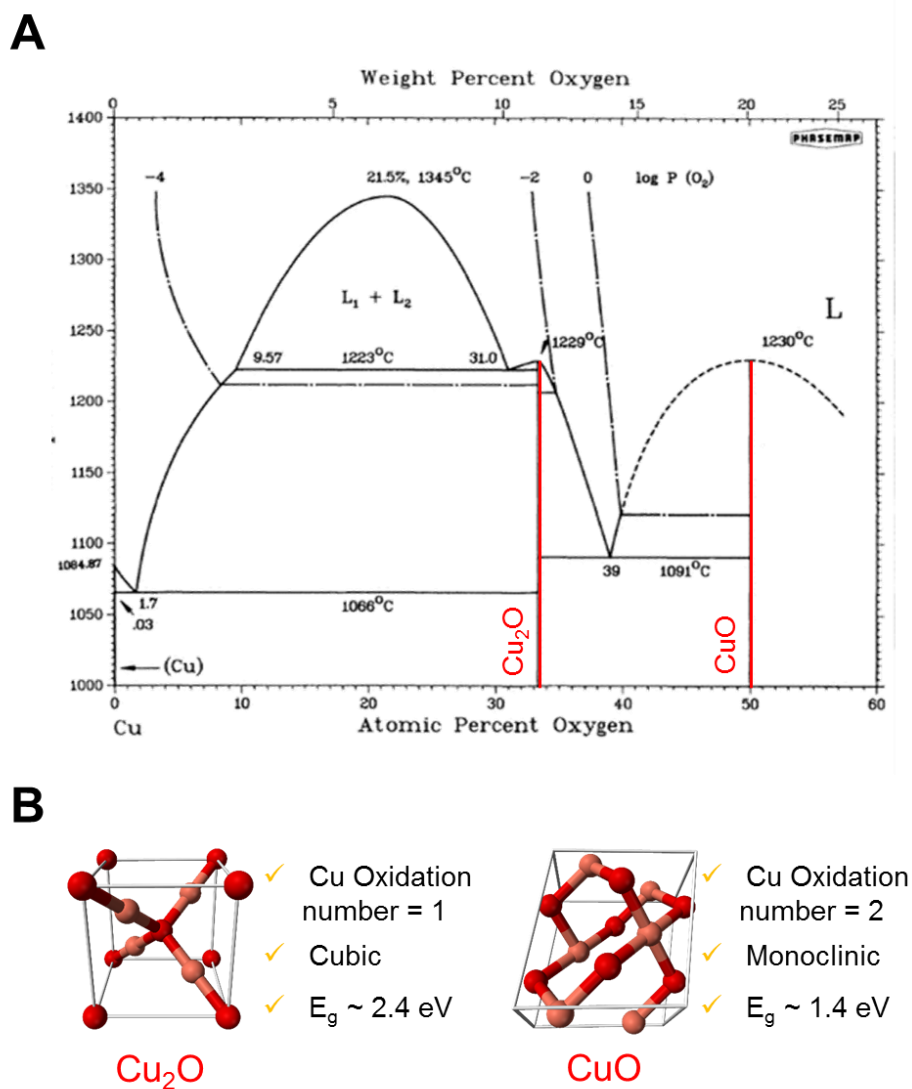


Figure 1.3 (A) Phase diagram of Cu-O system showing compound of copper and oxygen: CuO and Cu₂O. (B) Crystal structure of Cu₂O and CuO; pink balls indicate Cu, and red balls indicate O.

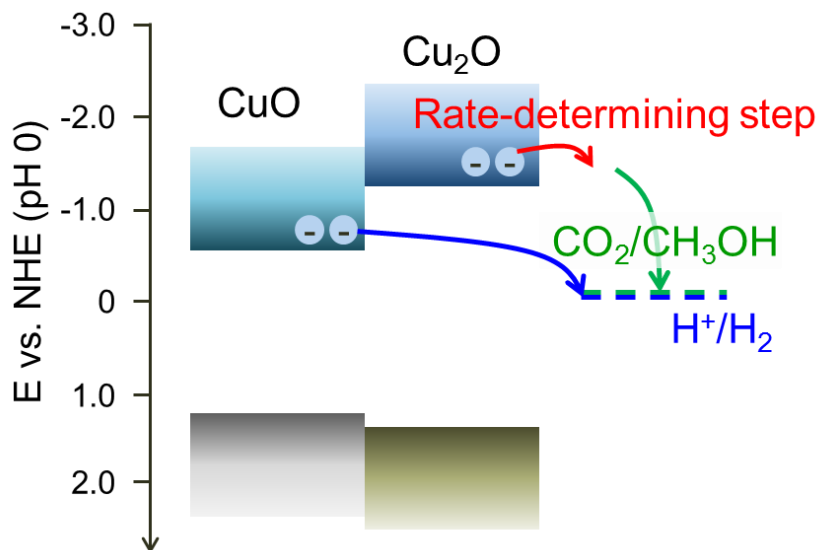


Figure 1.4 Band diagram of CuO and Cu₂O showing that Cu₂O could perform CO₂ reduction reaction whereas CuO prefers hydrogen evolution reaction.

Therefore, fabrication of an electrode with mono-phase Cu₂O is necessary to achieve high selectivity for CO₂ reduction. However, precise control of the oxidation state of copper oxide is difficult because the apparent activation energies of reduction of CuO and Cu₂O are similar [1.19, 20]. Generally, the Cu₂O nanostructure is fabricated by reducing nanostructured CuO or oxidizing nanostructured Cu. However, the redox atmosphere was controlled only at atmospheric pressure or an inert gas atmosphere, such as Ar, and was not systematically controlled, which resulted in the phase mixing with CuO or metallic Cu [1.11, 12]. In the conventional reducing condition, the reduction of CuO to Cu₂O occurs, as well as the reduction of Cu₂O to Cu also occurs simultaneously [1.21], and in the oxidation process, Cu oxidizes not only to Cu₂O but also to CuO [1.22].

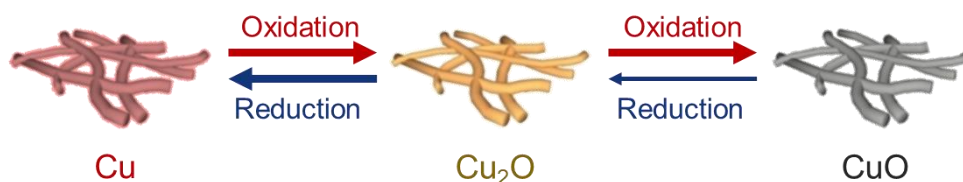


Figure 1.5 Scheme for the typical process of fabrication of nanostructured Cu₂O. Nanostructured Cu₂O is highly metastable and difficult to be fabricated as mono-phase.

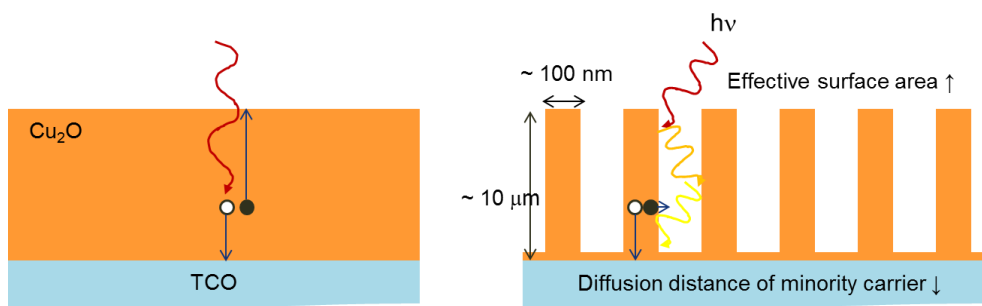


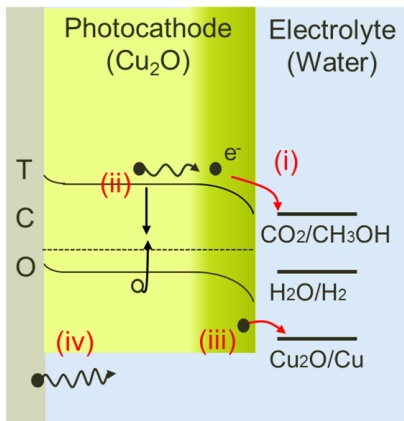
Figure 1.6 Schematics for the advantages of nanostructured electrode.

Besides the difficulty of fabrication of nanostructured Cu₂O, the nanostructure is essential for efficient CO₂ reduction because nanostructure increases effective surface area of electrode and reduces diffusion distance of minority carrier (Figure 1.6). The diffusion length of minority carrier in the Cu₂O was reported to 20 – 100 nm [1.23-25] and it is incommensurate with the light absorption depth near the bandgap which is approximately 10 μm [1.23, 26, 27]. Therefore, the electrode should have the nanostructure with the feature size of about 100 nm that the minority carriers can diffuse

to the interface with the electrolyte.

Although the nanostructured Cu_2O having mono-phase is successfully fabricated, there are several problems in applying the nanostructured Cu_2O to an actual PEC system. First, the fluorine-doped tin oxide (FTO) substrate should not be directly exposed to the electrolyte. When the FTO is directly exposed to the electrolyte, it shunts the device, resulting in leakage of electrons from the substrate, which degrades the photoactivity of the photoelectrode [1.12]. Therefore, FTO should be fully covered with the active material to prevent the leakage of electrons. Second, the Cu_2O is not stable in the reducing environment because the reduction potential of Cu_2O to metallic Cu is more negative than that of the CO_2 reduction [1.23]. Therefore, passivation of the Cu_2O electrode from the electrolyte is required to prevent the Cu_2O from being reduced to Cu instead of CO_2 reduction on Cu_2O .

In summary, in the Cu_2O photocathode for photoelectrochemical CO_2 reduction, Cu_2O should be present as mono-phase without other impurity phases of other oxidation states of copper to selectively perform the CO_2 reduction over hydrogen evolution reaction. The mono-phase Cu_2O should be nanostructured to absorb sufficient light while ensuring the diffusion length of minority carriers. Also, the Cu_2O should be passivated to inhibit the photocorrosion to metallic Cu, and the FTO should all be covered to prevent the direct contact with the electrolyte, which causes the electron leakage.



- Reaction selectivity for CO_2 (i)
→ Achieve mono-phase Cu_2O
- Short diffusion length of electron (ii)
→ Fabricate nanofiber structure
- Photocorrosion of Cu_2O (iii)
→ Passivate electrode with TiO_2
- Electron leakage from FTO (iv)
→ Deposit Cu_2O underlayer

Figure 1.7 Drawbacks of Cu_2O photocathode and overcoming strategy for the photoelectrochemical CO_2 reduction.

1.2.2. Fe₂O₃ photoanodes for water oxidation

The iron and oxygen atoms in hematite arrange in the corundum structure, which is trigonal-hexagonal scalenohedral (class $\bar{3}2/m$) with space group R-3c, lattice parameters $a=0.5036$ nm, $c=1.3749$ nm, and six formula units per unit cell. In the hematite crystal, O²⁻ are arranged in a hexagonal closed-packed lattice along the [001] direction [1.10]. The cations (Fe³⁺) occupy the two-thirds of the octahedral interstices in the (001) basal planes and the tetrahedral sites remain unoccupied. For the cations, FeO₆ octahedra that share edges with three neighboring octahedra in the same plane and one face with an octahedron in an adjacent plane in the [001] direction [1.28].

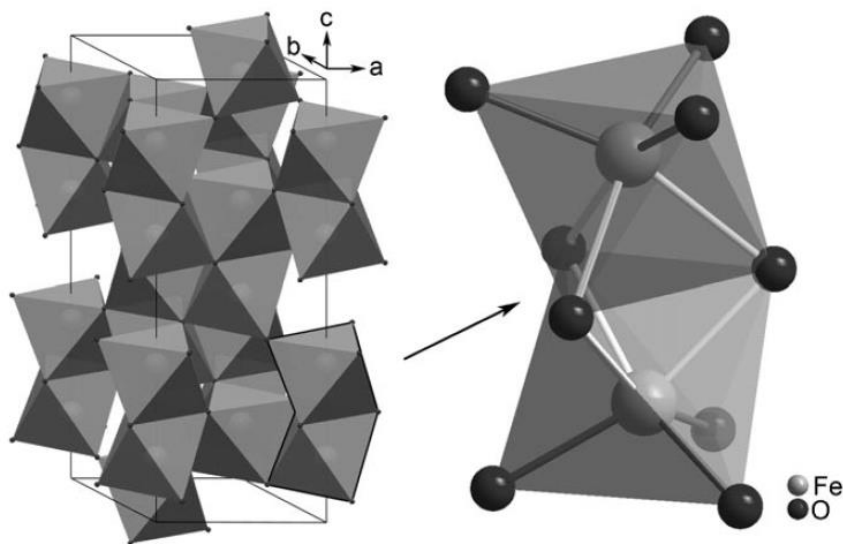
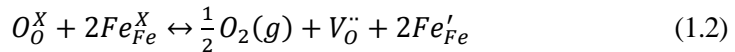
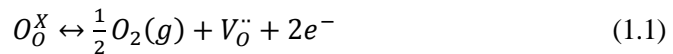


Figure 1.8 The unit cell of hematite showing the octahedral face-sharing Fe₂O₉ dimers forming chains in the c direction. A detailed view of one Fe₂O₉ dimer the Fe³⁺ cations produce long (light grey) and short (dark grey) Fe-O bonds [1.28].

The arrangement of the oxygen anions and the high-spin (d^5) cations affect the orientation of the spin magnetic moment of iron atoms and the spin configuration of iron influence the carrier transport properties of hematite [1.29]. The efficient transport of majority charge carriers to the current collector is one of the main requirement to be used as a photoanode. However, the polycrystalline hematite has extremely low electrical conductivities of $10^{-14} \Omega^{-1} \text{cm}^{-1}$ [1.30], conduction electron concentrations of 10^{18}cm^{-3} at 1000 K, and electron mobility of $10^2 \text{cm}^2 \text{V}^{-1} \text{s}^{-1}$ [1.31].

Therefore, the improvement of the electrical conductivity of hematite is an important challenge and it was improved by adding impurities that act as dopants. The p-type and n-type dopants were both studied such as Mg^{2+} , Cu^{2+} (p-type) and Ti^{4+} , Sn^{4+} , Si^{4+} (n-type) [1.32]. Other than the impurity atoms, intrinsic defect in hematite can also act as an electron donor and it could give further increase of conductivity to the externally doped hematite. When an oxygen vacancy is generated in the hematite, it gives two electrons by the ionization of the defect (Equation 1.1). The electrons are observed as the Fe^{2+} form because the conduction of hematite is proceeded by the hopping of electrons through the iron atoms (Equation 1.2). There are some systematic studies on the extrinsic doping of hematite, but the effect of intrinsic doping is not systematically studied as well as the synergistic effect with the extrinsic doping.



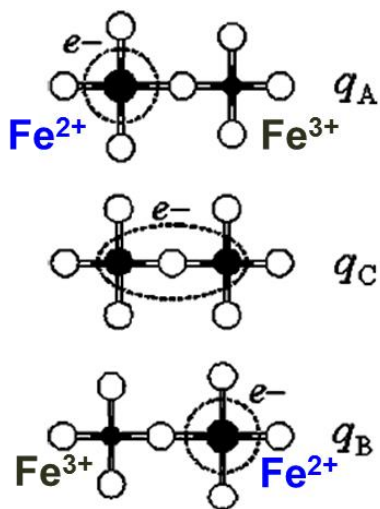


Figure 1.9 Polaron hopping conduction mechanism in hematite. Electron is transported as the form of Fe^{2+} [1.33].

In addition to the conduction of majority charge carriers, the minority charge carriers should also be effectively transported to the interface with the electrolyte. The diffusion length of minority carriers in pure hematite is several nanometers due to the extremely short lifetime of photogenerated holes [1.34]. Therefore, nanostructuring of hematite is essential because 400-500 nm thickness is needed for the complete light absorption [1.35, 36], which is far greater than the diffusion length of minority carriers. Furthermore, the oxygen evolution kinetics at the surface of Fe_2O_3 is usually very slow and transported minority carriers could be trapped at a surface state. Therefore, to facilitate the OER, surface treatment or co-catalyst is necessary.

Also, the electron cloud of the FTO substrate extends into the Fe_2O_3 film and thus enhances recombination, which is called as electron back injection [1.10]. It positively shifts the onset potential of the photoanode and to prevent the electron back injection,

underlayer between the Fe_2O_3 active material and the FTO substrate, that can block the electron cloud of the FTO substrate is necessary.

In summary, in the Fe_2O_3 photoanode for photoelectrochemical water oxidation, Fe_2O_3 should be doped by extrinsic and intrinsic dopants to improve majority carrier conductivity. The structure of hematite should be nanosize because the diffusion length of electron is extremely short due to the short lifetime of photogenerated holes. The surface of Fe_2O_3 should be treated to eliminate the surface trap sites or co-catalyst should be adopted to enhance the sluggish OER kinetics. Also, the electron cloud of FTO substrate recombines with the photogenerated holes in the Fe_2O_3 , which requires the underlayer to block the electron back injection from FTO substrate (Figure 1.10).

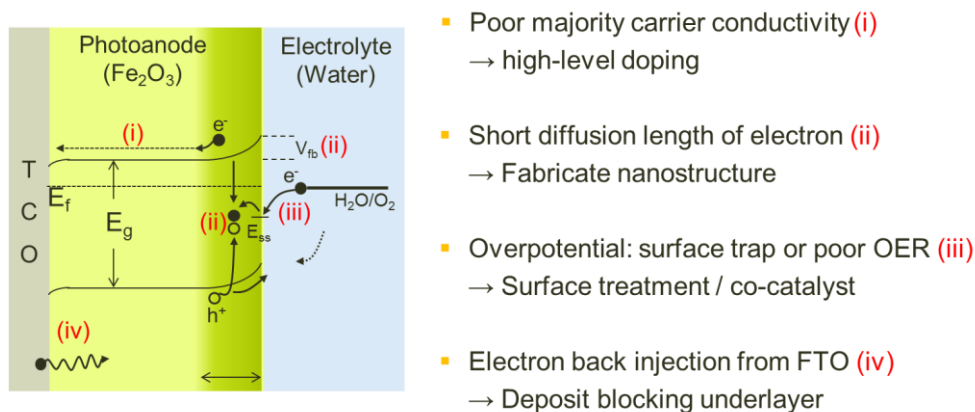


Figure 1.10 Drawbacks of Fe_2O_3 photoanode and overcoming strategy for the photoelectrochemical water oxidation.

1.3. Objective of the thesis

Photoelectrochemical cell could mimic the Z-scheme of natural photosynthesis process by fabricating appropriate photocathode and photoanode materials. Transition metal oxide is generally used as photoelectrode because of its semiconducting character. Considering the energy band position, earth abundancy, and toxicity, Cu_2O and Fe_2O_3 are selected as the photocathode and the photoanode, respectively. However, these materials have various problems as mentioned in the previous section, which act as drawbacks to be used as photoelectrochemical CO_2 reduction device without any external power sources except the solar light.

To improve the photoelectrochemical performance, precise control of oxidation state of transition metal oxide was essential because the defects and the phase of transition metal oxides are controlled by the oxidation state. However, the process and methodology to precisely control the oxidation state of transition metal oxide have not been developed. In the conventional calcination process to control the oxidation state of a material, oxidizing atmosphere was controlled to the atmospheric pressure and the reducing atmosphere was controlled to the inert gas as Ar or reactive gas as H_2 . The precise control or systematic control of oxidation state was not possible through this rough control of gas atmosphere during calcination process. Moreover, the processing parameter of calcination was adjusted through piecemeal method as trial and error not predicted through the calculations considering reaction thermodynamics.

The objective of this thesis is to provide the methodology of precisely controlling the oxidation state of transition metal oxide and structural design of photoelectrode for improving the performances.

The first focus is developing the mono-phase Cu_2O nanofiber photocathode with hierarchical structure for photoelectrochemical CO_2 reduction. Copper oxide nanofiber structure with diameters of approximately 100 nm secures the diffusion distance of the photogenerated minority carriers to the electrolyte and provides high effective surface area. The nanofiber is fabricated through the electrospinning process, which is simple and can be applied to mass production. The phase of copper oxide nanofiber is precisely controlled to mono-phase Cu_2O by predictive synthesis process based on thermodynamic calculations. We compared Gibbs free energy of each oxidation state of copper according to the chemical potential of oxygen, *i. e.*, the oxygen partial pressure during calcination process. Through the calculation, we derived the thermodynamic and kinetic processing parameters and reaction path to fabricate mono-phase Cu_2O nanofiber. Especially, mono-phase Cu_2O was successively fabricated at the condition where Cu_2O is thermodynamically metastable. Although the Cu_2O is thermodynamically metastable, we discovered the kinetically processable window of fabricating Cu_2O , a condition that Cu_2O kinetically maintains its phase. After fabricating Cu_2O mono-phase nanofiber, a hierarchical structure with the Cu_2O thin film underlayer and TiO_2 passivation layer was developed to be used as photocathode system. The Cu_2O thin film underlayer is adopted to block electron leakage from FTO substrate, and the TiO_2 passivation layer is deposited to prevent the photocorrosion of Cu_2O into Cu. The Cu_2O underlayer dramatically improved the photocurrent density of Cu_2O nanofiber electrode, which showed poor photoactivity without the underlayer due to the electron leakage from FTO. Also, the TiO_2 passivation layer significantly improved the photostability of Cu_2O which reduces to metallic Cu in reducing environment. By applying all of the above, we finally succeeded in reducing CO_2 to alcohol in aqueous electrolyte with the faradic efficiency of 93 % by hierarchically structured mono-phase Cu_2O nanofiber.

The second focus is fabricating the nanostructured Fe_2O_3 photoanode and controlling its defects for the photoelectrochemical water oxidation. Vertical nanostructure of hematite could effectively transported photogenerated holes to the interface with the electrolyte, and the high level doping by synergistic effect of extrinsic and intrinsic doping effectively transported photogenerated electrons to the FTO substrate. To generate oxygen vacancies effectively, we designed the annealing path of hematite. Hematite electrode was first reduced to Fe_3O_4 phase, and then it was re-oxidized to hematite with controlled oxygen partial pressures. The post annealing process, which involves reduction step, is quite effective for increasing the carriers in hematite by increasing oxygen vacancy. Hematite annealed with ambient air showed extremely low photocurrent density, but with the new process, it showed dramatically increased value with 8 times or more. In the annealing process that does not involve reduction step, initial state is hematite (Fe_2O_3), but with reduction step, initial state becomes magnetite (Fe_3O_4), which made hematite films more oxygen deficit even when the films were oxidized. In controlling oxygen partial pressure, there was clear tendency that lower partial pressure made higher photoactivity. Lower oxygen partial pressure induced smaller oxidation number of Fe that made Fe^{2+} more favorable. Since the conduction mechanism of hematite is small polaron hopping through $\text{Fe}^{3+}/\text{Fe}^{2+}$ valence exchange, abundance of Fe^{2+} phase can enhance the conductivity. Especially, annealed at 0.05 mTorr showed photocurrent density of 1.2 mA/cm^2 , whereas annealed at ambient air showed that of 0.76 mA/cm^2 . In addition, hierarchical structures with the undoped Fe_2O_3 underlayer to block the electron back injection from FTO substrate and the $\beta\text{-FeOOH}$ co-catalyst overlayer to enhance the OER kinetics were developed. The undoped Fe_2O_3 underlayer reduced the onset potential about 40 mV from 0.88 V to 0.84 V vs. RHE and the $\beta\text{-FeOOH}$ co-catalyst overlayer improved the photocurrent at 1.23 V vs. RHE to 1.64 mA/cm^2 .

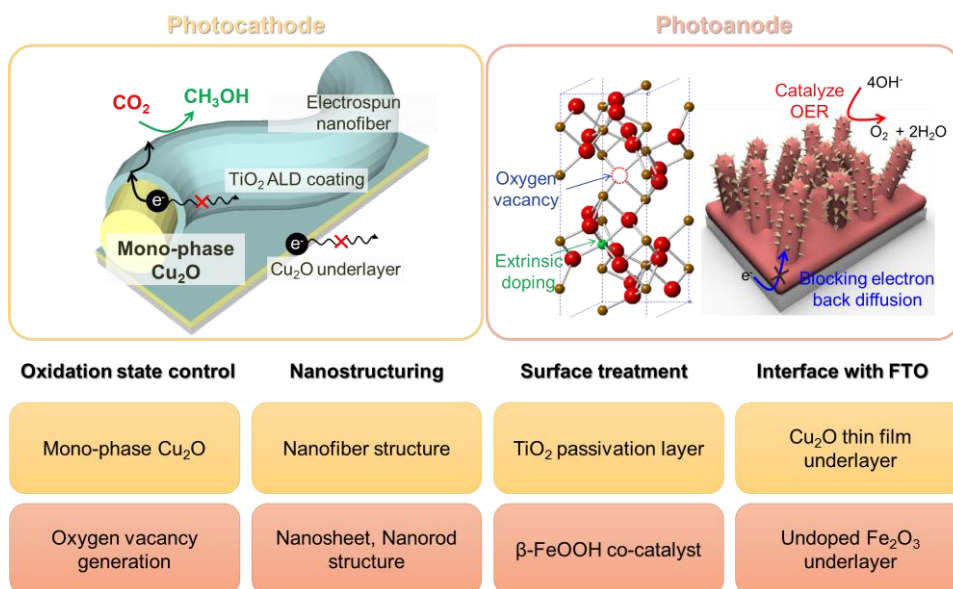


Figure 1.11 Drawbacks of Fe₂O₃ photoanode and overcoming strategy for the photoelectrochemical water oxidation.

1.4. Organization of the thesis

This thesis consists of eight chapters. The principles of photoelectrochemical reaction at the photocathode and photoanode by semiconducting materials are reviewed in Chapter 2. Chapter 3 describes the experimental procedures, including fabrication process, calculation of the thermodynamic parameters of calcination process, method for photoelectrochemical characterization and analyzing its products, microstructural characterization and investigation of oxidation state of materials. In Chapter 4, fabrication of mono-phase Cu_2O nanofiber is discussed. The reaction path of electrospun nanofiber is designed to maintain the nanofiber structure and the thermodynamic and the kinetic parameter of calcination is designed through thermochemical calculations. In that process, we have discovered the kinetically processable window of fabricating mono-phase Cu_2O nanofiber. In addition, we developed the hierarchical structure with the Cu_2O thin film underlayer and TiO_2 passivation layer to optimize the photoelectrochemical performances. Chapter 5 discusses the effect of phase of copper oxide and the effect of TiO_2 passivation layer on selectivity of photoelectrochemical CO_2 reduction. Chapter 6 discusses the effect of generation of oxygen vacancies on the photoactivity of Fe_2O_3 for the photoelectrochemical water oxidation, and chapter 7 discusses developing the hierarchical structures with undoped Fe_2O_3 underlayer and β - FeOOH co-catalyst overlayer, which further optimized the photoactivity of Fe_2O_3 . Chapter 8 summarizes this study and suggests a photocathode material for the photoelectrochemical CO_2 reduction, CuFeO_2 , which is stable p-type oxide in reducing environment.

CHAPTER 2

Theoretical background*

(*This chapter cited reference [2.1-3])

2.1. Semiconductor electrochemistry

Photoelectrochemical cell operates by the photogenerated carriers in the semiconductor, and thus energy band and the interface with the electrolyte mainly determines the potential of charge carriers that are used in the photoelectrochemical reaction.

In this section, fundamentals of energy bands of semiconductor, which is in contact with the electrolyte, and its electrochemical characteristics are reviewed.

2.1.1. Energy band and Fermi level

Semiconductors has continuous electron energy levels which are grouped into the valence band and conduction band, and there is a forbidden energy gap which is a group of energy levels that electrons cannot have between the valence and conduction energy bands. The density of states distributions corresponding to the valence and conduction bands are generally rather complicated functions of energy (Figure 2.1A), but near the

Chapter 2: Theoretical background

band edges they often approach the simple parabolic forms shown in Figure 2.1B. In this chapter, we will further simplify the band diagram for semiconductors to the form shown in Figure 2.1C. The critical energies are the energies of the conduction band and valence band edges, E_C and E_V , which also define the band gap energy $E_{gap} = E_C - E_V$. In general, the probability of occupation of electrons is defined by the Fermi-Dirac function $f(E)$ for a distribution of energy levels.

$$f(E) = \frac{1}{1 + \exp\left(\frac{E - E_F}{k_B T}\right)} \quad (2.1)$$

Where E_F is the Fermi energy, k_B is the Boltzmann constant, and T is the absolute temperature. It can be seen that for $E > E_F$, the occupation probability falls rapidly towards zero over an energy range of a few $k_B T$, whereas for $E < E_F$ it rises rapidly to 1. For $E = E_F$, the occupation probability is 0.5. The concentrations of electrons (n) and holes (p), which must be equal under pure semiconductor with no doping impurities can be expressed in terms of the Fermi-Dirac probability function.

$$n = \int_{E_C}^{\infty} D_C(E) f(E) dE \quad (2.2)$$

$$p = \int_{-\infty}^{E_V} D_V(E) [1 - f(E)] dE \quad (2.3)$$

$$np = N_C N_V \exp\left(-\frac{E_{gap}}{k_B T}\right) \quad (2.4)$$

Chapter 2: Theoretical background

Where D_C and D_V are the densities of states distributions, and N_C and N_V are the effective densities of states in the conduction band and valence band, respectively. The concentrations of electrons and holes are related by the mass balance equation (2.3).

However, in most cases, photoelectrodes are doped semiconductors of which the dopants are from the external sources or the internal sources. These contain donor (n-type doping) or acceptor (p-type doping) atoms (or vacancies) in the lattice that can produce electrons or holes according to the equilibria below.



The ionization energies for these reactions are generally of the order of $k_B T$, so that the free electron or hole concentrations at room temperature are determined by the doping level rather than by excitation of electrons across the bandgap. In this case, the Fermi energy is also determined by N_D or N_A , and if $n \ll N_C$ or $p \ll N_V$, the Fermi-Dirac function reduces to the Boltzmann function. Figure 2.2 contrasts an intrinsic semiconductor with n-type and p-type doped materials with the same bandgap.

$$n = N_C \exp\left(-\frac{E_C - E_F}{k_B T}\right) \quad p = N_V \exp\left(-\frac{E_F - E_V}{k_B T}\right) \quad (2.6)$$

The electrochemical potential of a charged species i is a partial molar quantity. It measures the way that the Gibbs energy G of a system changes when i is added to a phase that has an inner potential φ .

$$\bar{\mu}_i = \left(\frac{\partial \bar{G}}{\partial n_i} \right)_{T,P,n_j,\varphi} \quad (2.7)$$

Conceptually, the electrochemical potential can be splitted into components associated with the chemical species and its charge.

$$\bar{\mu}_i = \mu_i + z_i F \varphi \quad (2.8)$$

The first term is the chemical potential and the second term represents the electrical work done in transferring one mole of charge $z_i F$, where $z_i q$ is the total charge on the species i . The absolute value of the chemical potential of electrons, μ_n , is the work function, Φ . It represents the energy required to excite an electron from a bound state in the metal to a state corresponding to a free electron in vacuum. The chemical potential of electrons and holes depends on their concentration.

$$\mu_n = \mu_n^0 + k_B T \ln \frac{n}{N_C} \quad \mu_p = \mu_p^0 + k_B T \ln \frac{p}{N_V} \quad (2.9)$$

Where μ_n^0 and μ_p^0 are the standard chemical potentials of holes and electrons, and it can be seen from equation (2.9) that N_C and N_V correspond to the standard states for electrons and holes, respectively. Also, the electrochemical potentials of electrons and holes are related to the Fermi energy by below equations [2.4].

$$\bar{\mu}_n = E_F \quad \text{and} \quad \bar{\mu}_p = -E_F \quad (2.10)$$

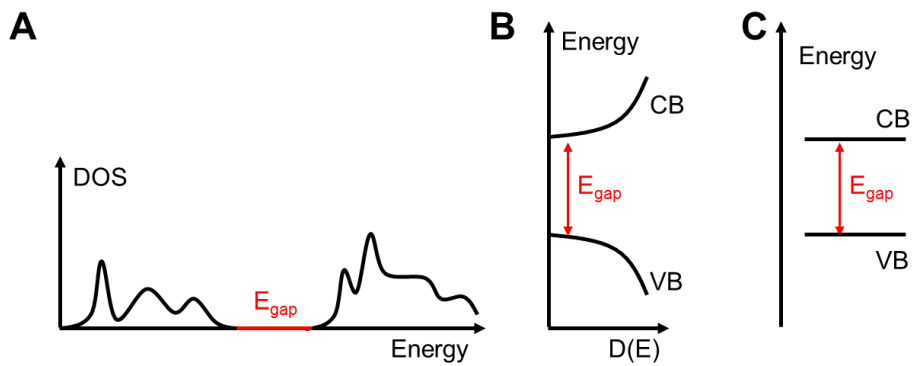


Figure 2.1 (A) Density of states (DOS) for a typical semiconductor. (B) Parabolic approximation near band edges. (C) Simplified band diagram used in this chapter.

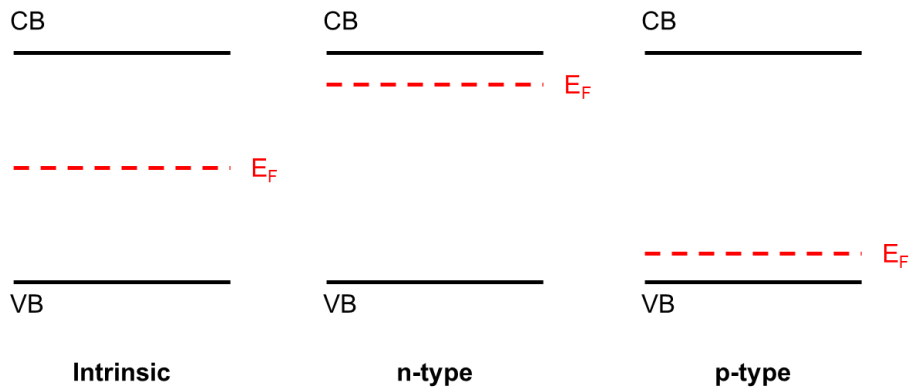


Figure 2.2 Band diagrams for intrinsic and doped semiconductors, showing the position of the Fermi level.

2.1.2. Semiconductor/electrolyte interface

Semiconductor junctions of different kinds are important in many types of electronic devices, including photoelectrochemical cells. The junction between semiconductor and the electrolyte could be understood by considering a semiconductor/metal junction as an example. If an n-type semiconductor is contacted by a metal with a higher work function, electrons will initially move from the semiconductor to the metal, generating a contact potential difference that establishes electronic equilibrium. The similar phenomenon happens at the semiconductor/electrolyte interface because the Fermi level of n-type semiconductor is usually higher than that of an electrolyte and the energy band of the semiconductor is formed as abovementioned semiconductor/metal junction. The removal of electrons from the semiconductor leaves behind a region of positive space charge near the semiconductor surface, consisting of ionized donors. The electric field and potential distribution in this space charge region can be obtained by integrating Poisson's equation in one dimension.

$$\frac{\partial^2 \varphi}{\partial x^2} = -\frac{\rho(x)}{\varepsilon \varepsilon_0} = -\frac{N_d}{\varepsilon \varepsilon_0} \quad (2.11)$$

Integration with the boundary conditions that the electric field and the electrical potential are zero at $x = W_{SC}$, where W_{SC} represents the width of space charge region, shows that the electric field varies linearly across the space charge region and the electrical potential varies with the square of distance. The parabolic dependence of $-\varphi$ which is apparent in Figure 2.3 corresponds to band bending in the space charge region. Although the electrical potential varies with distance, the electrochemical potential of

Chapter 2: Theoretical background

electrons is constant across the junction at equilibrium, as indicated by the horizontal line representing the Fermi energy. This means that in the dark at equilibrium, there is no driving force for the separation of thermally generated electrons and holes [2.5].

The difference of semiconductor/metal junction and semiconductor/electrolyte junction is that the electrolyte is not an electronic conductor; there are no holes and electrons to consider. Instead, electrons are localized on energy levels in the solvent and ions. It might appear that the definition of equilibrium in terms of Fermi energies would be difficult or impossible in this case, however, if the electrolyte contains a redox couple, electronic equilibrium can be achieved by electron transfer across the semiconductor/electrolyte junction. The reaction for a redox couple of oxidized phase O and reduced phase R for a one-electron reaction can be written as below.



The equilibrium condition can be expressed in terms of the electrochemical potentials of the reactants and products.

$$\bar{\mu}_O + \bar{\mu}_n = \bar{\mu}_R \quad \text{or} \quad \bar{\mu}_n = \bar{\mu}_R - \bar{\mu}_O \quad (2.13)$$

The electrochemical potential of electrons is equal to the difference between the electrochemical potentials of R and O at the equilibrium. By using equation (2.8), the electrochemical potential can be split into the chemical and electrical components.

$$\bar{\mu}_n = \mu_n - q\varphi_{SC} = \bar{\mu}_O - \bar{\mu}_R = \mu_O - \mu_R + q(z_R - z_O)\varphi_{sol} \quad (2.14)$$

Chapter 2: Theoretical background

$(z_R - z_O)$ is equivalent to the number of electrons transferred, and the difference in inner potentials (the contact potential difference) between the semiconductor and the electrolyte as below.

$$\Delta\varphi = \varphi_{SC} - \varphi_{sol} = \frac{1}{q}(\mu_n + \mu_R - \mu_O) \quad (2.15)$$

Comparison with the semiconductor/metal junction in Figure 2.3A shows that the band bending in the semiconductor is now determined by the chemical potential of electrons in the semiconductor, i. e., work function, and the difference between the chemical potentials of the redox species R and O. The redox Fermi level can also be defined in terms of the standard chemical potentials of O and R and their number densities.

$$E_{F,redox} = \bar{\mu}_R - \bar{\mu}_O = (\bar{\mu}_R^0 - \bar{\mu}_O^0) + k_B T \ln \frac{N_R}{N_O} \quad (2.15)$$

The redox Fermi level therefore plays the same role as the Fermi level of any other contact such as a metal, allowing construction of band diagrams like the Figure 2.3B.

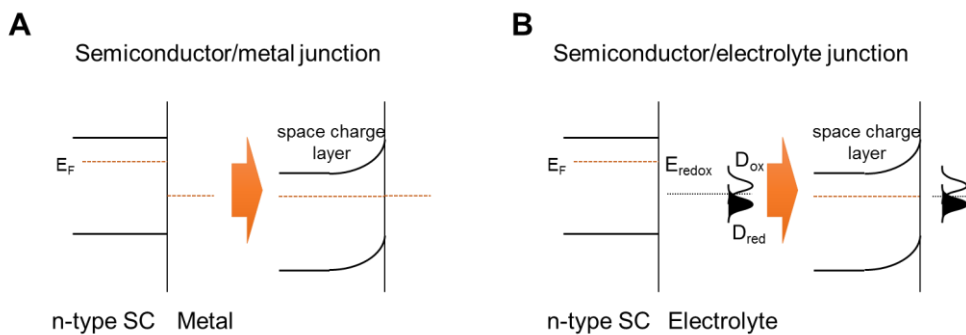


Figure 2.3 Band diagrams for n-type semiconductor/metal and n-type semiconductor/electrolyte.

2.1.3. Potential distributions at the interface

The preceding discussion shows that the redox Fermi energy in the electrolyte plays the same role as the electron Fermi level in a metal contact. It follows that if a junction is formed between an n-type semiconductor and an electrolyte that has a lower Fermi energy, a depletion layer will be formed equivalent to the semiconductor/metal contact. Similarly, a depletion layer will be formed in a p-type semiconductor if the redox Fermi energy is higher than the Fermi energy of the semiconductor. Figure 2.4 illustrates the distributions of charge, electrical field, and electrical potential across the semiconductor/electrolyte junction. Integration of Poisson's equation (Equation 2.11) using the abrupt depletion approximation gives the potential gradient at the surface of the semiconductor (Equation 2.16). A second integration gives the potential drop across the space charge region (Equation 2.17), which allows defining the width of space charge region W_{SC} as a function of potential drop $\Delta\phi_{SC}$ and the doping density N (equation 2.18), giving equation 2.19 for the electric field.

$$\left(\frac{d\phi}{dx}\right)_{x=0} = \frac{qNW_{SC}}{\epsilon_{SC}\epsilon_0} \quad (2.16)$$

$$\Delta\phi_{SC} = \frac{qNW_{SC}^2}{2\epsilon_{SC}\epsilon_0} \quad (2.17)$$

$$W_{SC} = \left(\frac{2\Delta\phi_{SC}\epsilon_{SC}\epsilon_0}{qN}\right)^{1/2} \quad (2.18)$$

$$\left(\frac{d\phi}{dx}\right)_{x=0} = \left(\frac{2qN\Delta\phi_{SC}}{\epsilon_{SC}\epsilon_0}\right)^{1/2} \quad (2.19)$$

If a redox electrolyte with a redox Fermi level that is equal to the Fermi level of semiconductor is used, no charge is removed from the semiconductor and there is no space charge region. This is the flat band condition. This situation can be obtained in the absence of a redox couple in the electrolyte by controlling the electrode potential. The potential at which the space charge region vanishes is the flat band potential, U_{fb} .

The fixed space charge in the semiconductor is balanced by a net charge of opposite sign in the electrolyte that is due to a rearrangement of the mobile ions which form an electrical double layer. In concentrated electrolytes, the ionic counter charge is located very close to the surface of the semiconductor, and we can use the simple Helmholtz model of the double layer, where the ionic charge is assumed to be situated on the outer Helmholtz plane (Figure 2.5). The Helmholtz layer gives rise to the Helmholtz capacitance, C_H , which according to the simple Helmholtz model of the electrical double layer is given as below [2.6].

$$C_H = \frac{\varepsilon_H \varepsilon_0}{\delta_H} \quad (2.20)$$

Where δ_H is the width of the Helmholtz layer, and ε_H is the relative permittivity of the electrolyte, which may be lower than the bulk value due to dielectric saturation at high fields. The potential drop across the Helmholtz layer can be obtained using dielectric continuity ($\varepsilon_{SC} E_{SC} = \varepsilon_H E_H$) as the boundary condition.

$$\Delta V_H = \frac{\varepsilon_{SC}}{\varepsilon_H} \left(\frac{2qN\Delta\phi_{SC}}{\varepsilon\varepsilon_0} \right) \delta_H \quad (2.21)$$

Chapter 2: Theoretical background

Since the charge stored in the depletion layer is proportional to the W_{SC} , the space charge capacitance per unit area can be obtained as below.

$$C_{SC} = \frac{dQ_{SC}}{d\Delta\phi_{SC}} \quad (2.22)$$

The exact solution gives the Mott-Schottky equation, written here for an n-type semiconductor considering that $\Delta\phi_{SC} = V + V_{fb}$.

$$C_{SC}^{-2} = \frac{2}{q\epsilon N_D} \left(V + V_{fb} - \frac{k_B T}{q} \right) \quad (2.23)$$

The capacitance is normally measured as a function of the applied potential in an inert electrolyte with a controlled pH rather than in a redox electrolyte. If the doping density is sufficiently low so that the potential drop across the Helmholtz layer can be neglected, $\Delta\phi_{SC}$ in equation 2.23 can be replaced by the difference $U - U_{fb}$, where U is the applied potential. It follows that the doping density and flat band potential can be obtained by plotting C_{SC}^{-2} versus electrode potential. Normally, C_{SC} is much smaller than C_H , so that the measured capacitance is close to C_{SC} . However, if the doping density is high, it is necessary to take into account the fact that the space charge capacitance is connected in series with the Helmholtz capacitance [2.7]. This does not affect the slopes of Mott Schottky plots, but displaces the intercepts. Figure 2.6 shows Mott-Schottky plots for p-type and n-type semiconductor electrodes. It represents how the flat band potential is related to the Fermi energies and the valence band and conduction band energies.

Chapter 2: Theoretical background

For an n-type semiconductor which is in equilibrium with a redox electrolyte having a lower Fermi energy, the bands are bent as shown in Figure 2.7A. If a positive potential is applied (reverse bias), the Fermi level in the semiconductor moves downward relative to the electrolyte redox level and electron flow from the redox electrolyte to the semiconductor becomes thermodynamically possible (Figure 2.7B). However, the rate of electron injection from the redox species R into the conduction band of the semiconductor is determined by the energy difference between $E_{F,redox}$ and E_C . This energy barrier is the same as the Schottky barrier that is formed with high work function metals, and it restricts current flow to a small constant value known as the reverse saturation current. If a negative potential is applied (forward bias – Figure 2.7C), the band bending decreases and electron flow from the semiconductor to the species O in the electrolyte becomes thermodynamically possible. The current will increase as the potential is made more negative and the concentration of electrons at the surface rises. Beyond the flat band potential, electrons accumulate near the surface of the semiconductor, which now behaves more like a metal electrode (Figure 2.7D).

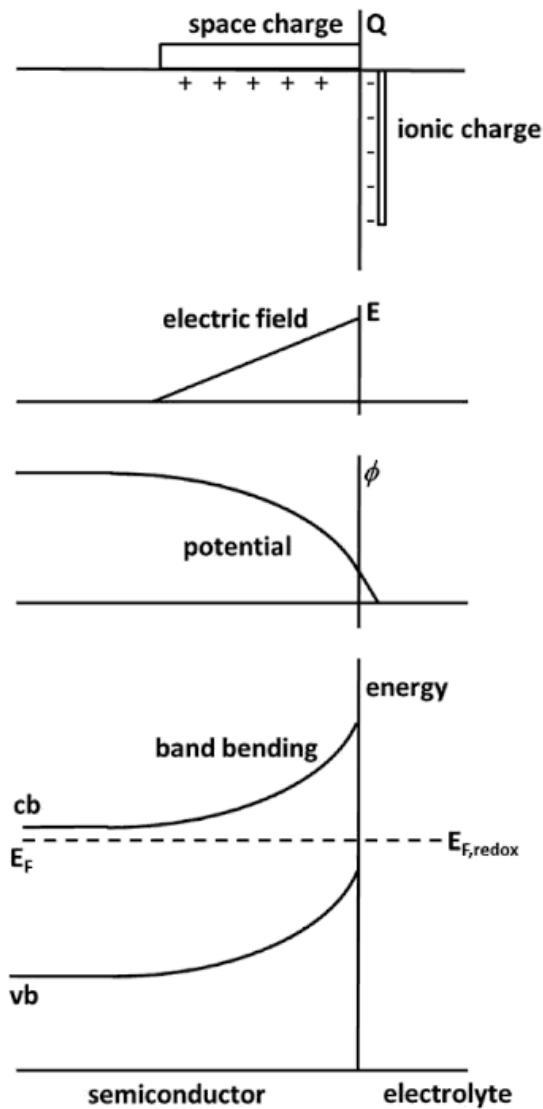


Figure 2.4 Distribution of charge, electrical field, electrical potential, and band energies showing the depletion condition that is developed when an n-type semiconductor is brought into contact with a redox electrolyte with a lower Fermi level [2.1].

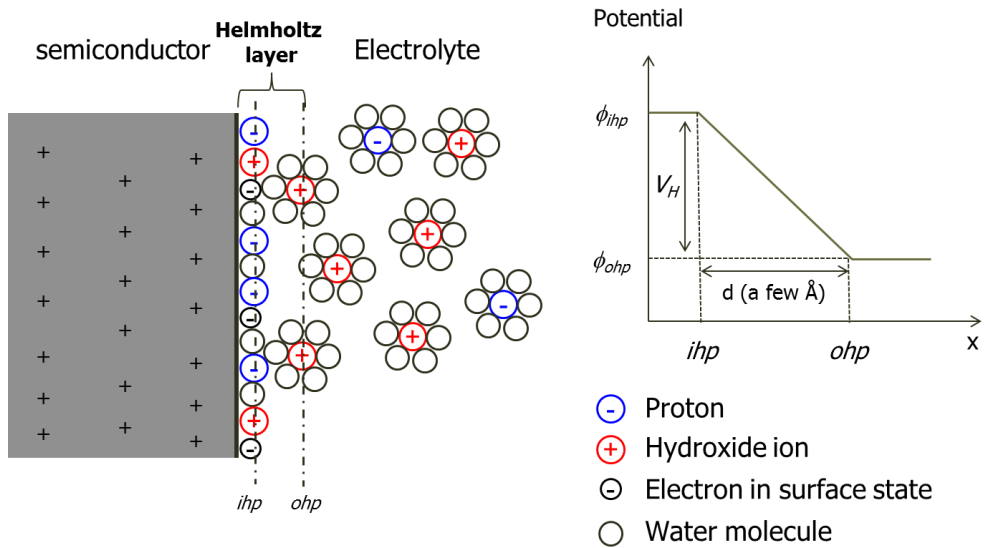


Figure 2.5 Formation of the electron double layer at the interface between the semiconductor and electrolyte. The Helmholtz layer and the potential distribution is demonstrated.

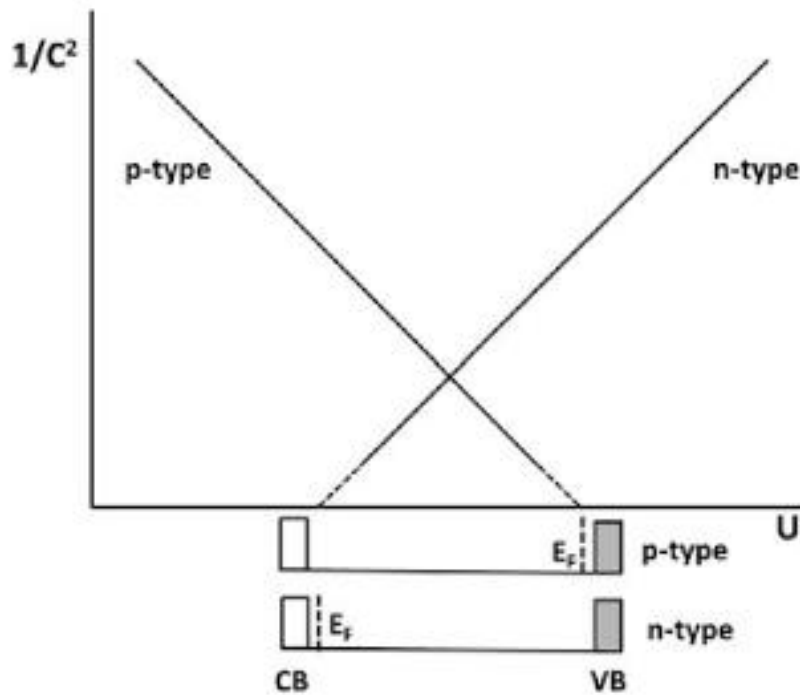


Figure 2.6 Schematic Mott-Schottky plots for the same material doped p-type and n-type. It shows how the flat band potentials are related to the Fermi energies and the band energies [2.1].

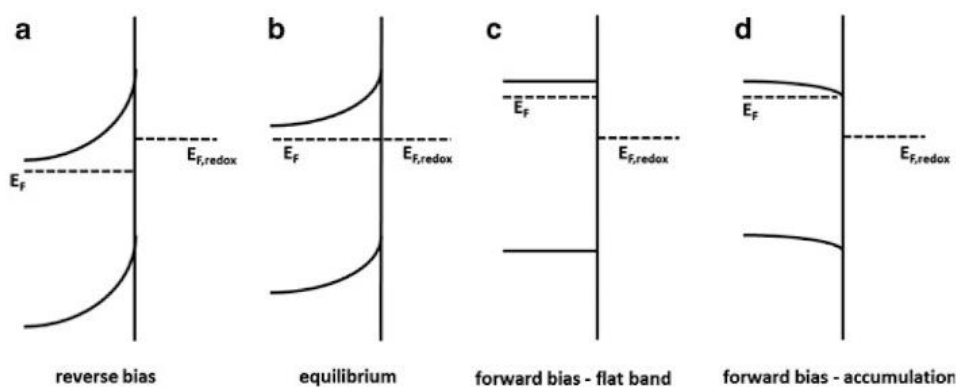


Figure 2.7 Diode behavior of the n-type semiconductor/redox electrolyte junction in the dark. The junction blocks electron flow from right to left under reverse bias, but passes an electron current from left to right as forward bias reduces band bending [2.1].

2.1.4. Photoelectrochemical process

So far we have only considered the behavior of the semiconductor/electrolyte junction in the dark. When photons with energy $h\nu = E_{gap}$ are absorbed by a semiconductor, electrons are excited across the forbidden gap, creating electron hole pairs. For a junction initially held at the equilibrium potential as shown in Figure 2.7, the local concentrations of electrons and holes will be perturbed from their equilibrium values giving rise to a splitting of the dark Fermi level into quasi-Fermi levels for electrons and holes (Figure 2.8). Since the holes generated by illumination can accept electrons from the species R, electron flow from right to left now becomes possible and a photocurrent is produced that depends on the generation, collection, and reaction of holes in the junction region. This generation and collection problem was originally solved by Gartner [2.8] for solid state junctions and adopted by Butler [2.9] for the semiconductor/electrolyte junction. The formulation of the problem are illustrated in Figure 2.9.

We begin by assuming that the reaction of holes at the surface is fast because it involves electron transfer from a fast outer sphere of redox species, i.e. no bond breaking or formation is involved. Secondly, we assume that recombination at the surface or in the space charge region can be neglected. These assumptions are equivalent to stating that all electron hole pairs generated in the space charge region are separated by the gradients of the corresponding quasi-Fermi levels. The driving force for the transport of electrons and holes is the gradient of the appropriate quasi-Fermi level. The current density is therefore given by [2.4]:

$$j = nu_n \left(\frac{\partial E_{F,n}}{\partial x} \right) + pu_p \left(\frac{\partial E_{F,p}}{\partial x} \right) = nu_n \left(\frac{\partial \bar{\mu}_n}{\partial x} \right) - pu_p \left(\frac{\partial \bar{\mu}_p}{\partial x} \right) \quad (2.24)$$

Where n and p are the concentrations and u_n and u_p are the motilities of electrons and holes. We can define currents associated with the gradient of chemical potential (diffusion current) and with the gradient of electrical potential (drift current) since the electrochemical potential can be separated conceptually into chemical and electrical parts.

We have assumed that all holes generated in the space charge region reach the surface, where they accept electrons from the redox species R, we should also consider holes generated beyond the edge of the space charge region. These have a finite diffusion length, and if they reach W_{SC} , we assume that they will be transported to the surface to accept electrons from R. the solution of this problem is the Gartner equation, which defines the ratio of the electron flux measured in the external circuit to the incident photon flux. This ratio is referred to as the external quantum efficiency (EQE) or the incident photon to current conversion efficiency (IPCE).

$$EQE = \frac{j_{photo}}{qI_0} = 1 - \frac{\exp(-\alpha W_{SC})}{1 + \alpha L_{min}} \quad (2.25)$$

Here, I_0 is the incident photon flux corrected for reflection losses, α is the absorption coefficient at the photon energy concerned, and L_{min} is the diffusion length of minority carriers.

The assumptions made in the derivation of the Gartner equation are often not valid for real systems. Firstly, surface recombination is difficult to eliminate, and secondly,

recombination in the space charge region may be important, particularly if the interfacial electron transfer is so slow that the concentration of minority carriers builds up at the interface. The reactions involved in photoelectrolysis are slow multistep processes involving adsorbed intermediates, and the equation (2.24) no longer describes the current voltage behavior because recombination is dominant, especially for low band bending. This means that the EQE is much lower than predicted by the Gartner equation.

The net current across the illuminated semiconductor/electrolyte interface is made up of the current due to the reactions involving photogenerated minority carriers as well as majority carriers, which becomes more important as the band bending is reduced under forward bias. The current voltage characteristics of an n-type semiconductor/electrolyte junction are illustrated in Figure 2.10. In this case, the penetration depth of light is similar to the width of the space charge region and $\alpha L_p < 1$, so that the photocurrent increases with increased band bending. The forward bias current increases exponentially in the same way as it would for a metal electrode, and the net current drops to zero close to the flatband potential in the ideal case. If the electrode is illuminated at open circuit, its potential will change from the equilibrium value determined by the redox couple to a new value where the net current is zero. This change is the photovoltage, V_{photo} , and for an ideal junction, it is close to the difference between the redox potential and the flat band potential.

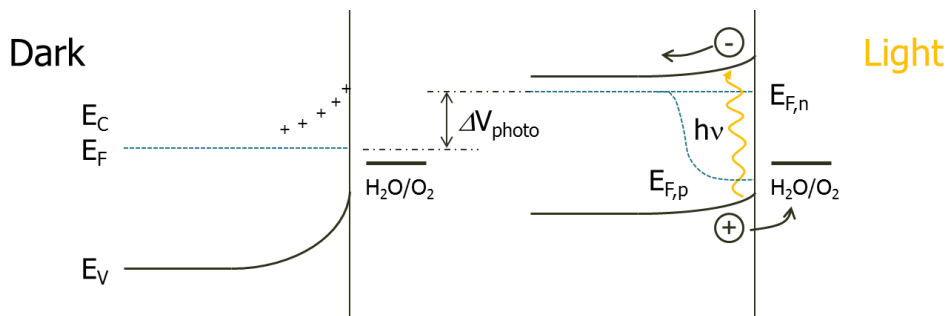


Figure 2.8 Splitting of the Fermi energies brought about by illumination in n-type semiconductor. The Fermi energy of the minority carriers (holes) is strongly affected by illumination, whereas the Fermi energy of majority carriers remains the same.

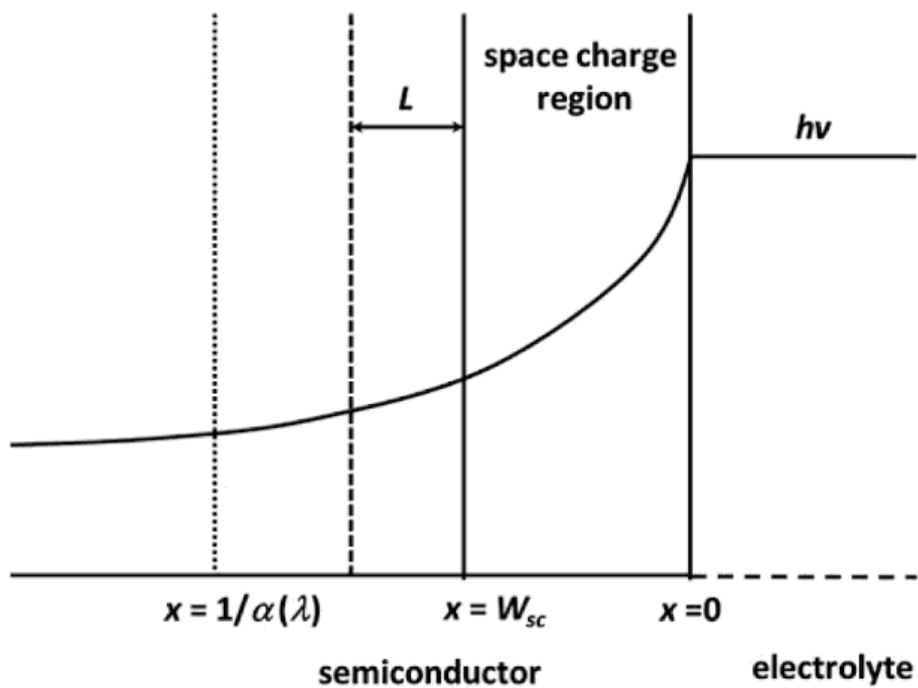


Figure 2.9 Characteristic length scales considered in the derivation of the Gartner equation. W_{sc} is the width of the space charge region and $1/\alpha$ is the wavelength dependent penetration depth of the incident light [2.1].

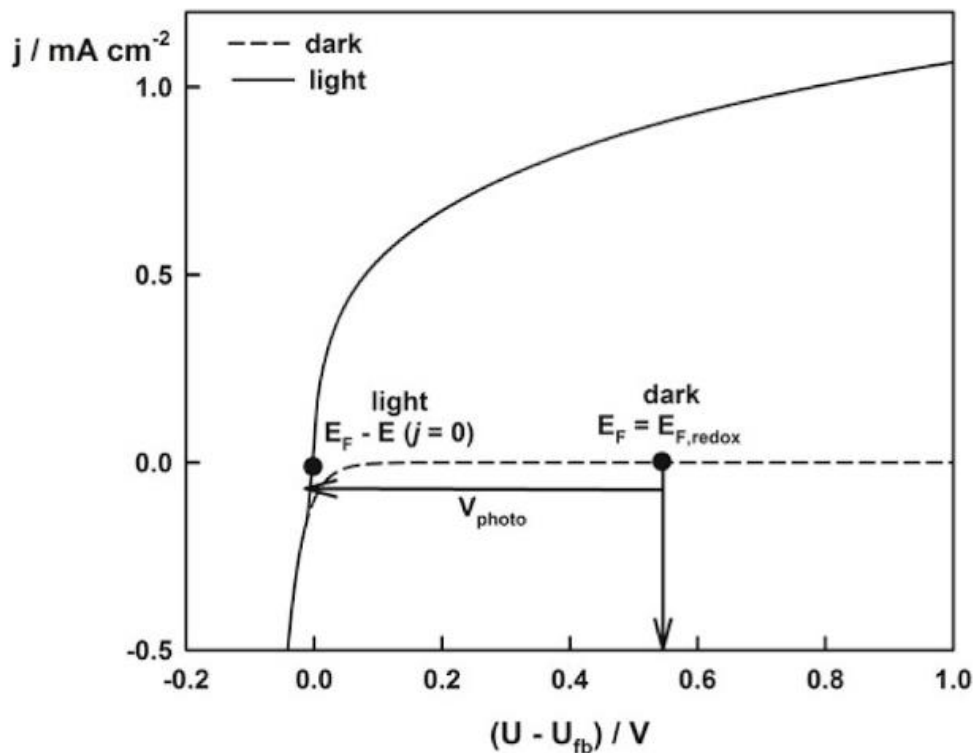


Figure 2.10 Current-voltage curves for an n-type semiconductor in the dark and under illumination. The photocurrent for the illuminated electrode was calculated using the Gartner equation. The dark current increases exponentially with forward bias. At open circuit in the dark, the electrode potential is determined by the equilibrium potential of the redox system. Under illumination, the open circuit potential is determined by the condition $j = 0$. The change in potential brought about by illumination corresponds to the photovoltage [2.1].

2.1.5. Recombination of carriers

If electron hole recombination occurs in the space charge region or at the surface, holes are lost before they can accept electrons from solution species. In this case, the steady state photocurrent voltage plots will deviate from the ideal form predicted by the Gartner equation [2.10]. A typical example showing the delayed onset of the photocurrent is demonstrated in Figure 2.11.

Surface recombination was also considered by Peter *et al.*, in a series of papers [2.11-14], and the most important aspect of surface recombination was the transient effects seen when chopped light is used to record voltammograms. When the light is switched on, photogenerated minority carriers move towards the interface, giving rise to an almost instantaneous displacement current corresponding to a change in the charge stored in the space charge capacitance (Figure 2.12). If interfacial electron transfer is slow, the concentration of minority carriers will build up near the interface. The minority carriers may be free or they may be trapped, for example, in surface states. Since the surface recombination current is proportional to the surface hole concentration, j_{rec} increases from zero when the light is switched on to a steady state value for longer times. The simplest kinetic scheme to describe these processes is shown in Figure 2.12. We assume that the current j_G due to holes moving to the surface is given by the Gartner equation. The current associated with surface recombination is due to electrons moving in the same direction as the holes, so the current has opposite sign. In addition, we also assume that the kinetics of interfacial charge transfer and of surface recombination can be described in terms of surface rather than volume concentrations. Thus, the currents due to hole transfer and recombination in Figure 2.12 are as below.

$$j_{tr} = qk_{tr}p_{surf} \quad j_{rec} = qk_{rec}p_{surf} = q\sigma v_{th}n_{x=0}p_{surf} \quad (2.26)$$

Here k_{tr} and k_{rec} are first-order rate constants (s^{-1}), p_{surf} is the surface concentration (cm^{-2}) of holes, σ is the capture cross-section for electron hole recombination, and v_{th} is the thermal velocity. It can be seen from Figure 2.12 that time-dependent hole concentration is determined by the difference between the rate of arrival of holes at the surface (j_G) and the rate of their removal by recombination (j_{rec}) and transfer (j_{tr}).

$$q \frac{dp_{surf}}{dt} = j_G(t) - qk_{tr}p_{surf}(t) - qk_{rec}p_{surf}(t) \quad (2.26)$$

When the light is switched on, the initial concentration of holes is zero, so $j_{rec} = 0$ and we measure the charging current j_G . As p_{surf} increases with time, j_{rec} increases proportionately and the measured photocurrent falls if interfacial hole transfer is sufficiently slow that recombination can begin to compete for holes. Finally in the steady state, the hole concentration becomes constant and the measured photocurrent decays to a plateau. The time-dependent hole concentration is obtained by solving equation 2.26 for the case of a square light pulse of duration τ .

$$p_{surf}(t < \tau) = \frac{j_G}{q(k_{tr} + k_{rec})} (1 - \exp[-(k_{tr} + k_{rec})t]) \quad (2.27a)$$

$$p_{surf}(t < \tau) = p_{surf}(\tau) \exp[-(k_{tr} + k_{rec})t] \quad (2.27b)$$

Chapter 2: Theoretical background

The exponential decay of the photocurrent seen after switching the light on is given by below.

$$\frac{j_{photo}(t) - j_{photo}(\infty)}{j_{photo}(0) - j_{photo}(\infty)} = \exp[(k_{tr} + k_{rec})t] \quad (2.28)$$

The steady state current is given as below.

$$\frac{j_{photo}(\infty)}{j_{photo}(0)} = \frac{k_{tr}}{k_{tr} + k_{rec}} \quad (2.29)$$

When the light is switched off after some time τ , j_G falls almost instantaneously to zero, and the recombination of the residual holes at the surface gives rise to a transient current of opposite sign to the photocurrent as electrons move to the surface to recombine with the holes. This overshoot current also decays exponentially, in this case to zero.

$$\frac{j(t > \tau)}{j(0) - j(\tau)} = \exp[-(k_{tr} + k_{rec})t] \quad (2.30)$$

The time dependence of the surface hole concentration and photocurrents is shown in normalized form in Figure 2.13. Since $k_{tr} = k_{rec}$ in this example, only half of the holes arriving at the surface are transferred to the electrolyte under steady state conditions. The values of k_{tr} and k_{rec} can be obtained from the decay lifetime and the ratio of steady state to instantaneous current.

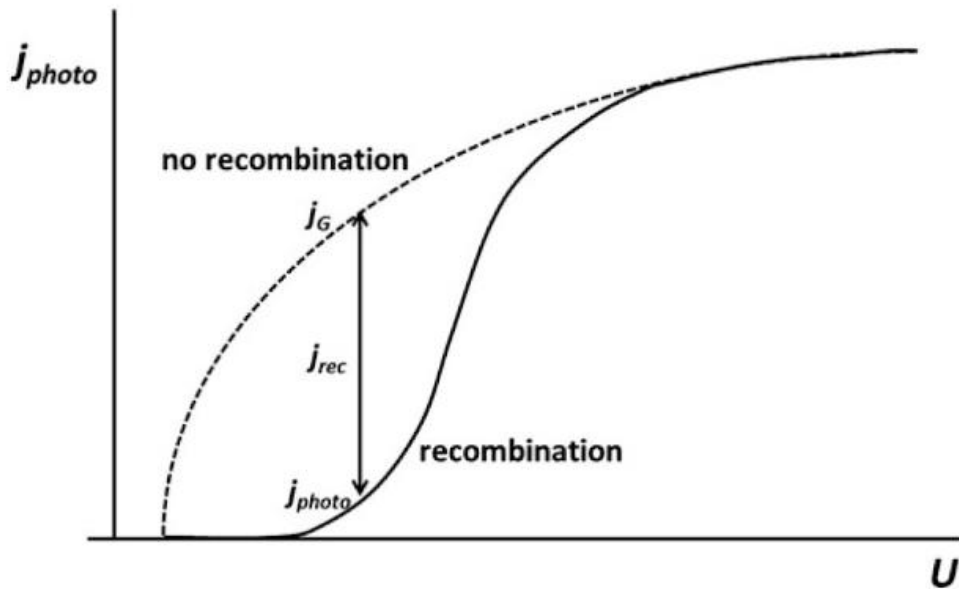


Figure 2.11 Delayed onset of photocurrent arising from recombination, either in the space charge region or at the surface. j_G is the current predicted by the Gartner equation, j_{photo} is the experimental photocurrent, and j_{rec} is the recombination current [2.1].

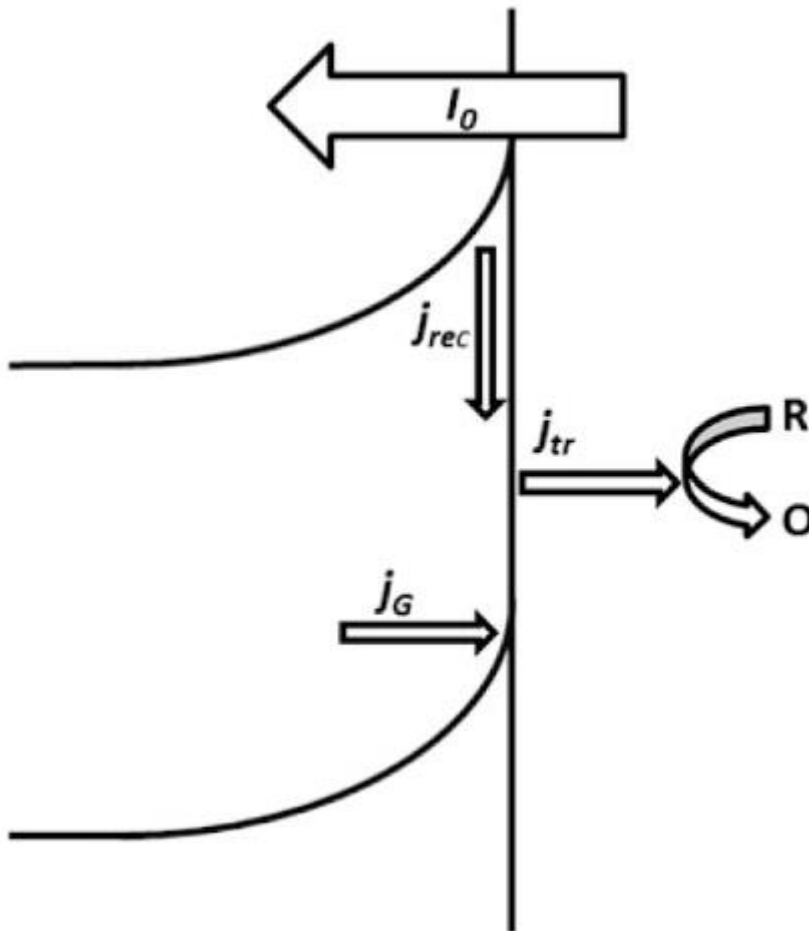


Figure 2.12 Scheme of kinetic that describes the competition between charge transfer and surface recombination [2.1].

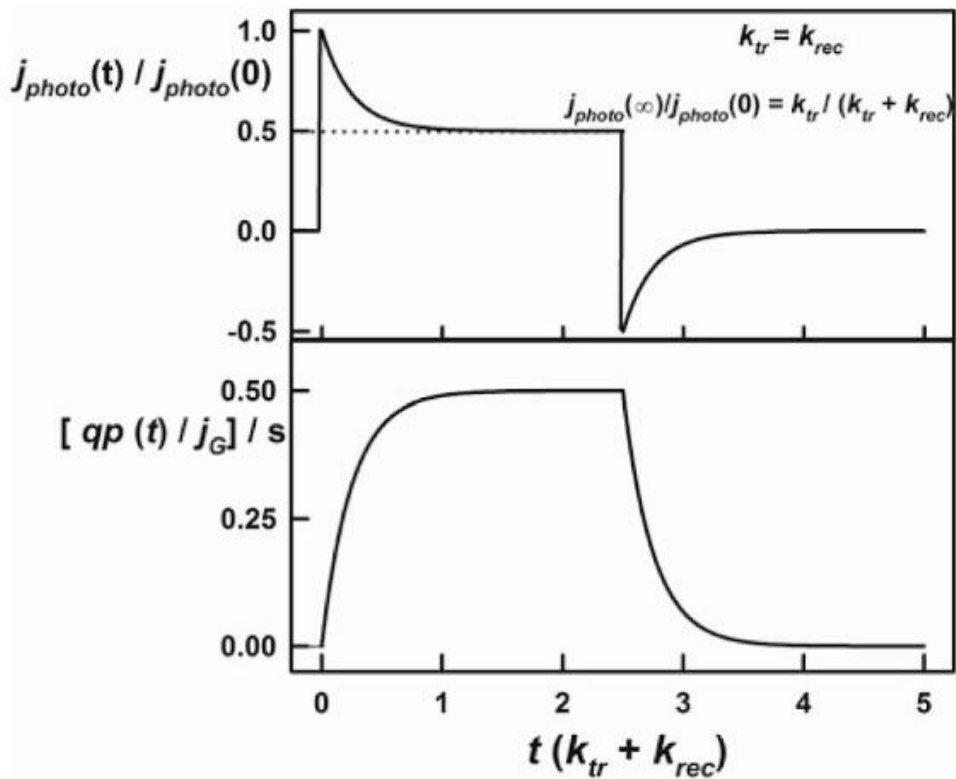


Figure 2.13 Normalized plots of transient photocurrent and corresponding surface hole concentration for $k_{tr} = k_{rec}$. The exponential decay time constant $(k_{tr} + k_{rec})^{-1}$ and the ratio of the steady state current to the spike = $k_{tr} / (k_{tr} + k_{rec})$, allowing k_{tr} and k_{rec} to be determined [2.1].

2.2. Photoelectrochemical CO₂ reduction

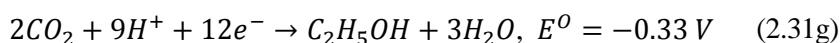
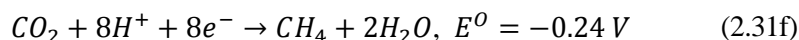
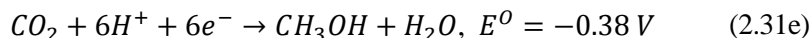
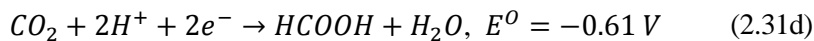
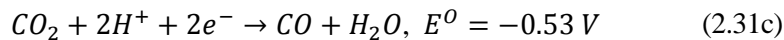
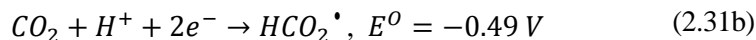
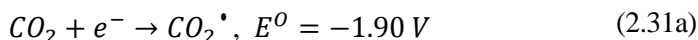
A perennial quest for managing CO₂ effectively to other hydrocarbon has become inevitable due to the fast-growing CO₂ discharge leading to the global warming. The photoelectrochemical reduction of CO₂ has gathered significant attention since it mimics the natural photosynthesis process by mimicking the Z-scheme.

The conversion of CO₂ to other hydrocarbons can be described in three steps: generation of charge carriers through excitation, charge separation and transportation, and reduction of CO₂ by photogenerated electrons.

In this section, the mechanism for CO₂ reduction into various other carbon compounds and the material candidates for the photocathode with their reported properties are reviewed.

2.2.1. Theory of photoelectrochemical CO₂ reduction

In order to fabricate a photocathode material that can effectively convert CO₂ into other carbon compounds, thorough understanding of energy band is required. The positions of the conduction band should match the reduction potentials of CO₂ reduction, and Figure 2.14 shows the band edge position of a few selected semiconductor materials relative to the energy of various redox couples at pH 1 in aqueous solution. Since CO₂ is chemically stable due to the covalently bonded carbon and oxygen with the double bond having enthalpy of +805 kJ mol⁻¹, a substantial amount of energy is required for the bond breaking process. Thus, a photocathode with sufficient reduction potential for CO₂ will enable the formation of a spectrum of products depending on the photoelectrochemical reduction potential as given in the following equations [2.15-18].



Three plausible mechanisms have been widely accepted for the conversion of 1 mole of CO₂ to methane over a photocatalyst: the formaldehyde route, the carbene route, and glyoxal route. The three mechanisms are depicted in Figure 2.15 [2.19, 20].

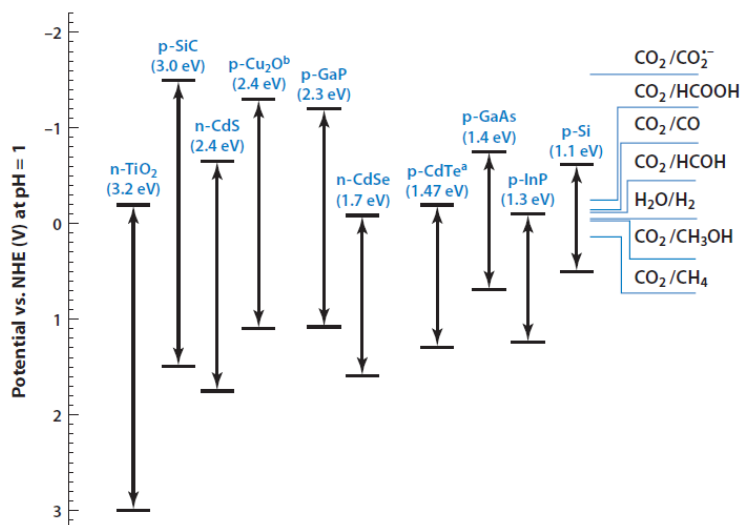


Figure 2.14 Band edge positions of various semiconductors relative to the redox potentials at pH 1 of compounds involved in CO₂ reduction [2.21].

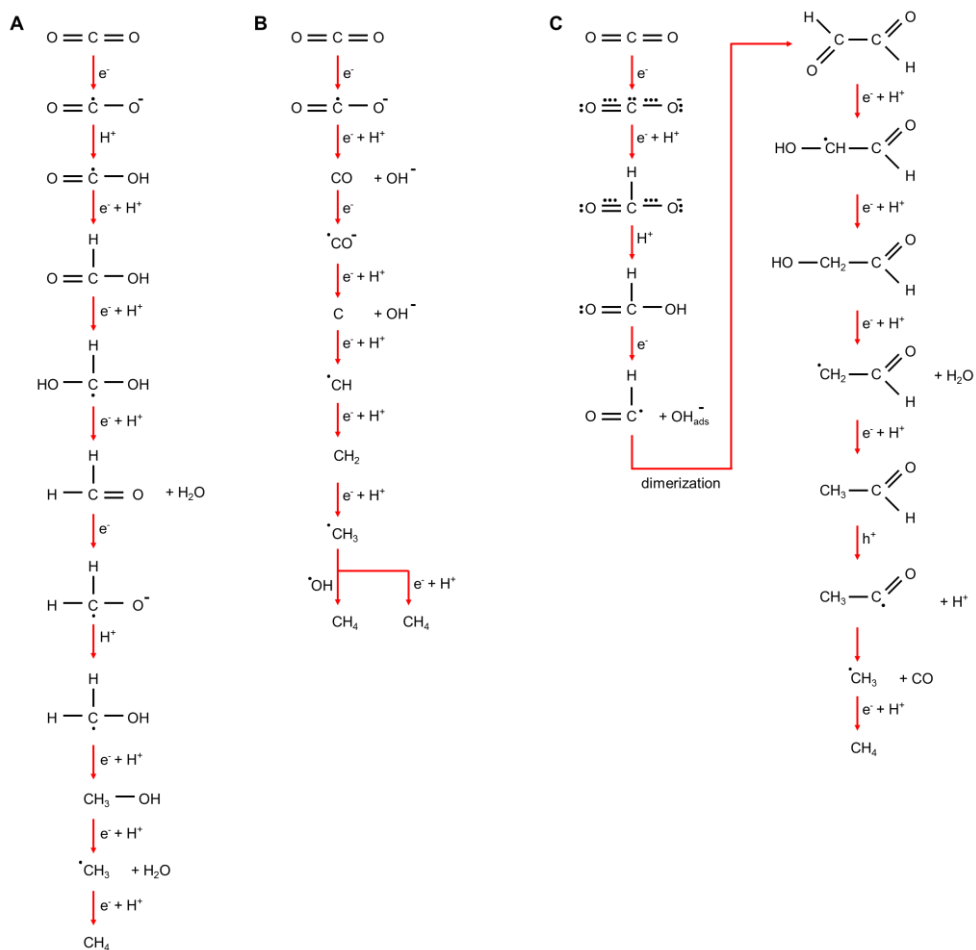


Figure 2.15 CO₂ reduction mechanism following (A) formaldehyde route, (B) carbene route, and (C) glyoxal route [2.19, 20].

2.2.2. Summary of CO₂ reduction catalyst and performances

To predict the photoactivity of photocathode material candidates for the photoelectrochemical CO₂ reduction, it is useful to compare their photocatalytic performances, which have been widely studied in the past. Table 2.1 shows photocatalytic performances of CO₂ reduction for various semiconducting materials.

Table 2.1 Summary of CO₂ reduction photocatalyst materials and corresponding performances.

Photocatalyst	Co-catalyst	Output products	Yield (μmol/g·h) (*ppm/g·h)(**mmol/h)	Ref.
Mesoporous TiO ₂ NFs	-	CH ₄	3.08 – 19.55	2.22
TiO ₂ /Pt-MgO	Pt-MgO	CH ₄ , CO	0.7 (CH ₄); 0.28 (CO)	2.23
Cu ₂ O@Pt/TiO ₂	Pt, Cu	H ₂ , CO, CH ₄	25 (H ₂); 8.3 (CO); 33 (CH ₄)	2.24
Cu ₂ O/TiO ₂	Cu ₂ O	CH ₄	25*	2.25
CeO ₂ /TiO ₂	CeO ₂	CH ₄ , CO	12000-13100 (CO); 442 (CH ₄)	2.26
Cu/TiO ₂ -P25	Cu	CH ₄ , CO	12-24 (CO); 0.46-0.65 (CH ₄)	2.27
Ag@TiO ₂	Ag	CH ₄ , CH ₃ OH	0.44 (CH ₄ +CH ₃ OH)	2.28

Chapter 2: Theoretical background

Cu, Pt@TiO ₂	Cu, Pt	CH ₄ , C _x H _y	2.6 ml/g·h (CH ₄); 3.5 ml/g·h (C _x H _y)	2.29
Au/Pt@TiO ₂	Au/Pt	CH ₄ , CO	114 (CH ₄); 17(CO)	2.30
Graphene/TiO ₂	Graphene	CH ₄ , C ₂ H ₆	4.6-10.1 (CH ₄); 7.2-16.8 (C ₂ H ₆)	2.31
MWCNT/TiO ₂	MWCNT	CH ₄	0.17 (CH ₄)	2.32
Zn ₂ GeO ₄	-	CH ₄ , O ₂	3.8 (CH ₄); 22 (O ₂)	2.33
Zn ₂ GeO ₄ (100)	-	CH ₄ , O ₂	1.2 (CH ₄); 12 (O ₂)	2.33
Zn@Ga ₂ O ₃ /Ag	-	CO, H ₂ , O ₂	117 (CO); 16.9 (H ₂); 70.1 (O ₂)	2.34
Cd ₂ Ge ₂ O ₆ /RuO ₂	RuO ₂	CH ₄	0.72 (CH ₄)	2.35
NaNbO ₃	-	CH ₄	0.45-5.7 (CH ₄)	2.36
In ₂ O ₃ /g-C ₃ N ₄	Pt	H ₂	1990*	2.37
Layered double hydroxides	-	CO, O ₂	0.5-3.7 (CO); 0.4-6.4 (O ₂)	2.38
AgX:Ag (X=Cl, Br)	-	CH ₃ OH	8 (X=Cl; CH ₃ OH); 22 (X=Br; CH ₃ OH)	2.39
W ₁₈ O ₄₉	-	CH ₄	666*	2.40
CuGaO ₂	-	CO	9*	2.41
LiNbO ₃	-	CH ₂ O ₂	7.7**	2.42
Bi ₂ WO ₆	-	CH ₄	1.1	2.43
BiVO ₄	-	C ₂ H ₅ OH	110	2.44
Ga ₂ O ₃	-	H ₂ , CO	4.13 (H ₂); 1.8 (CO)	2.45
ZrO ₂	-	CO	0.51	2.46

Chapter 2: Theoretical background

MgO/ZrO ₂	-	CO	2.4	2.47
NiO	-	CH ₃ OH	393	2.48

2.3. Photoelectrochemical water oxidation

The oxidation of water is a counter reaction of photoelectrochemical CO₂ reduction and hydrogen evolution reaction, which occurs at the photoanode of a photoelectrochemical cell. The photoelectrochemical oxidation of water is free from the problem of reaction selectivity because other competitive reactions are too much unfavorable than the water oxidation. However, the overpotential for the oxidation of water is still large about several hundreds of millivolts, thus needs an efficient photoanode with small overpotential and large photocurrent density.

In this section, the detailed mechanism and fundamentals for the water oxidation are reviewed. In addition, the trends in activity of water oxidation according to the suggested descriptors are reviewed.

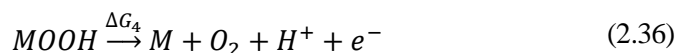
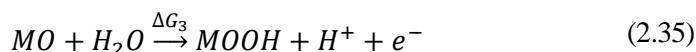
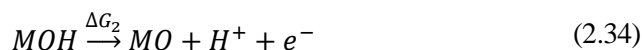
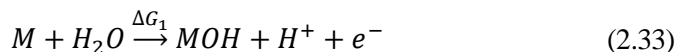
2.3.1. Theory of photoelectrochemical water oxidation

In terms of a mechanistic analysis of the water oxidation (OER), a major difficulty lies in the fact that the OER is a complex process involving the transfer of four electrons. Since electrons are transferred one at a time the process will, by necessity, be multistep in which distinct intermediates are generated on the electrode surface. Consequently, the OER may follow any of a number of different pathways.

Over the years, various possible mechanistic schemes have been proposed with notable early studies. [2.49-53] In these early mechanistic schemes the OER was usually interpreted in terms of an initial discharge of hydroxide ions at a catalytically active surface site M leading to the formation of discrete adsorbed hydroxide intermediates:



Subsequent steps in the reaction were thought to involve the formation of a range of surface adsorbed intermediates such as MO, MOOH or physisorbed peroxide species, which could then react with each other, through various disproportionation or bimolecular decomposition reactions. Based on this, the model reaction mechanism termed the associative mechanism was suggested [2.54].



Where ΔG_i is the Gibbs free reaction energy of reaction step i . Each reaction step involves the transfer of one electron implying the free energy change for each step will be potential dependent. Also, while this mechanism describes the OER under acidic conditions, the thermodynamic conclusions are independent of pH as the free energies deduced from equation (2.33) to (2.36) vary in the same way with pH [2.55]. In this theoretical framework, the Gibbs free adsorption energies of the surface intermediates ΔG_{MOH} , ΔG_{MO} , and ΔG_{MOOH} are calculated as a function of the electrode potential [2.54]. At a given applied potential, the reaction energy of each elementary mechanistic step was given by the difference between the adsorption energies of two intermediates [2.54, 55].

A free energy diagrams for two catalysts are plotted at different potentials in Figure 2.16. The horizontal lines represent the free adsorption energies of the individual intermediates and the reaction coordinate moves from free water on the left to free O₂ on the right. For a typical catalyst, the reaction energies for each step will differ due to irregular variations in the adsorption energies of the intermediate species [2.56]. All steps in the reaction are thermodynamically unfavorable at potentials below the reversible potential, $V_1 - V^0 = \eta < 0$, with $\Delta G_i > 0$. As the potential is increased, the free energies of the intermediates shift negatively so that the reaction steps eventually become thermodynamically favorable with $\Delta G_i \leq 0$. The overall thermodynamics of the OER are determined by the last elementary reaction step to become thermodynamically favorable. This step is referred to as the potential-determining step [2.57], and its magnitude is simply the largest ΔG_i values as below [2.58].

$$\Delta G^{OER} = \max[\Delta G_1, \Delta G_2, \Delta G_3, \Delta G_4] \quad (2.37)$$

In this respect, the thermodynamic overpotential is the additional potential required by the potential-determining step, which is given by [2.58]:

$$\eta^{OER} = \Delta G^{OER}/q - 1.23 \text{ V} \quad (2.38)$$

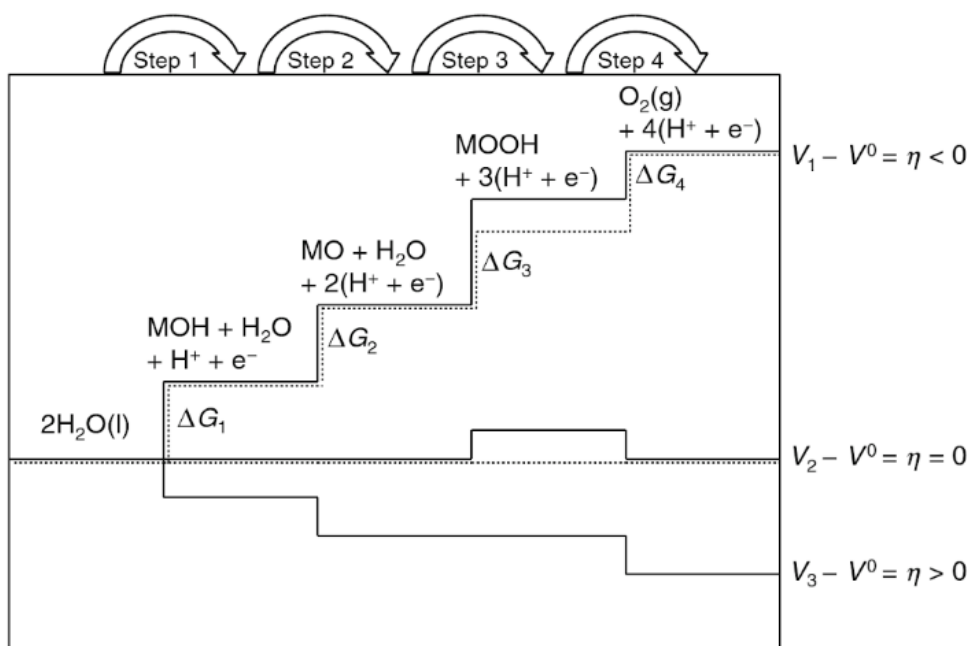


Figure 2.16 Schematic plot of the Gibbs free energy of the reactive species and intermediates in the oxygen evolution reaction versus the reaction coordinate. Solid lines indicate the energetics of a real catalyst and dotted lines indicate that of an ideal catalyst [2.56].

2.3.2. Trends in water oxidation activity of catalyst

Over the past fifty years, considerable research efforts have been devoted to the kinetic and mechanistic study of the OER. However, little mechanistic consensus has been achieved though many studies have attempted to rationalize the relative electrocatalytic activities of different electrode materials in terms of a given physicochemical property of descriptor. The volcano plot has been widely applied in the study of heterogeneous chemical catalysis [2.59] and a schematic representation is presented in Figure 2.17. A descriptor could be any of a number of properties of the catalyst [2.60], however, the most successful descriptors generally describe the interaction between a key reaction intermediate and the catalytic surface. Figure 2.17 suggests that an optimal interaction exists, which is the Sabatier principle stating that the best catalyst binds the intermediates with appropriate forces [2.59, 61]. If the interaction is too weak or too strong, the catalyst fails to activate the reactant or the product fails to dissociate.

The first volcano relation for the OER was displayed in Figure 2.18 [2.62] which showed a correlation between the overpotential and the standard enthalpy change for a lower to higher valent oxide transformation. This correlation can be rationalized if the OER is expected to involve one or more surface bound oxygen moieties such as MOH, MO, or MOOH. The interaction of these intermediates with the surface of a given oxide MO_x could result in an increase in the coordination sphere of M, and therefore their formation would be expected to parallel to the heat of formation of the oxide in the next valence state [2.62, 63].

In addition, advances in DFT calculations have enabled an explicit description of OER activity in terms of calculated adsorption energies. The intermediates for the OER at metal oxide are suggested: MOH, MO, and MOOH. Indeed, subject to whichever reaction step is potential determining, the binding energy of these species could prove a suitable descriptor.

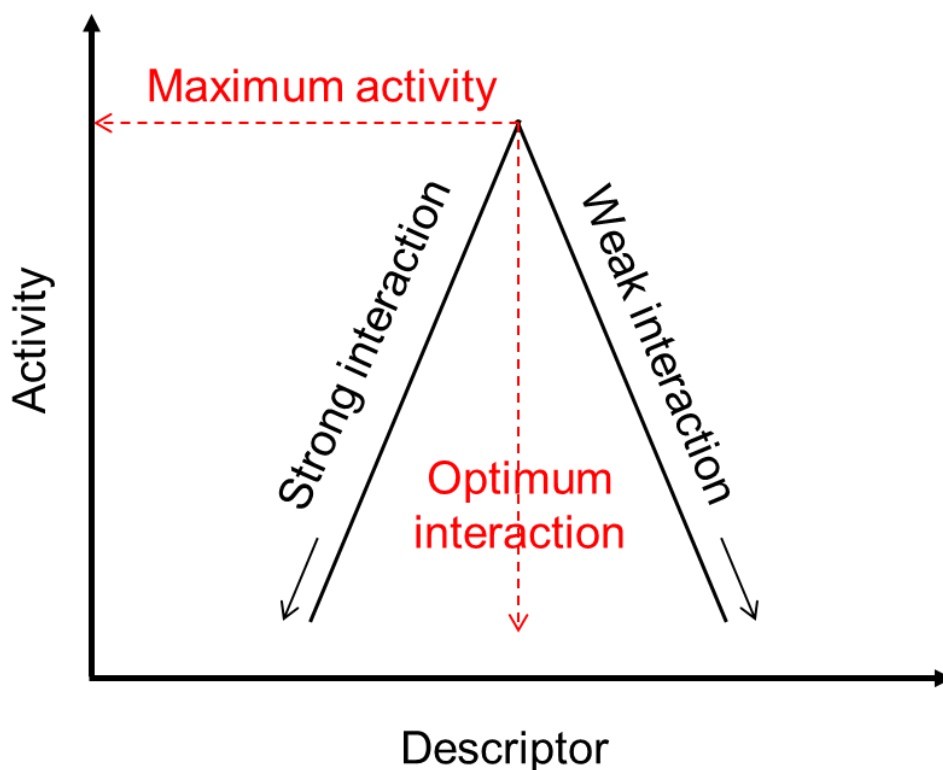


Figure 2.17 Schematic plot of the Gibbs free energy of the reactive species and intermediates in the oxygen evolution reaction versus the reaction coordinate. Solid lines indicate the energetics of a real catalyst and dotted lines indicate that of an ideal catalyst.

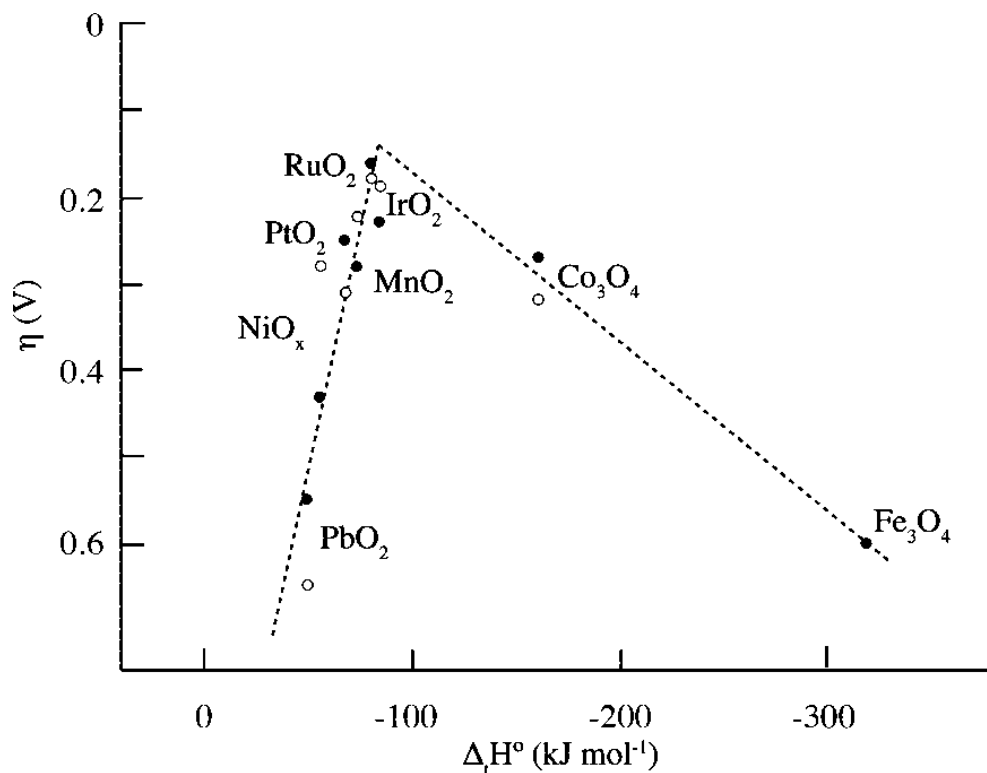


Figure 2.18 Schematic plot of the Gibbs free energy of the reactive species and intermediates in the oxygen evolution reaction versus the reaction coordinate. Solid lines indicate the energetics of a real catalyst and dotted lines indicate that of an ideal catalyst [2.62].

CHAPTER 3

Experimental procedures

3.1. Sample preparation

3.1.1. Fabrication of Cu₂O photocathode

Fluorine-doped tin oxide (FTO) on a glass substrate (15 mm × 25 mm × 2.2 mm; 7 Ω□⁻¹) were cleaned by sonification in acetone, ethyl alcohol, and deionized water, sequentially. Metallic copper thin film underlayer was sputtered with the DC power of 150 W and the working pressure of 4 mTorr.

The Cu₂O nanofibers were prepared by a simple electrospinning process. Mixture of 9 g of distilled water (DI) and 1 g of dimethylformamide (DMF, Sigma Aldrich, > 99.8%) was used as the solvent and 1.111 g of polyvinylalcohol (PVA, M_w ~ 89000, Sigma Aldrich) was added in solution followed by the addition of 0.555 g of copper acetate (Cu(CH₃COO)₂·H₂O, M_w = 199.65, Sigma Aldrich). Then the mixture was vigorously stirred at room temperature for 8 hours to form a homogeneous precursor solution, and the solution was electrospun via a syringe with a metal needle tip (18G). The distance between the needle tip and the grounded collector was 12 cm, and the

feeding rate of 0.6 ml/h during the 2 minutes of electrospinning time. Substrate with thin film of copper deposited on FTO glass was lied on grounded collector during the electrospinning process.

Ultrathin Titanium dioxide (TiO_2) passivation layer was deposited on the surface of the Cu_2O nanofiber electrodes using a plasma enhanced atomic layer deposition (PEALD, Plus 100, Quoros. co) system. The ALD was carried out at a substrate temperature of $150\text{ }^\circ\text{C}$ in order not to vary the oxidation number of Cu_2O nanofibers. Titanium dioxide was deposited using titanium tetraisopropoxide (TTIP, $\text{Ti}(\text{OCH}(\text{CH}_3)_2)_4$) and O_2 plasma as the Ti and O precursors. Ti precursor was evaporated at $40\text{ }^\circ\text{C}$ and transported by Ar gas with a flow rate of 10 sccm. O_2 and Ar gases were used as the plasma and purge gases, respectively, with a flow rate of 50 sccm. The RF power during deposition was 100 W with a working pressure of 200 mTorr. The GPC for TiO_2 was 0.6 \AA , which was measured by ellipsometry of TiO_2 films deposited on polished silicon wafers with a native surface oxide. Following ALD, the samples were annealed at $450\text{ }^\circ\text{C}$ for 1 hour with $p\text{O}_2$ of $10\text{ }\mu\text{Torr}$.

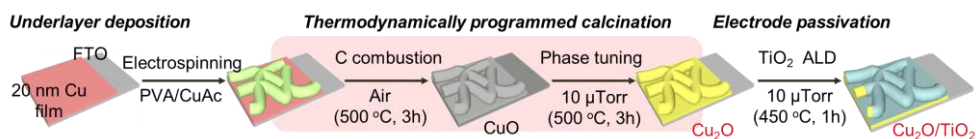


Figure 3.1 Schematic illustration of fabrication process of mono-phase Cu_2O nanofiber with hierarchical structure consists of Cu_2O thin film underlayer and TiO_2 passivation layer.

3.1.2. Fabrication of Fe₂O₃ photoanode

(This section cited reference [3.1, 2])

First, the fabrication process for the hematite photoanode samples to investigate the effect of oxygen vacancies on the photoactivity is demonstrated. substrates of fluorine-doped tin oxide (FTO) on glass (20 mm×25 mm×2.2 mm; $7 \Omega \square^{-1}$) were cleaned by sonification in a acetone, isopropyl alcohol, and deionized water, sequentially. The cleaned substrates were pretreated with diluted TEOS solution. An ethanol (99%, DaeJung)-based 10 mM of the iron(III) chloride hexahydrate (FeCl₃·6H₂O, >99%, Sigma-Aldrich) solution was directly sprayed using compressed air onto a FTO substrate on a hot plate heated at 400 °C (aerosol spray pyrolysis (ASP), Figure 3.2A). The amount of the precursor solution sprayed was 30 mL, and 1mL of the solution was sprayed per one cycle every 30 seconds. Evaporation of the ethanol and pyrolysis of FeCl₃·6H₂O in ambient air resulted in the formation of Fe₂O₃ at the surface of the FTO. The Sn-doped hematite was also prepared by ASP under the same conditions, except that tin(IV) chloride pentahydrate (SnCl₄·5H₂O, 98%, Sigma-Aldrich) was dissolved in the FeCl₃-ethanol precursor solution. The Sn concentration was controlled by changing the amount of SnCl₄·5H₂O in the 30 mL of 10 mM-FeCl₃ solution. Figure 3.2A schematically shows the spray pyrolysis process. As-prepared hematite films by ASP were annealed in a tube furnace. Firstly, the hematite films were annealed at 550 °C for 1 h (ramping rate of 5 °C min.⁻¹) under high vacuum (base pressure of 1.2×10^{-6} Torr). The hematite films were subsequently annealed in oxygen ambient for 2 h. The oxygen partial pressure (p_{O_2}) was controlled to 5×10^{-5} , 5×10^{-3} , 5×10^{-2} , 5×10^{-1} , and 150 (ambient air) Torr by varying the flow-in rate of oxygen gas using a mass flow controller (MFC) and the flow-out rate using an angle throttle valve. To lower the p_{O_2} to 5×10^{-5} mTorr,

Chapter 3: Experimental procedures

the chamber was filled with an Ar/O₂ mixture gas to a the total pressure of 5 mTorr at the flow rate of 30 sccm for Ar and 0.3 sccm for O₂. For a comparison, a hematite was annealed at 550 °C for 3 h in ambient air. These annealing procedures are described as schematic diagrams in Figure 3.2B.

Second, the fabrication process for the hematite photoanode to investigate the effect of hierarchical structures on the photoactivity is demonstrated. Fluorine-doped tin oxide (FTO) on a glass substrate (15 mm x 25 mm x 2.2 mm; 7 Ω □⁻¹) was cleaned by sequentially sonicating in acetone, ethyl alcohol, and deionized water. Hydrothermal syntheses were conducted according to the method previously reported by Vayssieres et al. Twenty milliliters of an aqueous solution with iron chloride hexahydrate (0.15 M FeCl₃·6H₂O, >99%, Sigma-Aldrich) and sodium nitrate (1 M NaNO₃, 99%, Sigma-Aldrich) was transferred to a Teflon-lined autoclave with a 100 ml capacity. An FTO glass was loaded into the autoclave. Titanium doping was performed by adding titanium (IV) butoxide (Ti(OBu)₄, 10 μl, >97%, Sigma-Aldrich) into the precursor solution with concentrated hydrochloric acid (HCl, 70 μl, 35.0 %~37.0 %, Samchun). For the synthesis of the undoped hematite underlayer, the autoclave was placed in an oven and maintained at 95 °C for 50 minutes with the undoped precursor solution. Then, to synthesize the Ti-doped hematite layer, the autoclave was maintained at 95 °C for 13 hours in an oven with an underlayer-grown FTO substrate with the Ti-dopant added to the precursor solution. At last, the as-prepared samples were annealed in ambient air at 550 °C for 3 hours in a furnace. Third, the β-FeOOH layers were synthesized by loading the previously made sample into the autoclave and maintaining at 95 °C for 20-50 minutes with the undoped precursor solution. The schematic diagram for this synthetic process is shown in Figure 3.3.

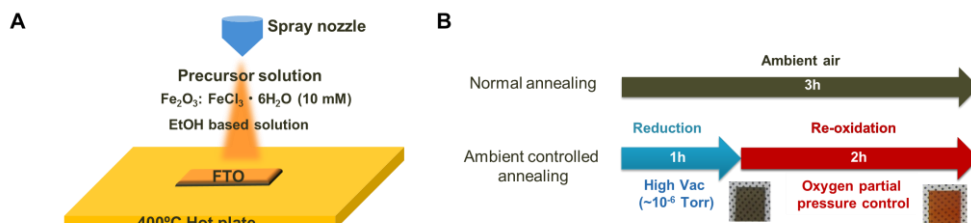


Figure 3.2 (A) Schematic for the process of spray pyrolysis that fabricates nanostructured Fe_2O_3 electrode. (B) Novel annealing process to effectively generate the oxygen vacancies in the hematite photoanode.

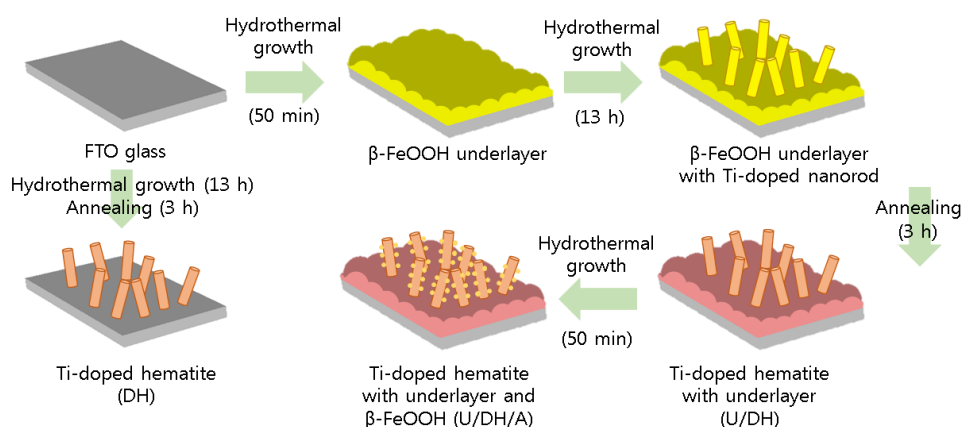


Figure 3.3 The procedure to fabricate a hierarchically structured hematite photoanode using hydrothermal synthesis.

3.2. Photoelectrochemical analysis

3.2.1. Photoelectrochemical analysis on Cu₂O photocathodes

Photoelectrochemical and electrochemical characterization were performed in 0.5 M KHCO₃ (pH 8.8) electrolyte using a three-electrode electrochemical cell configuration with a reference electrode of saturated calomel electrode (SCE) and counter electrode of Pt foil. The cuprous oxide working electrode was masked to define an active area of 0.28 cm². A Newport 300 W xenon arc lamp and AM 1.5G filter were used to simulate sunlight illumination with intensity of 100 mW cm⁻². 0.5 M KHCO₃ electrolyte was purged with CO₂ gas bubbling for 10 minutes before bulk electrolysis, and bulk electrolysis was subsequently performed for 20 minutes at potentials between 0.4 V and 0.8 V vs. RHE. During the linear sweep voltammetry, the potential was scanned between +0.8 V and +0.4 V versus RHE at a rate of 10 mV s⁻¹ with constantly chopped light. Light-chopping was performed with the Newport shutter which was set to turn the light on and off every 2 seconds. The headspace gases were collected by syringe with the volume of 1 ml, and were analyzed by gas chromatography and liquid products were analyzed by collecting 10 ml of liquid from the electrolyte after bulk electrolysis, and confirmed by nuclear magnetic resonance spectroscopy (NMR, Avance 600MHz, Bruker).

3.2.2. Photoelectrochemical analysis on Fe₂O₃ photoanodes

(This section cited reference [3.1, 2])

Photoelectrochemical and electrochemical characterizations were performed in a 1 M NaOH (pH 13.6) electrolyte using a three-electrode electrochemical cell configuration

Chapter 3: Experimental procedures

with an SCE reference electrode, and a Pt foil counter electrode. The hematite working electrode was masked to define an active area of 0.28 cm^2 . A Newport 300 W xenon arc lamp and an AM 1.5G filter were used to simulate sunlight illumination with an intensity of 100 mW cm^{-2} . During the photocurrent measurements, the potential was scanned between -0.3 V and 0.7 V versus SCE at a rate of 10 mV s^{-1} . Light-chopping J-E was performed with a Newport shutter, which was set to turn the light on and off every 2 seconds. Impedance spectroscopic measurements were performed with a multi-channel analyzer (ZIVE-MP2 Wonatech), and the data were fitted using ZMAN software. Data were collected using Potentiodynamic EIS mode with a 10 mV amplitude, between 100 kHz and 10 mHz , and between -1.0 V and 0.7 V versus SCE.

3.3. Microstructural and chemical analysis

The morphology of the samples were observed using a field-emission scanning electron microscope (FESEM, Carl Zeiss SUPRA 55VP), and the crystallinity of the samples were analyzed using an X-ray diffractometer (XRD, Bruker AXS New D8 Advance). High resolution transmission electron microscope (HRTEM, JEOL JEM-3000F) were used to analyze morphology and crystallographic orientations. X-ray photoelectron spectroscopy (XPS, PHI 5000 VersaProbe, ULVAC-PHI) data were collected on the sputter-cleaned surface of Cu₂O/TiO₂ electrode. Raman spectroscopy (inVia Raman microscope, Renishaw) were performed to analyze the crystallinity of TiO₂ passivation layer after post-annealing process

CHAPTER 4

Design and Fabrication of Cu₂O Nanofiber Photocathode

4.1. Introduction

Mimicking the natural photosynthesis process, which produces fuel in the form of glucose from the reduction of carbon dioxide (CO₂) with light and water, has been considered to be the ultimate solution for the global warming problem [4.1-6]. However, in performing the reduction of CO₂ in an aqueous condition, the reduction of CO₂ has to compete with the reduction of water [4.7-9]. Making the CO₂ reduction more dominant was difficult because the rate-determining step of CO₂ reduction has a higher redox potential than that of water reduction [4.9, 10]; therefore, high selectivity was possible in an organic electrolyte where the system is innately free from the competition with the water reduction reaction [4.11]. However, the use of organic electrolytes is usually harmful to environment; therefore, water, an eco-friendly and earth-abundant electrolyte, is preferred [4.1, 2]. Herein, in an aqueous media, a faradic efficiency of 93% for CO₂ conversion to alcohol was achieved with mono-phase Cu₂O fabricated by precisely controlling d-orbital electrons of transition metals by designing and controlling the

kinetic and thermodynamic parameters during the annealing process.

Transition metals have various oxidation states because they have electrons in the d-orbital, which has small energy differences [4.12]. Therefore, transition metals have the redox property that electrons can easily be lost and obtained [4.13-17]. These metals can also bond with various anions, forming oxides, nitrides and sulfides with various compositions showing various material properties to be used as various applications in energy and environmental systems [4.4-7]. Especially, its oxide forms are widely used for photoelectrochemical catalysts because they show various band structures according to the oxidation states [4.18-21]. The oxidation states of transition metal oxide vary, for example, Mn shows 6 different oxidation states, Ti shows 3 oxidation states, and Cu shows 2 oxidation states. Among these oxides, copper oxide has been used as a photocathode for photoelectrochemical reaction by its p-type semiconducting character [4.22, 23]. Copper oxide mainly exists as two forms; cupric oxide (CuO) and cuprous oxide (Cu₂O) [4.24]. CuO has a monoclinic structure with the band gap of approximately 1.4 eV, Cu₂O has a cubic structure and has a band gap of approximately 2.4 eV [4.10]. Cu₂O has received considerable attention as a photocathode for photoelectrochemical CO₂ reduction [4.4] because Cu₂O has a band gap that can utilize the visible light of the sunlight spectrum and has a negative conduction band edge position, which generates high energy photo-induced electrons [4.10], and moreover, it is earth-abundant and non-toxic, which makes it environmentally friendly [4.25].

However, in CO₂ reduction by Cu₂O, few studies are reported in an aqueous electrolyte, and the studies observed low selectivity [4.26-28], which is mainly because the Cu₂O photocathode is usually mixed with other impurity phases such as CuO and Cu [4.23, 26-30]. When the Cu₂O phase is mixed with the CuO phase, CO₂ reduction is less favored because photogenerated electrons located at the conduction band edge of

Cu₂O can overcome the activation energy barrier of the CO₂ reduction while that of CuO cannot [4.10]. Therefore, fabrication of an electrode with mono-phase Cu₂O is necessary to achieve high selectivity for CO₂ reduction. However, precise control of the oxidation state of copper oxide is difficult because the apparent activation energies of reduction of CuO and Cu₂O are similar [4.31, 32]. Generally, the Cu₂O nanostructure is fabricated by reducing nanostructured CuO or oxidizing nanostructured Cu. However, the redox atmosphere was controlled only at atmospheric pressure or an inert gas atmosphere, such as Ar, and was not systematically controlled, which resulted in the phase mixing with CuO or metallic Cu [4.22, 23]. In the conventional reducing condition, the reduction of CuO to Cu₂O occurs, as well as the reduction of Cu₂O to Cu also occurs simultaneously [4.33], and in the oxidation process, Cu oxidizes not only to Cu₂O but also to CuO [4.34]. To date, there have been no reports for fabricating the Cu₂O phase by an annealing technique that systematically controls the annealing parameter considering thermodynamics and kinetics, and the control of the phase was attempted only in a piecemeal manner through trial and error.

Herein, by precisely controlling the gas atmosphere based on thermodynamic calculations, we successfully fabricate nanostructured copper oxide, which is transformed to mono-phase Cu₂O. By considering the driving force between the oxidation states of copper and the diffusion kinetics of oxygen, copper oxide is processed in a condition where Cu₂O is thermodynamically metastable. In that condition, we discovered the “kinetically processable window” such that the phase transformation is completed within a reasonable time scale while the Cu₂O maintains its phase without transforming into another phase. This process is only possible in the nanoscale material, because the gas-solid reaction by altering the gas atmosphere could only control the near-surface of the material.

For the fabrication of nanostructured Cu₂O, electrospinning is used, and the as-spun nanofibers are treated by the abovementioned annealing process that controls the thermodynamic and kinetic parameters. To utilize the Cu₂O nanofiber in a photocathode for a CO₂ reduction system, a hierarchical structure was applied to overcome the typical drawbacks. A Cu₂O thin film underlayer was adopted to block electron leakage from the current collector [4.23], and a TiO₂ passivation layer was also adopted to prevent the photocorrosion of the Cu₂O nanofibers [4.35]. High photocurrent density was achieved by adopting a nanofiber structured electrode, and the CO₂ was reduced to methanol at high selectivity. The technique of precisely controlling the oxidation states of the transition metal is broadly applicable to transition metal compounds that can be adopted to various catalytic applications.

4.2. Fabrication of mono-phase Cu₂O nanofiber

To perform the photoelectrochemical CO₂ reduction effectively, nanostructuring of the active material and controlling its phase precisely to the target phase is important. Therefore, in this section, the process to obtain the nanofiber structure and the strategy to transform the phase of copper oxide nanofiber into mono-phase Cu₂O are discussed.

4.2.1. Optimization of the electrospinning process

Electrospinning is a simple process that can produce a continuous 1-D nanostructure, which is beneficial of securing the diffusion length of minority carriers, and enhance transport properties of majority carriers. However, applying electrospun nanofibers to the photoelectrode has one great drawbacks: the adhesion of nanofiber to the conductive substrate. Electrospun nanofiber has long, cylindrical structures and thus they tends to entangle themselves rather than stick to the substrate. Therefore, optimization of the electrospinning process is a basic requirement for fabricating the copper oxide nanofiber structure. Figure 4.1 shows the four strategies which had been tried to enhance the adhesion of as-spun and calcined nanofiber to the FTO substrate.

First, the conductive substrate is changed to nanostructured substrate so that the nanofiber is entangled by the nanostructure of the substrate. Second, the surface of the FTO substrate is coated by the precursor solution that is the same with the electrospinning solution to interact with the as-spun nanofiber. Third, the solvent of the electrospinning solution is varied to the less-evaporating solvent so that the as-spun nanofiber is wetted to the surface of FTO. Last, the electrospinning time is varied to optimize the interaction and entanglement between nanofibers.

The nanostructured substrates were examined for the ITO nanorods and Ni foams each representing the vertical and porous nanostructures (Figure 4.2A-B). However, it showed negative effect on the adhesion, and the delamination of nanofiber stacking was occurred rather than entangling with the nanostructure of substrate, because the contact area between the nanofiber and the electrode was even reduced compared to the plane substrate.

Next, the use of the precursor solution for electrospinning as an adhesive layer has been attempted. The precursor solution was spin-coated onto the FTO substrate, and it was dried in an oven for 3 hours at 60 °C. The thickness of dried precursor solution layer shows thickness of about 50 nm (Figure 4.3A). As shown in Figure 4.3B, however, the precursor solution layer does not act as an adhesive layer and nanofiber was barely adhere to the substrate.

The solvent of the electrospinning solution was changed to less-evaporating solvent which has higher boiling temperature. The properties of the solvent used is listed in the Table 4.1. The solvent is varied to the mixture of ethanol and water, water only, and the mixture of water and dimethylformamide (DMF). As can be seen in Figure 4.4, when the ethanol is mixed with water, which has low boiling point, the delamination of nanofiber was occurred because the nanofibers are not wetted onto the FTO substrate due to the fast evaporation of the solvent during the electrospinning. When the water is only used as the solvent of electrospinning solution, the adhesion was improved but the drop of solution was observed. When the DMF is mixed with water, which has high boiling point, the nanofiber is well attached to the FTO substrate because the wettability of nanofiber is improved and thus the contact area between the as-spun nanofiber and the FTO substrate is increased.

The electrospinning time was optimized to achieve high mass loading of active

materials on the substrate. The electrospinning time is varied from 30 seconds to 10 minutes, and at 10 minutes, the nanofiber is delaminated. This is because if the nanofiber stack becomes too thick, the entanglement and the interaction between the nanofiber becomes too large so that the nanofiber stack is delaminated from the substrate. As can be seen in Figure 4.5, the maximum electrospinning time is 5 minutes that the nanofiber sticks to the substrate. In addition, the nanofiber is well attached at the FTO substrate after the calcination process.

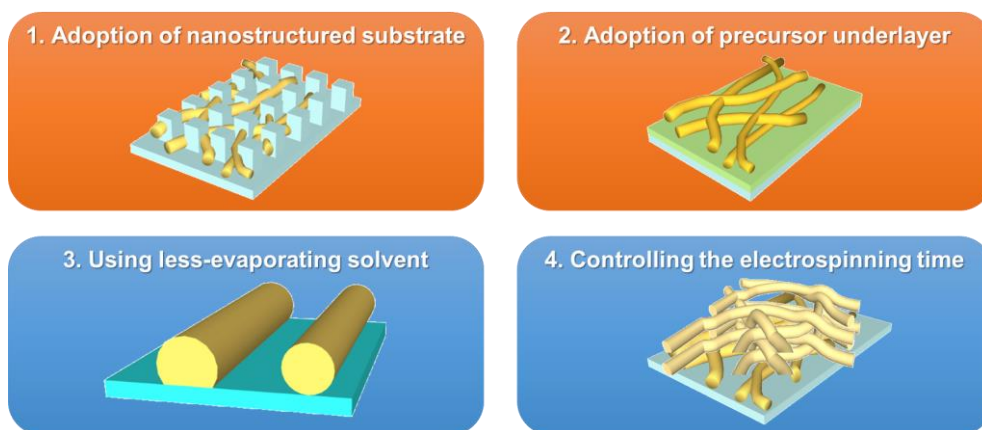


Figure 4.1 Four strategies to optimize the adhesion of nanofiber to the FTO substrate. The ineffective strategy and the effective strategy were divided into red box and blue box.

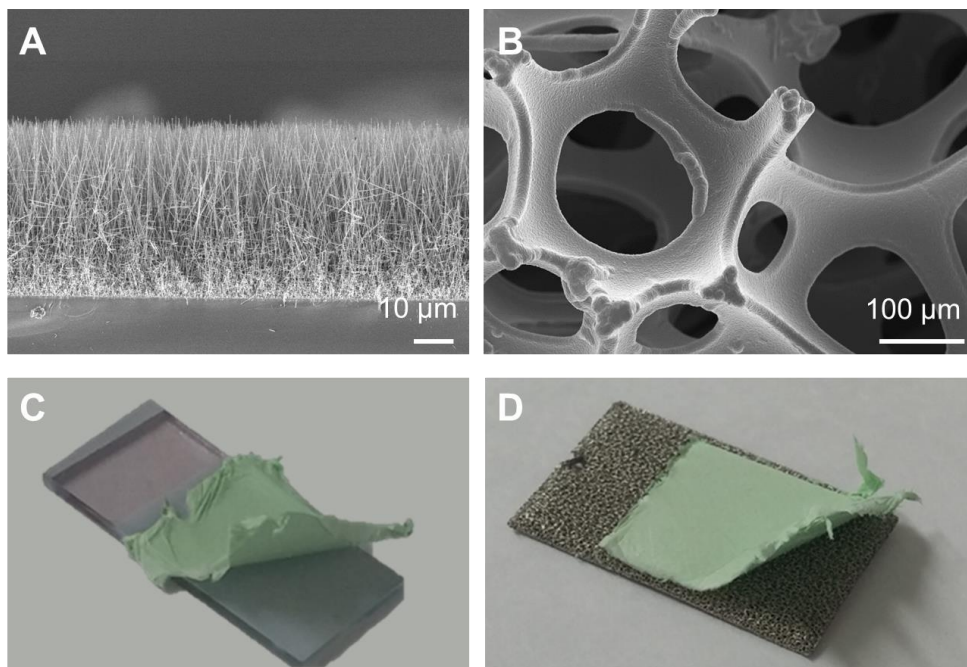


Figure 4.2 SEM micrograph of (A) ITO nanorods (B) Ni foams, showing vertical and porous nanostructure, respectively. Delamination of nanofiber from the (C) ITO nanorods and (D) Ni foams.

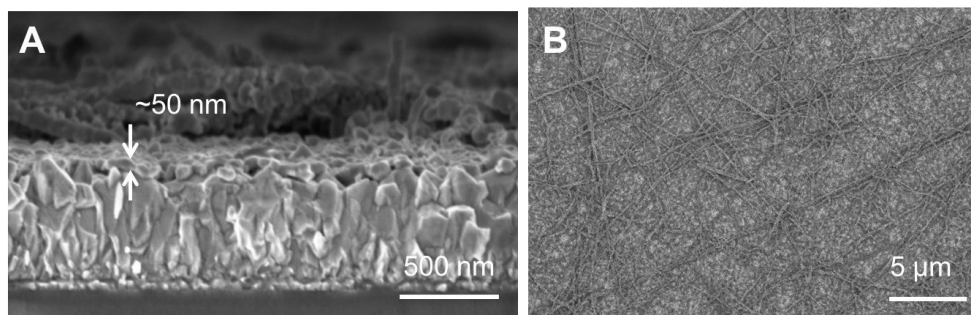


Figure 4.3 SEM micrograph of (A) cross-section of FTO substrate coated with precursor solution, and (B) electrospun nanofiber on the substrate.

Solvents	Ethanol	Water	Dimethylformamide (DMF)
Chemical formula	(C ₂ H ₅ OH)	H ₂ O	HCON(CH ₃) ₂
Molecular weight (g/mol)	46.07	18.00	79.09
Boiling point (°C)	78	100	158

Table 4.1 SEM micrograph of (A) cross-section of FTO substrate coated with precursor solution, and (B) electrospun nanofiber on the substrate.

Water 7 : EtOH 3	Water only	Water 8 : DMF 2
		
Delamination of nanofibers	Less delamination but solution drop forms	Well-attached nanofiber

Figure 4.4 Photograph of nanofiber on FTO glass with varying the solvent of an electrospinning solution.

	30 s	1m 30s	3 min	5 min	10 min
Before Calcination					
After Calcination					

Figure 4.5 Photograph of nanofiber on FTO glass with varying the electrospinning time from 30 s to 10 min. 5 min of electrospinning showed optimum thickness.

4.2.2. Design of the reaction path

As the nanofiber is well deposited on the FTO substrate by the optimization of electrospinning process in the previous section, now the polymer in the as-spun nanofiber should all be combusted because carbon residue does not have photocatalytic activity or good electron conductivity, which would impede the photoactivity of the electrode. The as-spun nanofiber consists of copper precursor and polymer backbone chain, and the oxidation of copper and the combustion of carbons in polymer should be occurred. Thus, the as-spun nanofiber could be considered as C-Cu-O system, and the reaction path to be transformed into mono-phase Cu₂O nanofiber is designed.

Since copper has three oxidation states, as-spun nanofiber could undergo three reaction paths to be transformed into mono-phase Cu₂O. First, the as-spun nanofibers could be directly oxidized to Cu₂O (direct oxidation path), second, the as-spun nanofibers could be reduced to Cu then re-oxidized to Cu₂O (reduction/oxidation path), and third, the as-spun nanofibers could be oxidized to CuO and the re-reduced to Cu₂O (oxidation/reduction path). As can be seen in Figure 4.6, these path are displayed in the Ellingham diagram, which shows the thermodynamic redox tendency of the elements at specific pO_2 , which is represented by the y-axis as a chemical potential of oxygen ($\Delta G_{O_2} = -RT\ln(pO_2)$) according to the temperature, hence demonstrating the thermodynamic stability region of each phase.

First, in the direct oxidation path, the breakdown of nanofiber is occurred as can be seen in Figure 4.7A. In this reaction path, the oxygen partial pressure is low so that the carbon is insufficiently combusted and the carbon residue is present between the copper oxide nanofibers. As the calcination precedes, the carbon residue combusts and it results the breakdown of nanofiber structure.

Second, in the reduction/oxidation path, carbons are incompletely combusted and the copper oxide agglomerations are formed on the carbon nanofiber. Since the oxygen partial pressure is even lower than that of direct oxidation path, the combustion of carbon is slower resulting the carbon nanofiber. Therefore, copper oxide cannot form nanofiber structure and it is agglomerated at the surface of carbon nanofibers (Figure 4.7B).

Third, in the oxidation/reduction path, the oxygen partial pressure was sufficiently high that enables the rapid combustion of carbons while oxidizing the copper acetate precursors. The uniform nanofiber structure of copper oxide is formed, which has the CuO phase due to the calcination at the atmospheric pressure (Figure 4.7C). Therefore, by following the oxidation/reduction reaction path, two-step calcination process is necessary to fabricate Cu₂O nanofiber as can be seen in Figure 4.8.

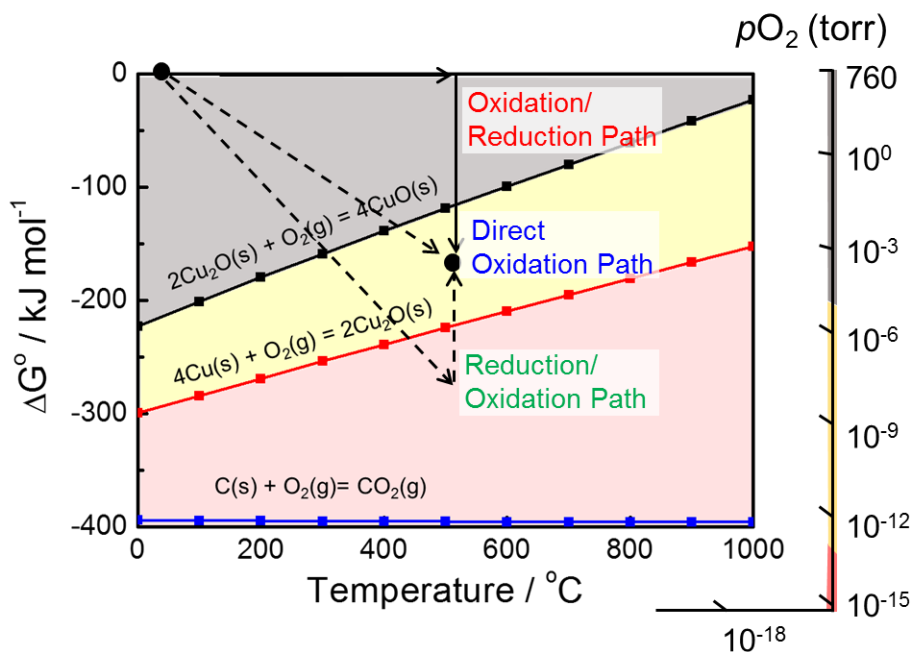


Figure 4.6 Ellingham diagram that shows the oxidation tendency of a phase according to the temperature and the chemical potential of oxygen. The reaction paths of transforming as-spun nanofibers into mono-phase Cu₂O are demonstrated.

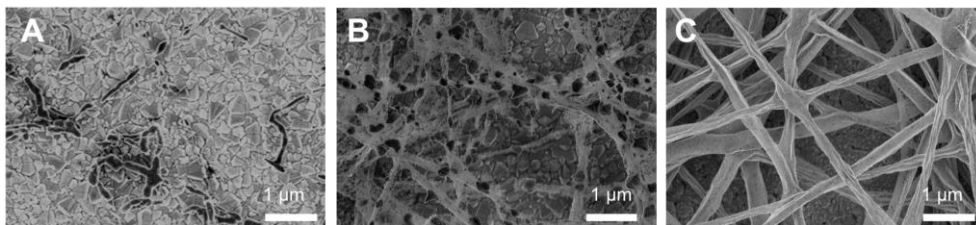


Figure 4.7 Morphology of nanofiber after calcination by three reaction paths: (A) direct oxidation path, (B) reduction/oxidation path, and (C) oxidation/reduction path. Only at the oxidation/reduction path, the uniform copper oxide nanofiber structure is formed.

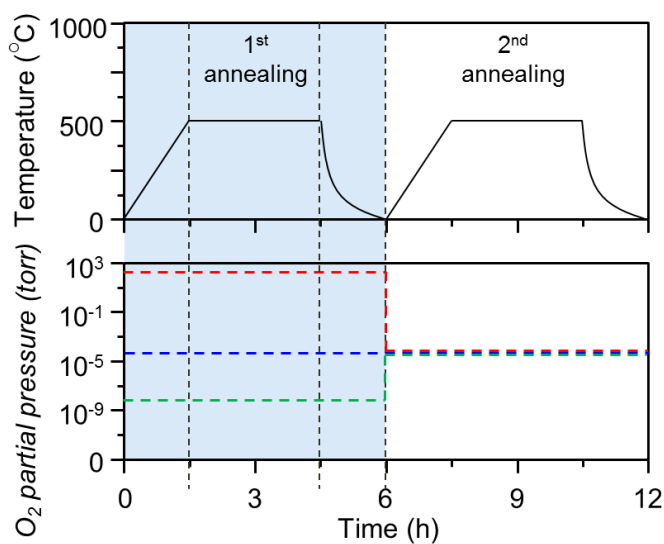
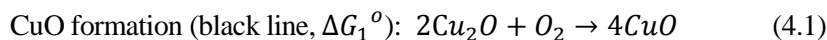


Figure 4.8 Heat treatment profile of calcination of as-spun nanofiber according to the reaction paths; red line, blue line, and green line indicates oxidation/reduction path, direct oxidation path, and reduction/oxidation path, respectively.

4.2.3. Design of the reaction parameter

As we have successfully fabricated copper oxide nanofiber having CuO phase, it should be further reduced to be transformed into mono-phase Cu₂O. The reduction of CuO to Cu₂O is controlled based on thermodynamic stability, as demonstrated in Figure 4.9. The representative reactions in the Cu-O system can be defined as follows.



At the gas atmosphere where ΔG_{O_2} is above the CuO formation ($\Delta G_1^o < \Delta G_{O_2}$), CuO is thermodynamically stable. At the gas atmosphere where ΔG_{O_2} is below the CuO formation and above the Cu₂O formation ($\Delta G_2^o < \Delta G_{O_2} < \Delta G_1^o$), Cu₂O is thermodynamically stable. At the gas atmosphere where ΔG_{O_2} is below the Cu₂O formation ($\Delta G_{O_2} < \Delta G_2^o$), Cu is thermodynamically stable. Using the bulk thermodynamic database, at the annealing temperature of 500 °C, the equilibrium p_{O_2} of reactions (4.1) and (4.2) are 7.15×10^{-6} Torr and 5.37×10^{-13} Torr, respectively (Figure 4.9).

In fact, as we are dealing with a nanoscale material, a surface energy term should be considered as an excess energy term to the bulk thermodynamic data [4.39-42]. By inverse calculation of the Gibbs free energy from the temperature and p_{O_2} conditions for the reduction of the nanoscale copper oxide [4.43, 44], ΔG_1^o should be shifted by ~ 37 kJ mol⁻¹ and ΔG_2^o should be shifted by ~ 110 kJ mol⁻¹ as demonstrated in Figure 4.10 and Table 4.2. Therefore, at the temperature of 500 °C, the equilibrium p_{O_2} for the reduction of CuO to Cu₂O is 2.4×10^{-3} Torr, and that for the reduction of Cu₂O to Cu is

1.1×10^{-5} Torr. From the calculated phase boundary conditions of pO_2 for each copper oxide, we established the pO_2 values for the experiment to the Cu₂O-stable condition: 250 μ Torr, and 50 μ Torr, and to the Cu-stable condition: 10 μ Torr, and 1 μ Torr, and the annealing time is controlled to 1, 3, 6, and 12 hours at each pO_2 to consider the reaction kinetics.

The pO_2 was controlled by blowing an Ar/O₂ gas mixture and pumping by a turbo molecular pump coupled with an angle valve that controls the rate of pumping out of the gas. As a representative case, the fraction of phases of copper oxides after annealing the CuO nanofiber at the annealing time of 3 hours at 500 °C with the given pO_2 conditions are shown in Figure 4.11. The XRD pattern was obtained and Rietveld analysis was performed to quantify the ratio of the phases according to the oxidation states of copper. After annealing at 250 μ Torr and 50 μ Torr, the resulting phase is a mixture of CuO and Cu₂O. At 10 μ Torr, all of the CuO is transformed into Cu₂O, and at 1 μ Torr, all the CuO is transformed into Cu. It should be noted that the mixture of CuO and Cu₂O is the result at Cu₂O-stable condition, while mono-phase Cu₂O is fabricated at pO_2 of 10 μ Torr, where Cu₂O is thermodynamically metastable. This finding indicates that not only thermodynamics but also kinetics should also be considered for the reactions at the nanoscale, which will be discussed later in more detail.

From the fraction of the phases of copper oxides according to the annealing time and the pO_2 (Figure 4.12), the transformation curve for the oxidation states of copper, starting from the CuO phase, was obtained (Figure 4.13). Labeled as CuO, Cu₂O, and Cu on the y-axis means that copper oxide is 100% transformed to each phase, *i.e.*, when the graph meets the horizontal line of Cu₂O, it means that all of the CuO is transformed into Cu₂O, and when the graph meets the horizontal line of Cu, it means that all of the Cu₂O is transformed into Cu.

Under the pO_2 of 250 μ Torr and 50 μ Torr, it was observed that the CuO was gradually reduced to Cu₂O as annealing time increases but was not completely transformed even after annealing for 12 hours. At the pO_2 of 10 μ Torr, mono-phase Cu₂O was observed at the annealing time of 3 hours. In the subsequent annealing time, Cu₂O is reduced further to Cu, and all of the Cu₂O is reduced to Cu after 12 hours of annealing. Under the pO_2 of 1 μ Torr, a mixture of Cu and Cu₂O was formed from the annealing time of 1 hour and was all reduced to Cu after 3 hours.

At all pO_2 , the graph follows a parabolic form and the data are fitted to the square root of time, indicating that all phase transformation kinetics are diffusion limited processes. The reduction of the CuO nanofiber is readily available by the surface reaction of weakly bonded O at the CuO surface turning into gaseous oxygen, which is replenished by the diffusion from the CuO/Cu₂O interface at the interior of the nanofiber [4.45]. The same kinetic consideration is done with the reduction of Cu₂O into Cu.

From the experimental results, the “kinetically processable window” of producing mono-phase Cu₂O which is the kinetic parameter in which Cu₂O maintains its phase without transforming into another phase, is discovered at the annealing time region of about 3 hours at a pO_2 of 10 μ Torr. The origin of the kinetically processable window is explained by the driving force of phase transformation between the oxidation states of copper according to each pO_2 . At the pO_2 of 50 μ Torr, 10 μ Torr, and 1 μ Torr, the Gibbs free energy values of Cu, Cu₂O, and CuO are calculated by the thermochemical database program (Factsage software), reflecting the shift due to the surface energy term caused by the nanosizing effect, as seen in Figure 4.14.

At 50 μ Torr, the Gibbs free energy of Cu₂O is the smallest, and at 10 μ Torr and 1 μ Torr, the Gibbs free energy of Cu is the smallest, indicating the most stable phases at each of the pO_2 values. The driving force of phase transformation can be derived by the Gibbs

free energy difference between each phase. The driving forces for the reduction of CuO to Cu₂O at 50 μ Torr, 10 μ Torr, and 1 μ Torr are 14.4 kJ, 35.1 kJ, and 47.7 kJ, respectively.

At 50 μ Torr, a Cu₂O-stable condition, the driving force for the phase transformation from CuO to Cu₂O is small. Therefore, it is difficult to reduce all of the CuO phase to the Cu₂O phase within a reasonable processing time. At 10 μ Torr, although the target phase Cu₂O is metastable and Cu is thermodynamically stable, the driving force for the phase transformation of CuO to Cu₂O is sufficiently large. Therefore, the parent phase, CuO, could be completely reduced to the target phase, Cu₂O. This condition might seem to be counterintuitive for producing Cu₂O because the produced Cu₂O will be subsequently reduced further to Cu. However, since the difference in the Gibbs free energy between Cu and Cu₂O is significantly smaller than that between Cu₂O and CuO, the transformation kinetics of reduction of Cu₂O into Cu is slower than that for CuO into Cu₂O.

Therefore, there is a kinetically processable window which is the condition of the kinetic parameter in which CuO is completely reduced to Cu₂O but not reduced further to Cu, although Cu₂O is thermodynamically metastable. If the p_{O_2} is too low, such as 1 μ Torr, the driving force of reduction of Cu₂O to Cu becomes also comparable to that of CuO to Cu₂O. Thus, the reduction of Cu₂O to Cu becomes so fast that the kinetically processable window where the mono-phase Cu₂O is present would disappear.

Therefore, considering the thermodynamics and kinetics of phase transformation, we were able to reduce all the CuO nanofibers into the mono-phase Cu₂O phase by discovering the kinetically processable window of the Cu₂O fabrication.

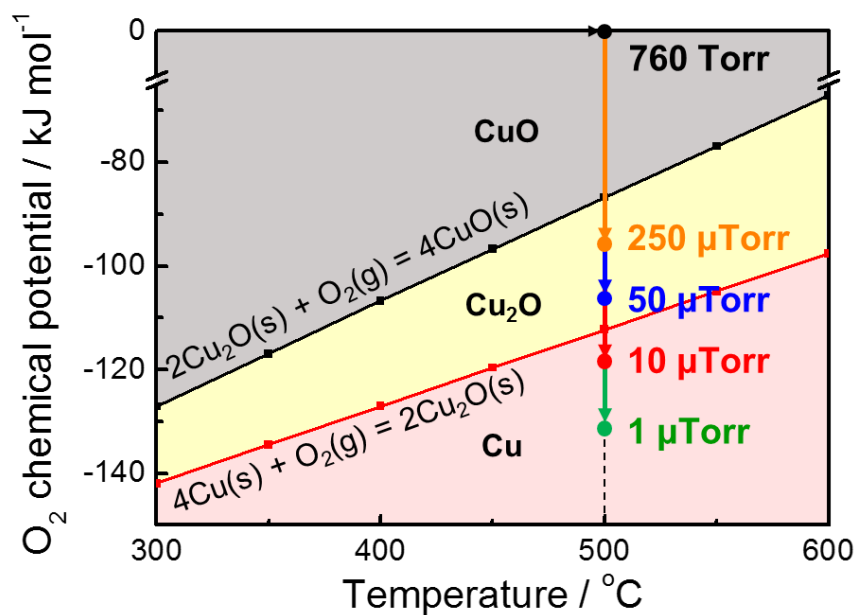


Figure 4.9 Diagram of chemical potential of oxygen showing the stable regions of CuO, Cu₂O, and Cu, according to the temperature. The experimental conditions of oxygen partial pressure are indicated.

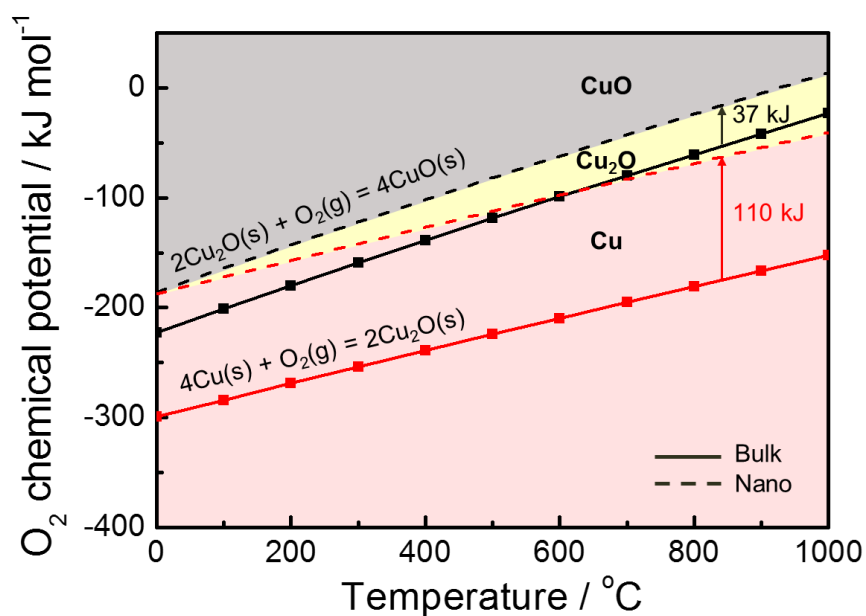


Figure 4.10 Diagram of chemical potential of oxygen showing the stable regions of CuO, Cu₂O, and Cu, according to the temperature. The experimental conditions of oxygen partial pressure are indicated.

	Temperature	pO_2 (Torr)	ΔG^o (nanoscale)	ΔG^o (bulk)
Equilibrium of CuO/Cu ₂ O (ΔG_1^o)	573 K	1×10^{-8}	-122 kJ	-159 kJ
Equilibrium of Cu ₂ O/Cu (ΔG_2^o)	573 K	7.5×10^{-11}	-142 kJ	-254 kJ

Table 4.2. Comparison between calculated equilibrium chemical potential of oxygen for the phase transformation of CuO to Cu₂O and Cu₂O to Cu.

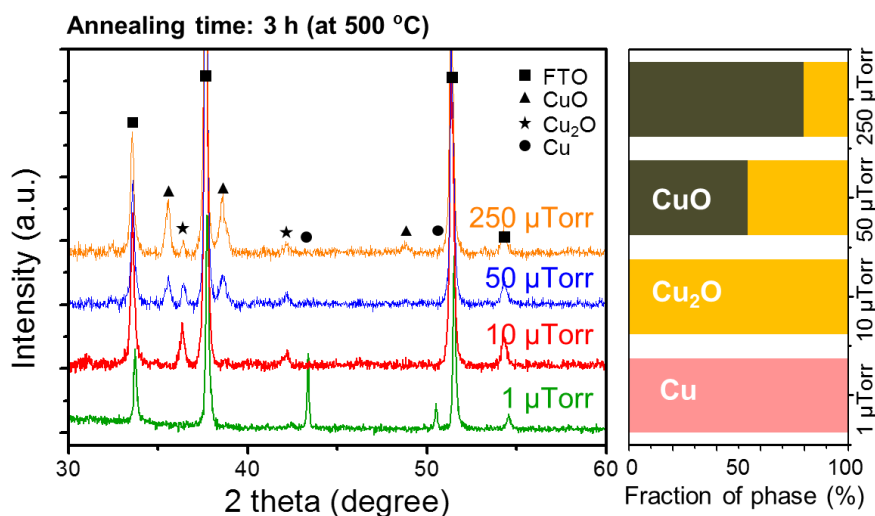


Figure 4.11 XRD pattern of copper oxides that are annealed at 500 °C for 3 hours at pO_2 of 250 μTorr, 50 μTorr, 10 μTorr, and 1 μTorr. Fraction of phases are quantified by Rietveld analysis.

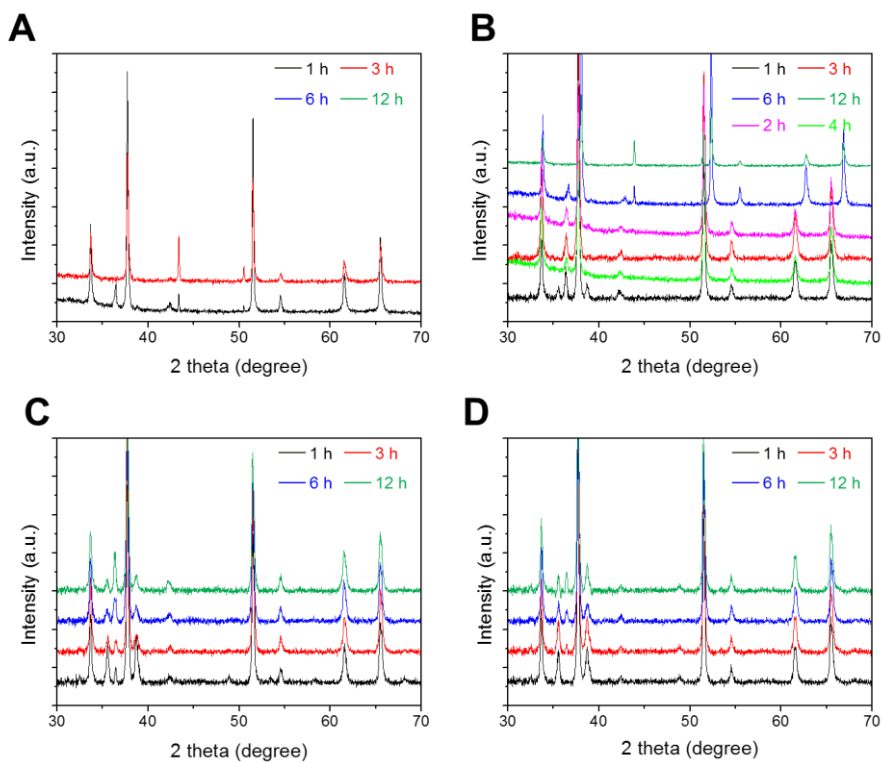


Figure 4.12 XRD pattern for the CuO nanofibers which are annealed at (A) 1 μ Torr, (B) 10 μ Torr, (C) 50 μ Torr, and (D) 250 μ Torr for 1 – 12 hours, respectively.

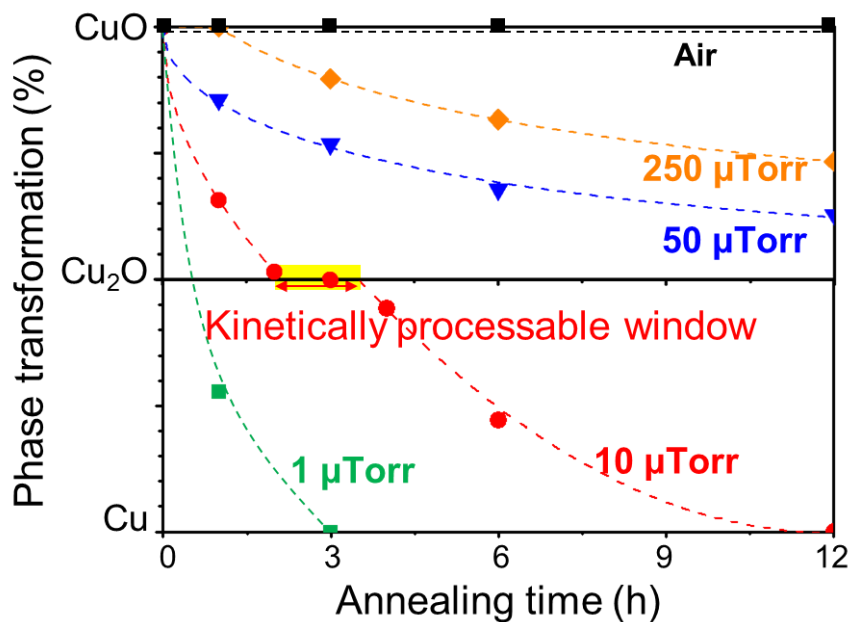


Figure 4.13 Transformation curve of reduction of CuO nanofiber according to the pO_2 of 250 μTorr , 50 μTorr , 10 μTorr , and 1 μTorr at 500 °C showing the kinetically processable window of mono-phase Cu₂O fabrication.

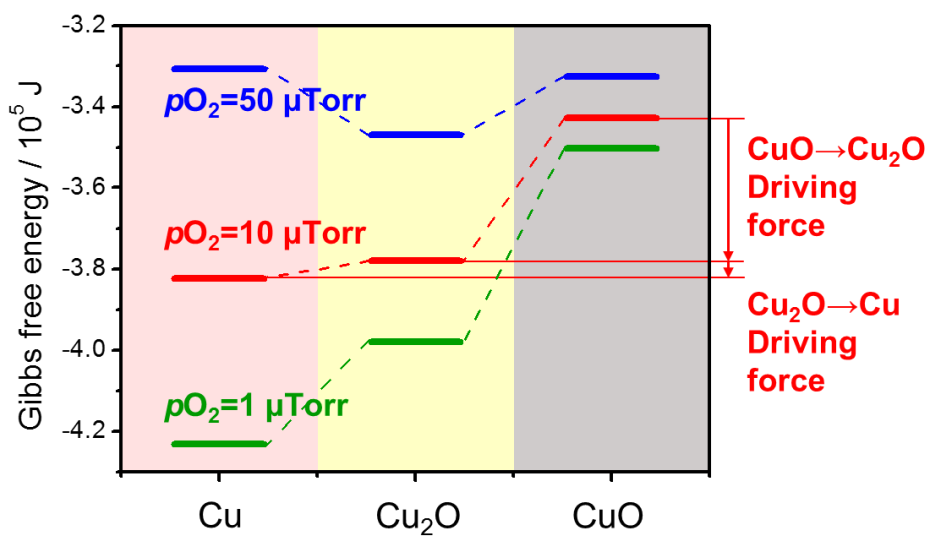


Figure 4.14 Calculation of the Gibbs free energy of CuO, Cu₂O and Cu according to the p_{O_2} of 50 μTorr , 10 μTorr , and 1 μTorr at 500 °C, indicating the driving force of phase transformation which is the difference in the Gibbs free energy between copper oxides.

4.3. Fabrication of the hierarchical structure

Although the mono-phase Cu₂O nanofiber is successfully produced, there are several problems in applying the Cu₂O nanofiber to an actual PEC system. First, the fluorine-doped tin oxide (FTO) substrate should not be directly exposed to the electrolyte. When the FTO is directly exposed to the electrolyte, it shunts the device, resulting in leakage of electrons from the substrate, which degrades the photoactivity of the photoelectrode [4.23]. Second, the Cu₂O is not stable in the reducing environment because the reduction potential of Cu₂O to metallic Cu is more negative than that of the CO₂ reduction [4.35]. Therefore, passivation of the Cu₂O electrode from the electrolyte is required to prevent the Cu₂O from being reduced to Cu instead of CO₂ reduction on Cu₂O.

To solve the above issues, a hierarchical structure which consists of a Cu₂O thin film underlayer, a mono-phase Cu₂O nanofiber, and a TiO₂ passivation layer was applied. A hierarchically structured photocathode is fabricated as mentioned before in the experimental section, and the final structure is described in Figure 4.15.

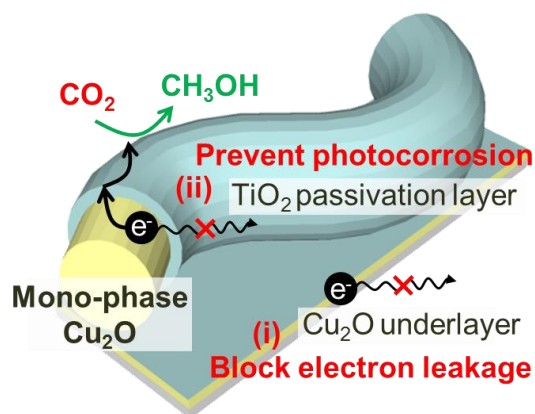


Figure 4.15 Schematic of the hierarchical structure of the Cu₂O nanofiber.

4.3.1. Optimization of Cu₂O thin film underlayer

To passivate the FTO substrate, the Cu film is deposited as an underlayer, and it well covers the FTO substrate as can be seen in Figure 4.16. Since the annealing process that the Cu film experiences is the same as the as-spun nanofiber, the film is first oxidized to CuO and then it is reduced to Cu₂O. To transform the CuO film into mono-phase Cu₂O under the same annealing conditions at the kinetically processable window of the nanofibers, optimization of the thickness of the film is necessary.

The thickness of the Cu deposited was varied to 20 nm, 50 nm, and 100 nm, which showed no differences in microstructure (Figure 4.16B-D). Through the XRD analysis, the thin film underlayer with a thickness of 20 nm had a mono-phase Cu₂O, whereas the larger thicknesses of 50 nm and 100 nm showed a mixture of CuO and Cu₂O (Figure 4.17). In the given kinetically processable window, the oxygen generated by the reduction of CuO to Cu₂O can all diffuse out in the thickness of 20 nm, whereas the generated oxygen inside the thin film of a larger thickness cannot diffuse out sufficiently.

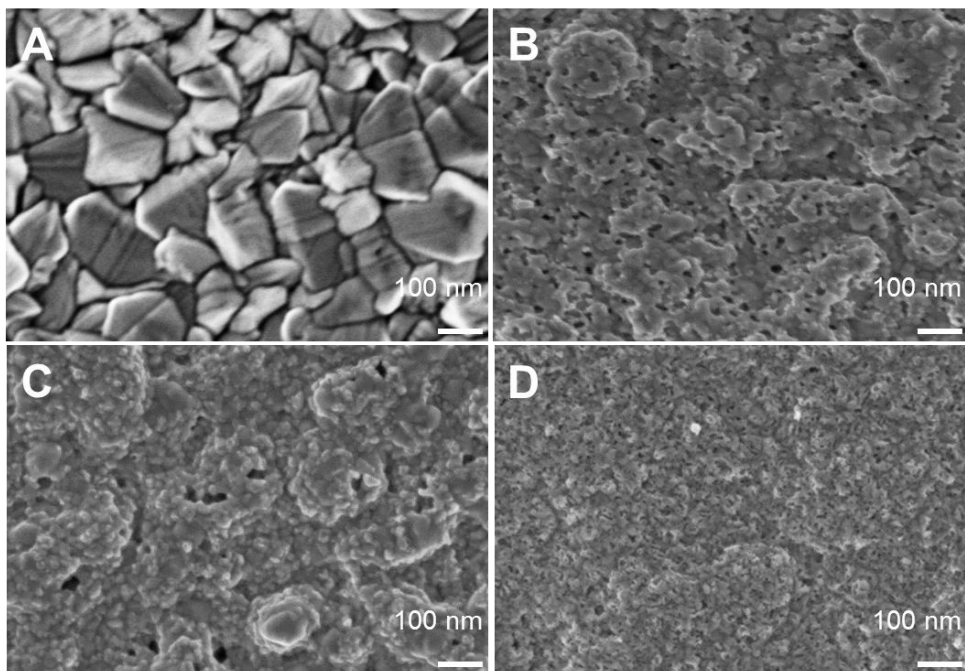


Figure 4.16 Morphology of the Cu_2O underlayer with respect to the thickness of (A) 0 nm, (B) 20 nm, (C) 50nm, and (D) 100nm.

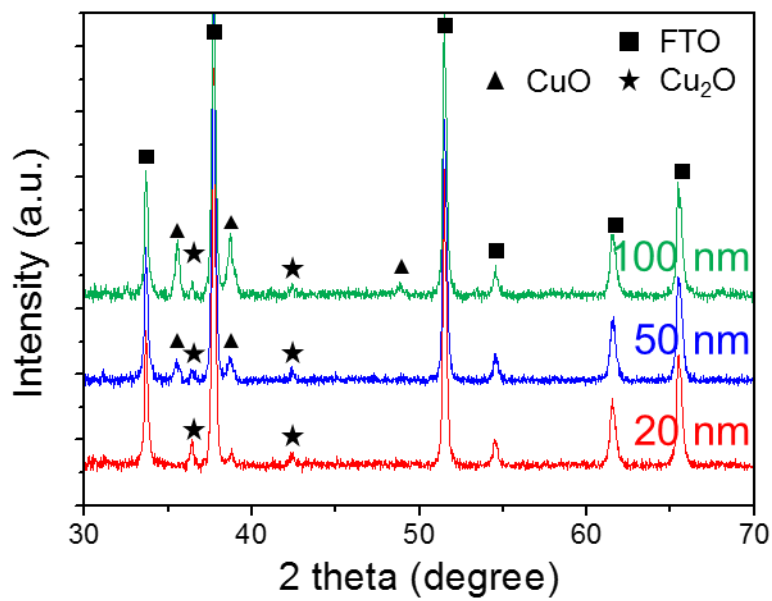


Figure 4.17 Phase of the Cu₂O underlayer with respect to the thickness of 20 nm to 100 nm.

4.3.2. Optimization of TiO₂ passivation layer

Next, to passivate the Cu₂O nanofiber, TiO₂ was deposited as a passivation layer. The TiO₂ layer is uniformly deposited without any pinholes as can be seen in the SEM and TEM (Figure 4.18A-B). The lattice fringe and FFT image indicates that the core is crystalline Cu₂O, and the shell is amorphous TiO₂ (Figure 4.18C-D). HAADF and EDS mapping were also done to confirm the core-shell structure of Cu₂O and TiO₂ (Figure 4.19). Generally, in such an amorphous passivation layer, many defects, such as surface traps, are present on the surface, which limits the photoactivity. Therefore, to annihilate the defects from the TiO₂ passivation layer, a post annealing process after ALD coating was performed. We adjusted the *p*O₂ to 10 μTorr so as not to alter the Cu₂O phase during post-annealing, and varied the annealing temperature to 400 °C, 450 °C, and 500 °C, with the annealing time of 1 hour.

The annihilation of defects can be expressed by an increase in crystallinity, and the crystallinity of the post-annealed TiO₂ passivation layer was observed by Raman spectroscopy (Figure 4.20). A Raman shift near 151 cm⁻¹ indicates both the crystalline TiO₂ and Cu₂O, and the Raman shift near 218 cm⁻¹ indicates the crystalline Cu₂O. Comparing the spectra, the peak intensity at 151 cm⁻¹ was increased after annealing at 500 °C and 450 °C, whereas annealing at 400 °C did not increase the peak intensity at 151 cm⁻¹.

It means that crystallization occurred from 450 °C, and annealing at a temperature lower than 450 °C is insufficient to crystallize the TiO₂ passivation layer. However, small aggregated TiO₂ nanoparticles were observed on the nanofiber at the annealing temperature of 500 °C, while an annealing temperature of 450 °C shows no aggregation, indicating that the TiO₂ passivation layer is stable up to 450 °C (Figure 4.21). In addition,

after the post-annealing at 450 °C with the $p\text{O}_2$ of 10 μTorr for 1 hour, the phase of the copper oxide was not altered and maintained mono-phase Cu_2O which was confirmed by XPS (Figure 4.22A) and XRD (Figure 4.22B).

The TiO_2 passivation layer requires more control besides eliminating defects while maintaining its structure to provide selectivity for CO_2 reduction. The thickness of TiO_2 passivation layer is crucial for the selectivity because it greatly affects the potential of the electrons used for the CO_2 reduction.

To selectively reduce the CO_2 , active sites for the CO_2 reduction must be present on the surface of the electrode, and electrons that have sufficient potential to perform the CO_2 reduction should be supplied on the active site. It is reported by several groups that the Ti^{3+} site in TiO_2 is both active for water reduction as well as CO_2 reduction to methanol [4.46-49]. The TiO_2 layer in this electrode system is annealed at an oxygen deficient atmosphere, as mentioned previously, and the generation of the Ti^{3+} site in the TiO_2 layer was confirmed by X-ray photoelectron spectroscopy (XPS) (Figure 4.23). Thus, both water reduction and CO_2 reduction can occur, however, whether which reaction occurs at the surface Ti^{3+} site is determined by the potential of the electrons transferred from the photocatalyst to the surface active site.

The influence of the TiO_2 thickness on the potential of electrons used for CO_2 reduction in the $\text{Cu}_2\text{O}/\text{TiO}_2$ system can be suggested through its band diagrams, which are demonstrated in Figure 4.24 considering its band gaps measured by UV-vis spectroscopy (Figure 4.25). Since the activation energy barrier of the CO_2 reduction is higher than that of water reduction, electrons that have insufficient potential to overcome the energy barrier of CO_2 reduction perform water reduction [4.9, 10]. Therefore, a high electron potential is necessary for selective CO_2 reduction in an aqueous condition. As demonstrated in Figure 4.24A, photogenerated electrons from the Cu_2O conduction

band edge would have sufficient potential to overcome the energy barrier of the CO₂ reduction, which traverse through the TiO₂ passivation layer to reach the interface with the electrolyte. If the TiO₂ layer is sufficiently thin, the photogenerated electrons from the Cu₂O do not equilibrate with the TiO₂ energy band level and directly traverse to the interface with the electrolyte [4.46, 47]. However, for the thick TiO₂ layer, as shown in Figure 4.24B, the photogenerated electrons from the Cu₂O equilibrate with the TiO₂ energy band level, resulting in insufficient electron potential to reduce the CO₂. Also, in a previous report by Y. Chen et al., the thin TiO₂ passivation layer deposited by the ALD process did not affect the selectivity of the electrochemical reaction, and only enhanced the stability of the electrode [4.50].

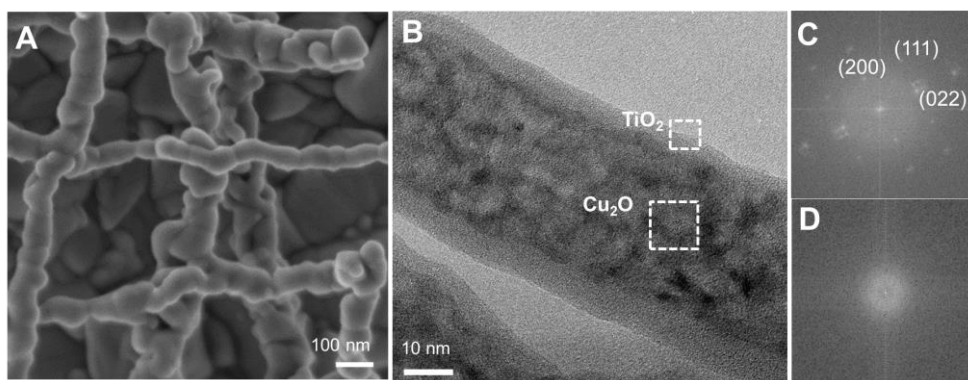


Figure 4.18 (A) SEM micrograph of the photocathode. (B) TEM image of the Cu₂O nanofiber after depositing 5 nm of TiO₂ by ALD. Diffraction pattern for (C) Cu₂O nanofiber and (D) TiO₂ passivation layer.

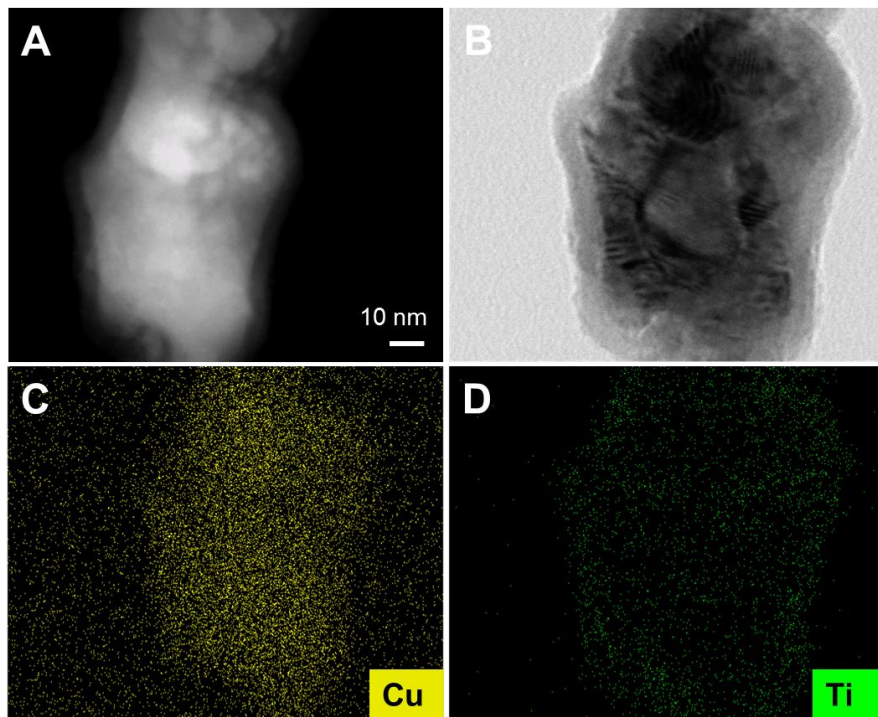


Figure 4.19 (A) HAADF image of Cu_2O nanofiber with TiO_2 passivation layer. Image of EDS mapping of TiO_2 -coated Cu_2O nanofiber. (B) Electron image, (C) mapping for Cu, and (D) mapping for Ti.

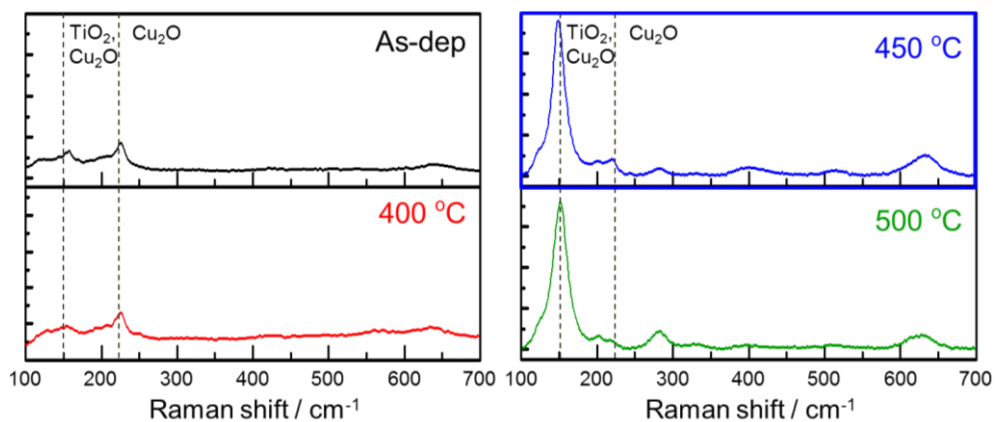


Figure 4.20 Raman spectrum of a TiO_2 -coated nanofiber with varying annealing temperatures from 400 °C to 500 °C. The crystallization of TiO_2 begin at 450 °C.

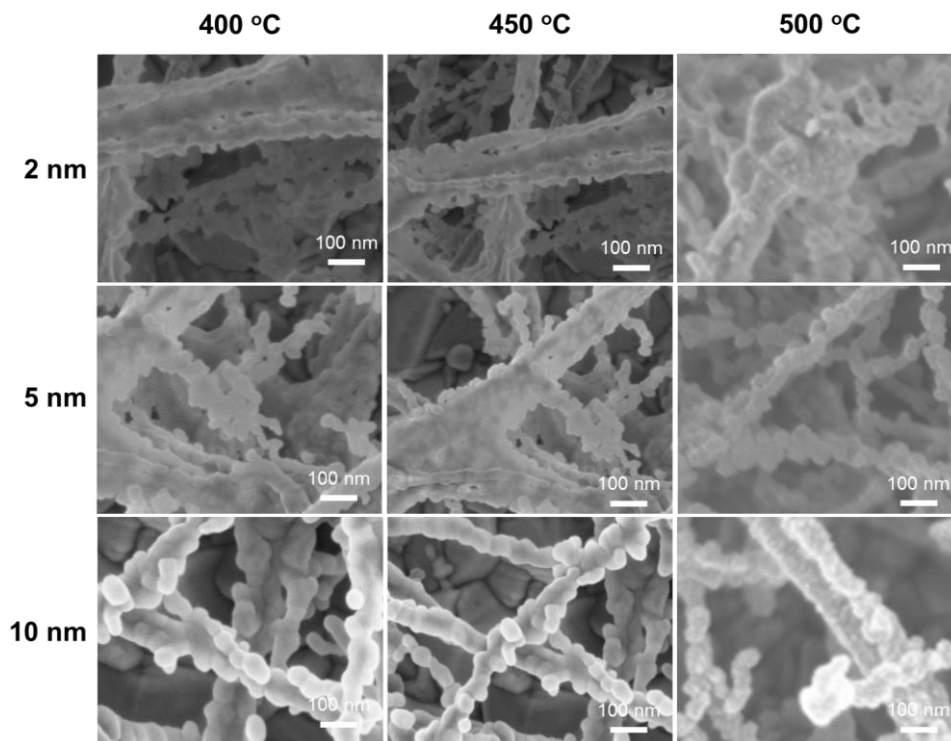


Figure 4.21 Morphology of nanofiber with post-annealed TiO_2 layer. Thickness of TiO_2 and annealing temperatures are varied from 2 nm – 10 nm and 400 °C – 500 °C, respectively.

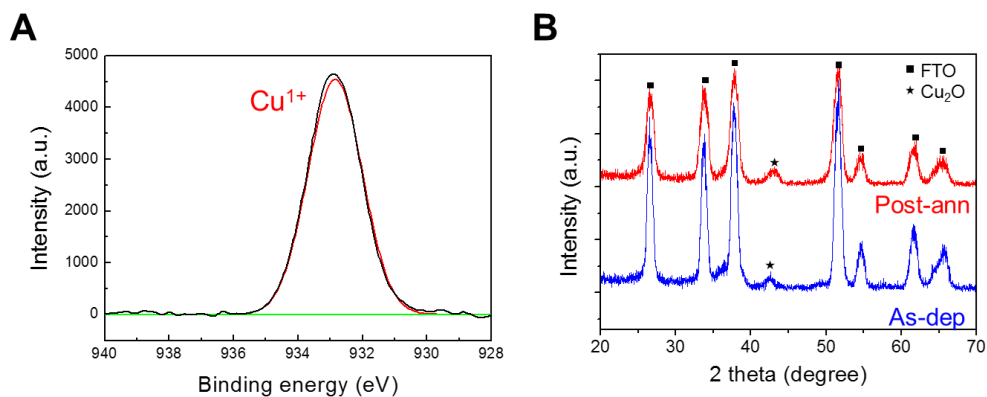


Figure 4.22 (A) X-ray photoelectron spectroscopy (XPS) profile for the Cu_2O nanofiber coated with 5 nm TiO_2 , which was annealed at 450 °C for 1 hour at $p\text{O}_2$ of 10 μTorr . (B) Phase of the electrode before and after the post-annealing of TiO_2 passivation layer; both showing mono-phase Cu_2O .

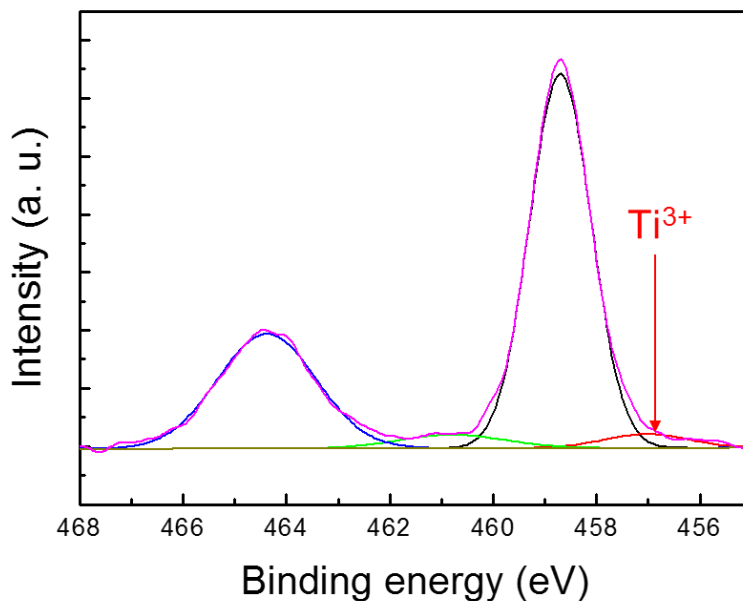


Figure 4.23 X-ray photoelectron spectroscopy (XPS) profile for the Cu₂O nanofiber coated with 5 nm TiO₂, which was annealed at 450 °C for 1 hour at *p*O₂ of 10 μTorr. It shows Ti³⁺ state which is the active site for CO₂ reduction.

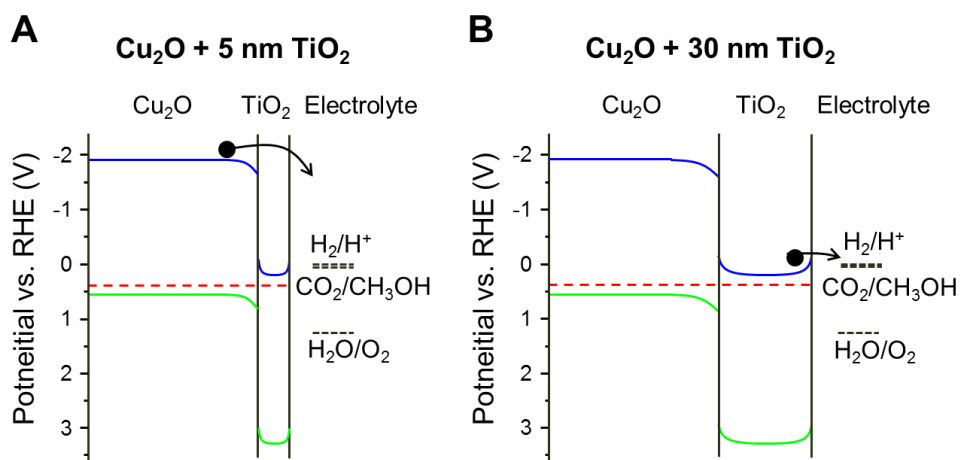


Figure 4.24 Band diagram of the $\text{Cu}_2\text{O}/\text{TiO}_2$ system equilibrated at 0.4 V vs. RHE with different thickness of the TiO_2 passivation layer. (A) Cu_2O nanofiber passivated with 5 nm thick TiO_2 , and (B) with 30 nm thick TiO_2 .

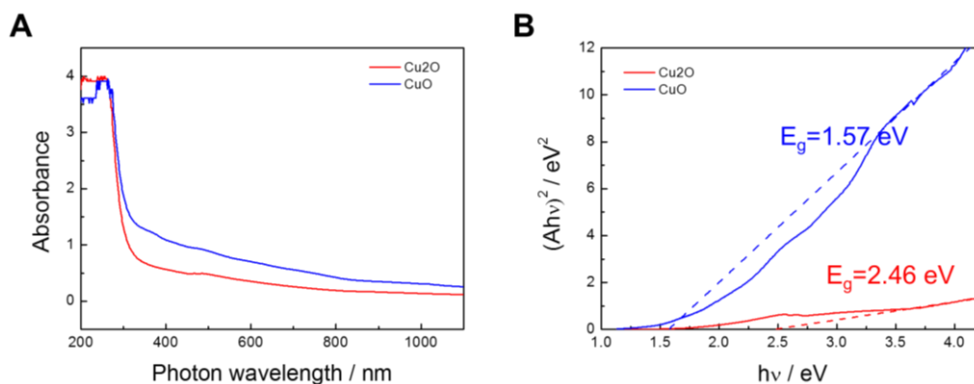


Figure 4.25 UV-visible spectra for the CuO and Cu_2O nanofiber showing band gaps of 1.57 eV and 2.46 eV, respectively for the CuO and Cu_2O .

4.4. Summary

Mono-phase Cu₂O nanofiber was fabricated through the electrospinning process, and followed thermodynamically programmed calcination process. The electrospinning process is optimized to improve the poor adhesion of nanofibers to the FTO substrate due to small contact area between them. Using the solvent with high boiling point and controlling the electrospinning time to 5 minutes were effective at improving the adhesion.

Then we controlled the reaction path of calcination of as-spun nanofibers to combust carbons and oxidize Cu precursor while maintaining its nanofiber structure. As-spun nanofibers should pass through CuO phase in order to maintain its nanofiber structure because carbon should be combusted rapidly not to interfere the formation of copper oxide nanofibers. Then the CuO nanofibers are calcined by thermodynamically programmed calcination process of which the parameter of calcination is calculated based on thermodynamics. We discovered the kinetically processable window of fabrication of mono-phase Cu₂O by comparing the Gibbs free energy of each oxidation state of copper at the given pO_2 . In the kinetically processable window, CuO is all reduced to Cu₂O but Cu₂O is not reduced to Cu, hence demonstrating the mono-phase Cu₂O.

To use the Cu₂O nanofiber as a photocathode, Cu₂O thin film underlayer is deposited to block the electron leakage from FTO, and TiO₂ passivation layer is deposited by ALD process to prevent the photocorrosion of Cu₂O into Cu. 20 nm thickness of Cu₂O thin film uniformly covered the FTO substrate and enhanced the photoactivity dramatically, and TiO₂ improved the photostability of Cu₂O nanofibers.

CHAPTER 5

Photoelectrochemical performance of Cu₂O photocathode

5.1. Introduction

In Chapter 4, we have successfully fabricated mono-phase Cu₂O nanofiber, of which oxidation state is expected to be crucial for the selectivity of CO₂ reduction reaction. Also, the hierarchical structure to adopt Cu₂O nanofiber to the photocathode, which consists of Cu₂O underlayer and TiO₂ passivation layer is developed to optimize the photoactivity and photostability.

The purpose of this chapter is analyze the effect of oxidation states of copper on the selectivity of CO₂ reduction, as well as the effect of underlayer and passivation layer on the photoactivity and photostability. In addition, the role of TiO₂ passivation layer on the selectivity of CO₂ reduction is studied.

5.2. Photoelectrochemical performances

5.2.1. Effect of Cu₂O thin film underlayer

Cu₂O thin film underlayer is introduced to block the electron leakage from the FTO substrate. When the FTO substrate is directly exposed to the electrolyte, it shunts the device by recombining electrons. The photocurrent density of the Cu₂O nanofiber electrode without the underlayer shows a low photocurrent density with a significant dark current, which indicates the leakage of electrons from the FTO substrate [5.1]. After the adoption of the Cu₂O underlayer, the photocurrent density increases dramatically, induced by blocking of the electron leakage shown as the negligible dark current in Figure 5.1. Therefore, the nanofiber electrode could effectively perform the electrochemical reaction only if the electron leakage from the conductive substrate is blocked by the underlayer. The underlayer thickness of 20 nm sufficiently prevents the electron leakage from the FTO substrate, and the electron blocking effect was the same with the thicknesses of 20 nm to 100 nm (Figure 5.2).

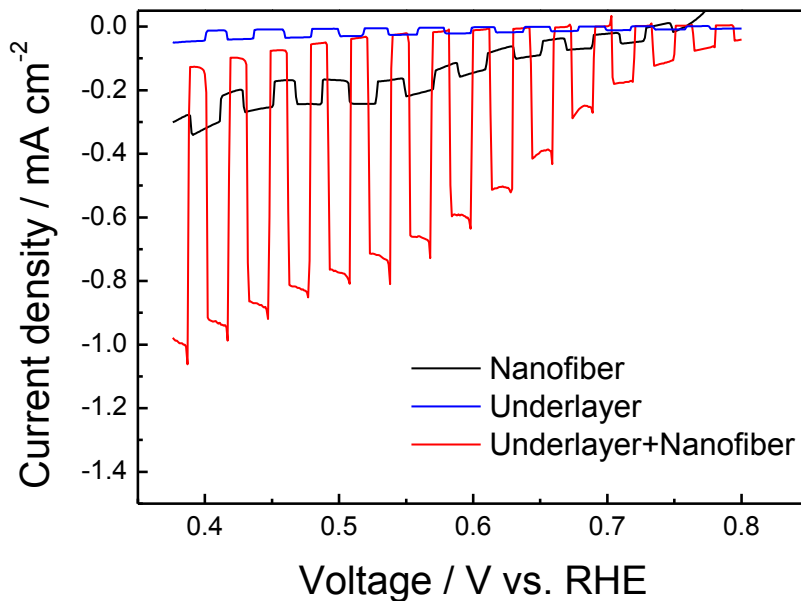


Figure 5.1 The effect of the underlayer on the photocurrent density. Underlayer enhances photoactivity of the nanofiber by blocking the electron leakage.

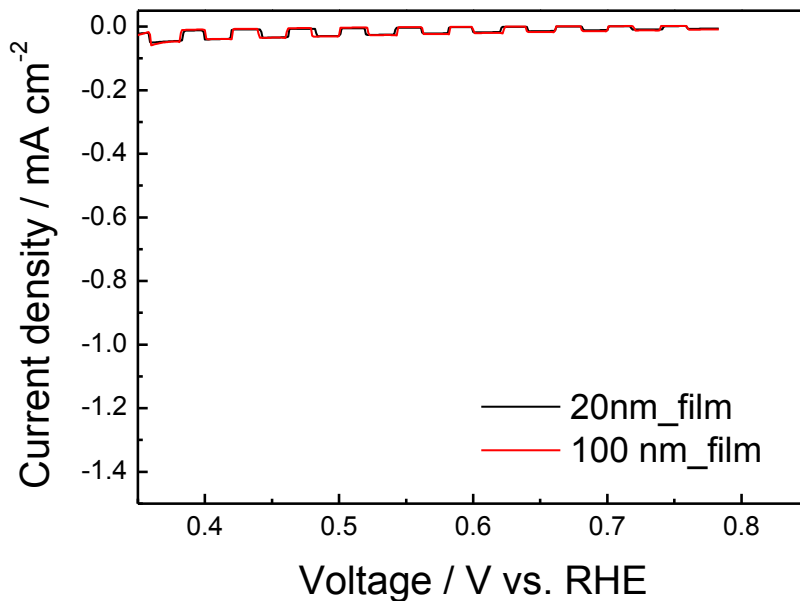


Figure 5.2 Photocurrent density curve for the 20 nm and 100 nm thick Cu_2O underlayer. Both film effectively blocks the electron leakage from FTO.

5.2.2. Effect of TiO₂ passivation layer

The TiO₂ passivation layer is deposited by ALD process to prevent the photocorrosion of Cu₂O into metallic Cu, which occurs in the reducing environment. Now, the effect of the TiO₂ passivation layer on photostability is tested at 0.4 V vs. RHE (Figure 5.3). The bare Cu₂O nanofiber without the TiO₂ passivation layer was immediately photoreduced to metallic copper, and the photocurrent density was dropped to nearly zero within a few seconds. Therefore, the TiO₂ passivation layer was deposited, but the as-deposited TiO₂ passivation layer significantly degraded the photocurrent density by its amorphous character, which indicates that there are many surface electron trap sites. However, after the post-annealing of TiO₂ passivation layer, the photocurrent density is dramatically enhanced by the annihilation of defects in TiO₂ amorphous layer by the crystallization with the post-annealing process. The photostability according to the TiO₂ thickness is also tested in Figure 5.4, and the thickness of 5 nm showed the best performance. Also, it is confirmed by GIXRD analysis that Cu₂O nanofiber showed no Cu peak after stability test, which is the resultant phase of photocorrosion (Figure 5.5).

The TiO₂ passivation layer not only enhances the photostability, but it also has to act as an active site for CO₂ reduction because TiO₂ meets directly with the electrolyte and CO₂. The possibility of Ti³⁺ site as an active site for CO₂ reduction is investigated at the previous chapter, and it was also mentioned that the thickness of TiO₂ would affect the selectivity of CO₂ reduction. Therefore, the effect of the thickness of the TiO₂ passivation layer on the selectivity of CO₂ reduction in aqueous condition is analyzed in Figure 5.6. While the Cu₂O electrode coupled with 5-nm thick TiO₂ performed the CO₂ reduction dominantly in the aqueous media, the Cu₂O electrode coupled with the 30-nm thick TiO₂ passivation layer performed water reduction with a faradic efficiency of 96%.

This is because, as described before, when the thickness of TiO₂ becomes too thick, high potential electrons photogenerated from Cu₂O cannot traverse the TiO₂ layer without the equilibration with TiO₂ energy level, which does not have sufficient potential to overcome the activation energy for CO₂ reduction.

The influence of the thickness of the TiO₂ passivation layer on the electron potential is confirmed by an electrochemical impedance spectroscopy (EIS) measurement for the bare Cu₂O nanofiber, the Cu₂O nanofiber with a 5-nm thick TiO₂ passivation layer, and the Cu₂O nanofiber with a 30-nm thick TiO₂ passivation layer. The equivalent circuit model was introduced based on previous EIS studies for photoelectrodes [5.2] (Figure 5.7).

The capacitance of the bulk Cu₂O/TiO₂ system, C_{bulk} , was extracted from fitting the measured frequency response of impedance of the electrode with increasing the applied potential (Figure 5.8). Mott-Schottky plots (C_{bulk}^{-2} vs. potential) were constructed, and the flat-band potentials for the Cu₂O/TiO₂ system can be derived by its intercept with the potential axis [5.3]. Flat band potentials for the bare Cu₂O and the Cu₂O with a 5-nm thick TiO₂ passivation layer are quite similar with the value of 0.512 V vs. RHE and 0.515 V vs. RHE, respectively, but the Cu₂O with a 30-nm thick TiO₂ passivation layer has a larger value of 0.657 V vs. RHE as demonstrated in Figure 5.9. It can be seen from the flat-band potential value that the band bending at the electrolyte interface of the Cu₂O with a 5-nm thick TiO₂ passivation layer is equal to that of the bare Cu₂O, while the Cu₂O with a 30-nm thick TiO₂ passivation layer shows a different band bending nature. Therefore, the electrons in the Cu₂O with a 5-nm thick TiO₂ passivation layer are transferred by the same behavior as the electrons of the bare Cu₂O are transferred to the interface, whereas the electrons in the Cu₂O with a 30-nm thick TiO₂ passivation layer experience equilibration with the TiO₂ energy level. Additionally, the diffusion of Cu

into the TiO_2 layer during annealing of $\text{Cu}_2\text{O}/\text{TiO}_2$ did not occurred, which is confirmed by XPS (Figure 5.10), as TiO_2 was successively used as the diffusion barrier for the Cu in the harsher condition [5.4].

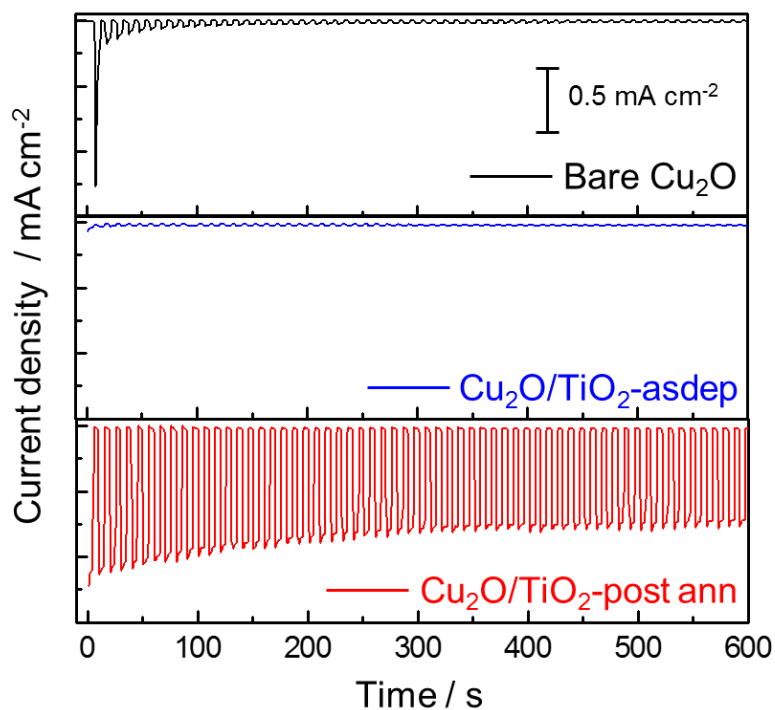


Figure 5.3 Photocurrent density curve for the 20 nm and 100 nm thick Cu_2O underlayer. Both film effectively blocks the electron leakage from FTO.

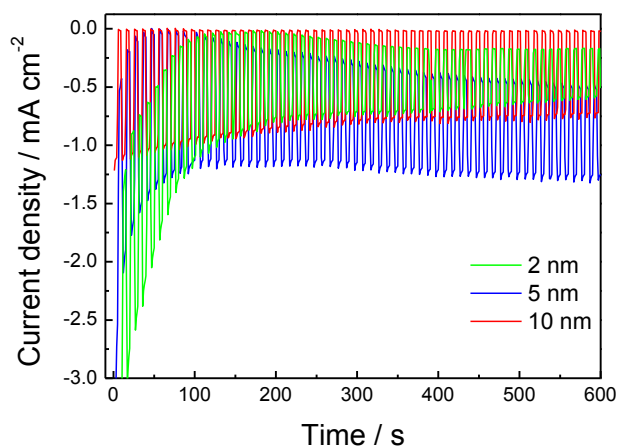


Figure 5.4 Photocurrent density curve for the thickness variation of TiO_2 passivation layer. TiO_2 with 5 nm thickness showed best performances.

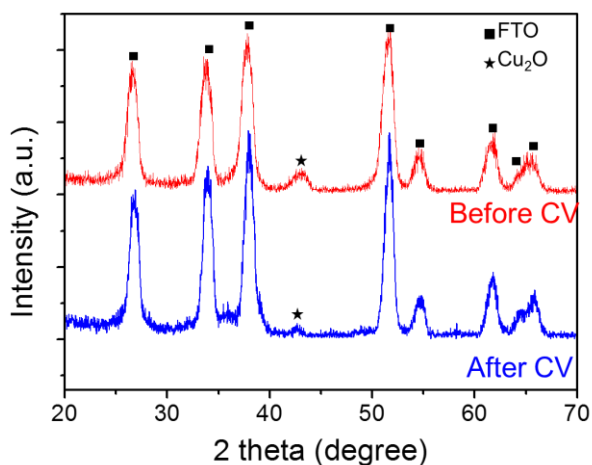


Figure 5.5 GIXRD pattern of Cu_2O electrode with 5 nm TiO_2 passivation layer before and after bulk electrolysis at 0.4 V vs. RHE.

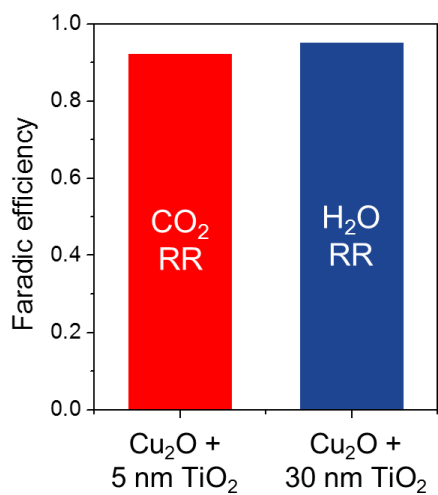


Figure 5.6 Faradic efficiency for the 5-nm TiO_2 coating and 30-nm TiO_2 coating on Cu_2O nanofiber.

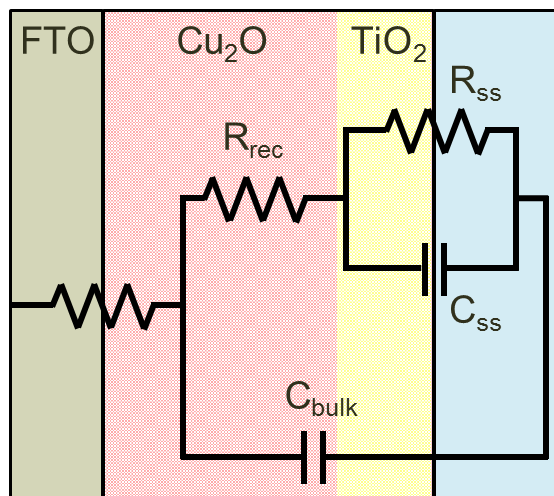


Figure 5.7 Equivalent circuit model for the photocathode.

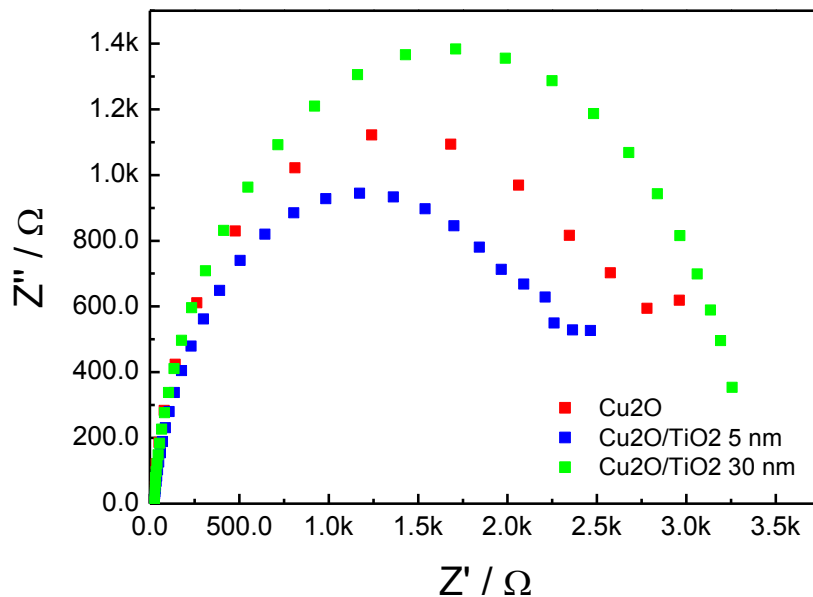


Figure 5.8 Nyquist plot for bare Cu_2O nanofiber, Cu_2O nanofiber with 5 nm TiO_2 overlayer, and Cu_2O nanofiber with 30 nm TiO_2 overlayer.

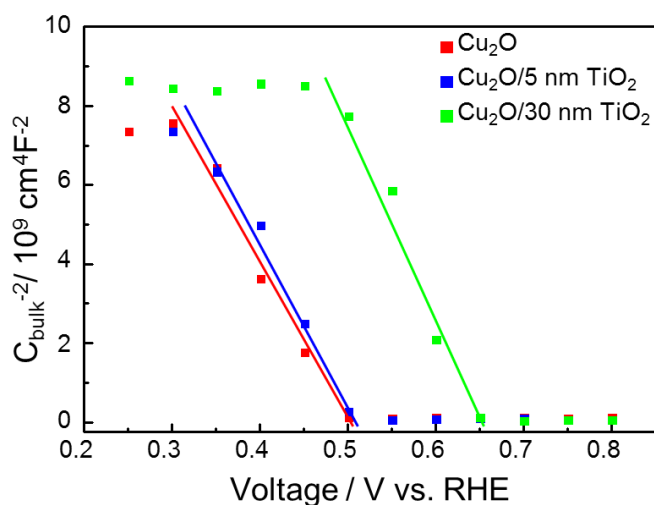


Figure 5.9 Mott-Schottky plot for the $\text{Cu}_2\text{O}/\text{TiO}_2$ system with different thickness of the TiO_2 passivation layer.

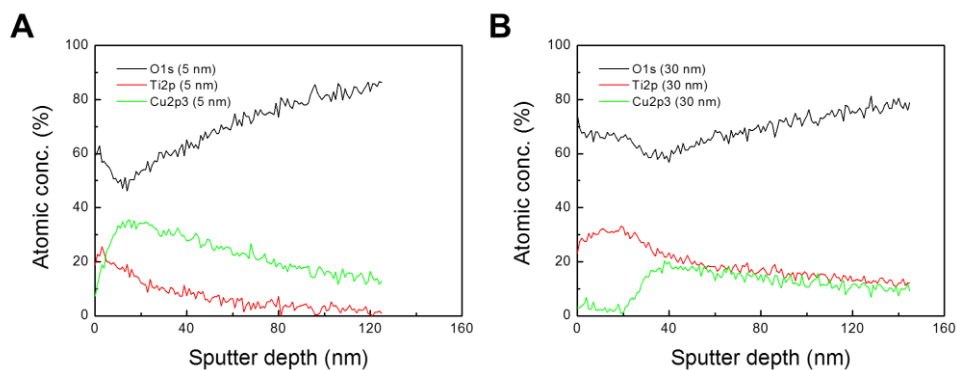


Figure 5.10 X-ray photoelectron spectroscopy (XPS) depth profile of $\text{TiO}_2/\text{Cu}_2\text{O}$ electrode after post-annealing according to the thickness of TiO_2 ; 5 nm, and 30 nm.

5.2.3. Effect of the phase of copper oxide

To observe the effect of the phase control of copper oxides, the photocurrent density was measured with varying phases of copper oxides. As shown previously in Figure 1, the annealing of nanofibers at atmospheric pressure, 50 μ Torr, and 10 μ Torr induced the mono-phase CuO (CuO), mixture of CuO and Cu₂O (CuO/Cu₂O), and mono-phase Cu₂O (Cu₂O), respectively with the fixed annealing time of 3 h and a temperature of 500 °C. The fraction of phases of the copper oxide differs according to the pO_2 , however, the photocurrent density shows no significant differences because both the CuO and Cu₂O are photoactive even though the reactions are quite different (Figure 5.11). They showed a photocurrent density of nearly 1 mA/cm² at 0.4 V vs. RHE, while the mixture of metallic Cu and Cu₂O fabricated by annealing at 1 μ Torr showed low photocurrent density because metallic Cu is not photoactive and interferes light absorption of Cu₂O (Figure 5.12).

The photocurrent density at 0.4 V vs. RHE is relatively high compared to the previously reported Cu₂O electrodes as can be seen in Figure 5.13, moreover, if this photocurrent originates from the CO₂ reduction in the aqueous electrolyte, this value is more meaningful since the photoactivity for the CO₂ reduction in an aqueous electrolyte was small. The products for the photoelectrochemical CO₂ reduction were analyzed by gas chromatography (GC) and nuclear magnetic resonance spectroscopy (NMR) (Figure 5.14, 5.15). No gaseous products were observed on the gas chromatography, except CO₂ and oxygen, indicating that CO₂ is converted into liquid products, and NMR spectroscopy was conducted to analyze the liquid products.

Next, the effects of the fraction of CuO and Cu₂O on the faradic efficiency for the CO₂ reduction and water reduction were analyzed (Figure 5.16). It is known that Cu₂O has a

more negative conduction band edge position than that of CuO, which means that photogenerated electrons from Cu₂O have higher potential than that from CuO. It is confirmed by the flat band potential of CuO of 0.624 V vs. RHE, which is more positive than that of Cu₂O (Figure 5.17).

In the case of mono-phase CuO, CO₂ reduction did not occur, and only water reduction occurred. In the case of the CuO/Cu₂O sample, the electrode consisting of CuO and Cu₂O, with the fraction of Cu₂O to whole copper oxide of 0.46, showed 18% faradic efficiency for the CO₂ reduction and 73% for the water reduction. Although the fraction of Cu₂O is nearly half of the total copper oxides, the faradic efficiency for the CO₂ reduction was not as high. Because a water reduction has a lower activation energy barrier than that of a CO₂ reduction, a H₂ evolution is more favored than a CO₂ reduction if both reactions are possible in the electrode. Another reason is that since the band gap of CuO is much smaller than that of Cu₂O, CuO absorbs a larger portion of the sunlight spectrum, thereby making the water reduction more dominant than the CO₂ reduction. In the case of the Cu₂O sample, the electrodes all consists of the Cu₂O phase and produce high energy electrons that overcome the activation energy of the CO₂ reduction. As a result, only the CO₂ reduction occurred with the faradic efficiency of 93%, which is the highest performance in the aqueous electrolyte to the best of our knowledge, emphasizing the importance of producing a mono-phase Cu₂O.

The detailed products for the CO₂ reduction by mono-phase Cu₂O according to the applied potentials between 0.4 V and 0.8 V vs. RHE are analyzed in Figure 5.18. The major products were formic acid, ethanol, and methanol. At low bias of 0.8 V and 0.7 V vs. RHE, the major product was formic acid, while ethanol and methanol were not produced. The production of formic acid decreased from 0.6 V vs. RHE, and the production of ethanol increased slightly. After the bias of 0.6 V vs. RHE, the major

product was methanol, and at 0.4 V vs. RHE, methanol was produced with a selectivity of 87%, and ethanol was produced with a selectivity of 5.8%. This high selectivity for alcohol in the aqueous condition was possible because the electrons with high electron potential are successfully supplied at the interface with the electrolyte by precise phase control of the mono-phase Cu_2O without CuO , which decreases the CO_2 selectivity.

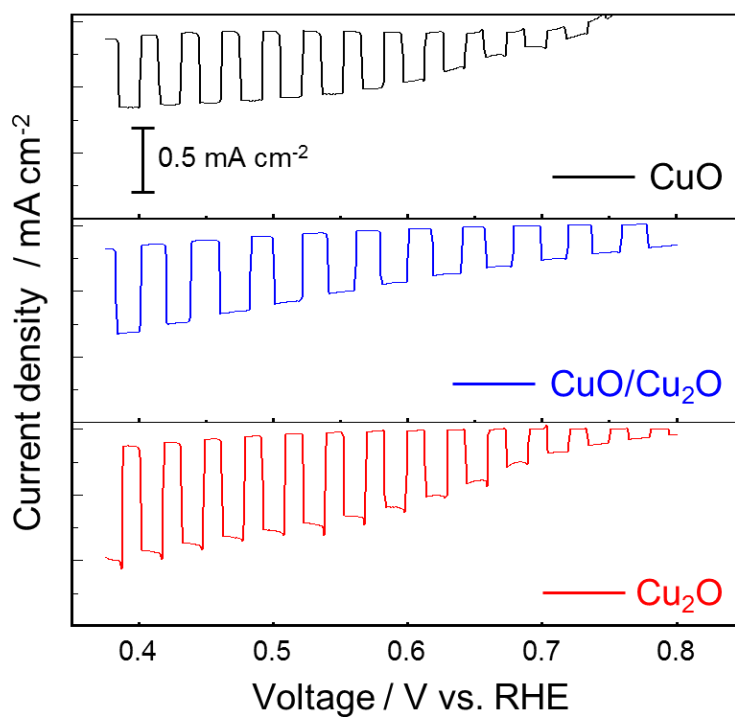


Figure 5.11 Photoelectrochemical performances for the Cu_2O photocathode: photocurrent density curve according to the phase of copper oxides.

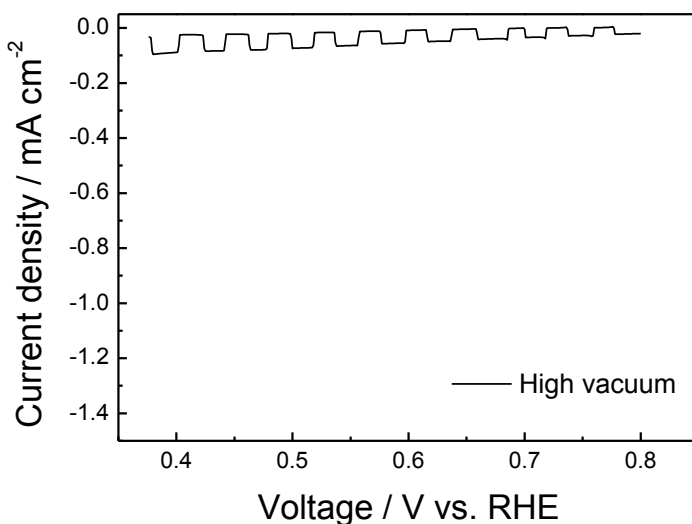


Figure 5.12 Photocurrent density curve of CuO annealed at high vacuum, showing low photoactivity due to the interfering of light absorption by Cu.

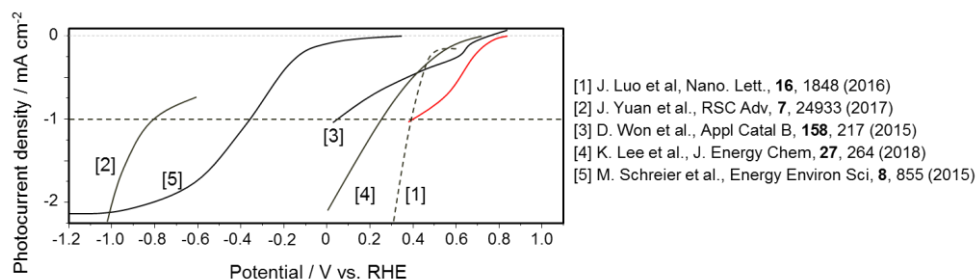


Figure 5.13 Plots of the photocurrent density for previously reported data of CO_2 reduction and H_2 evolution by Cu_2O photoelectrode. Black solid line indicates CO_2 reduction, black dotted line indicates H_2 evolution, and red solid line indicates CO_2 reduction by this paper.

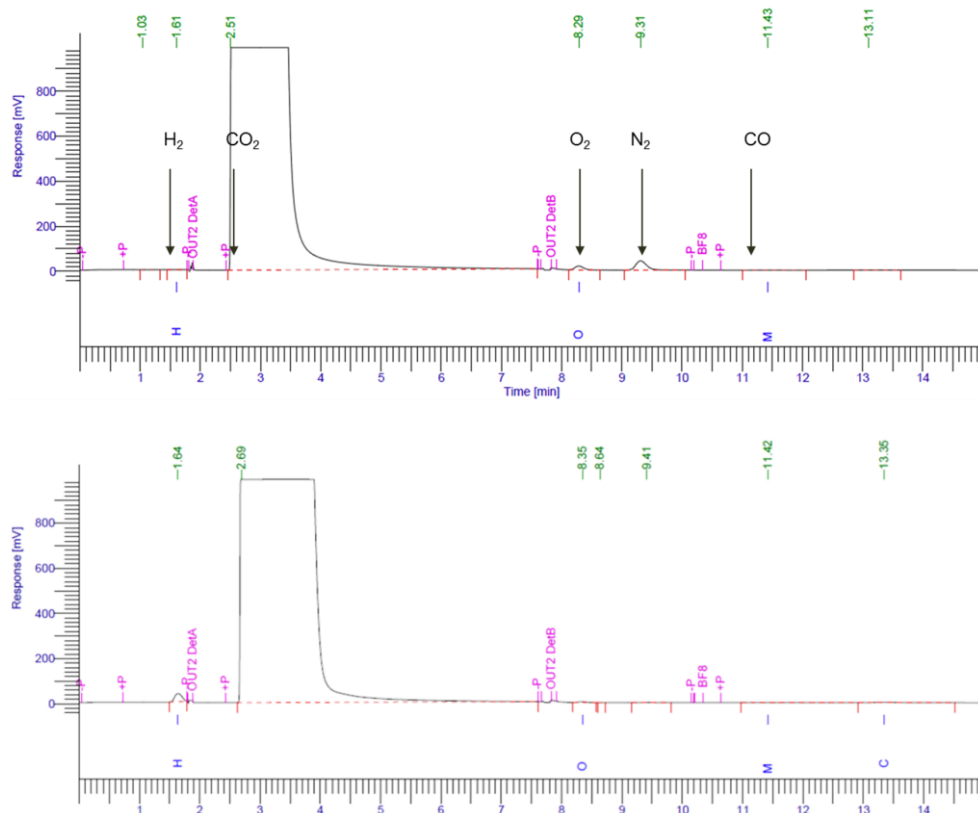


Figure 5.14 Gas Chromatography (GC) spectra after bulk electrolysis by mono-phase Cu_2O electrode.

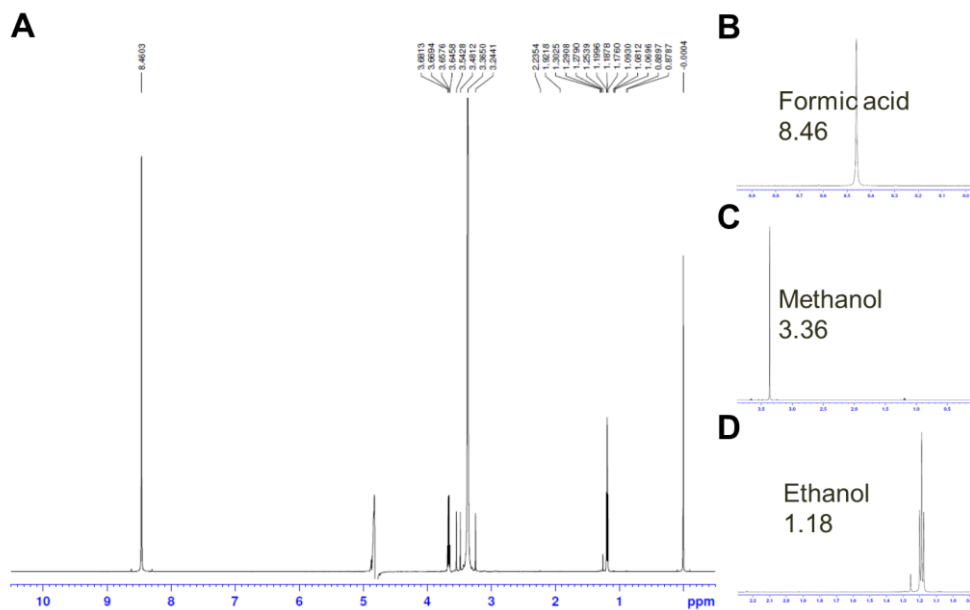


Figure 5.15 Nuclear Magnetron Resonance (NMR) spectra after bulk electrolysis by mono-phase Cu_2O electrode.

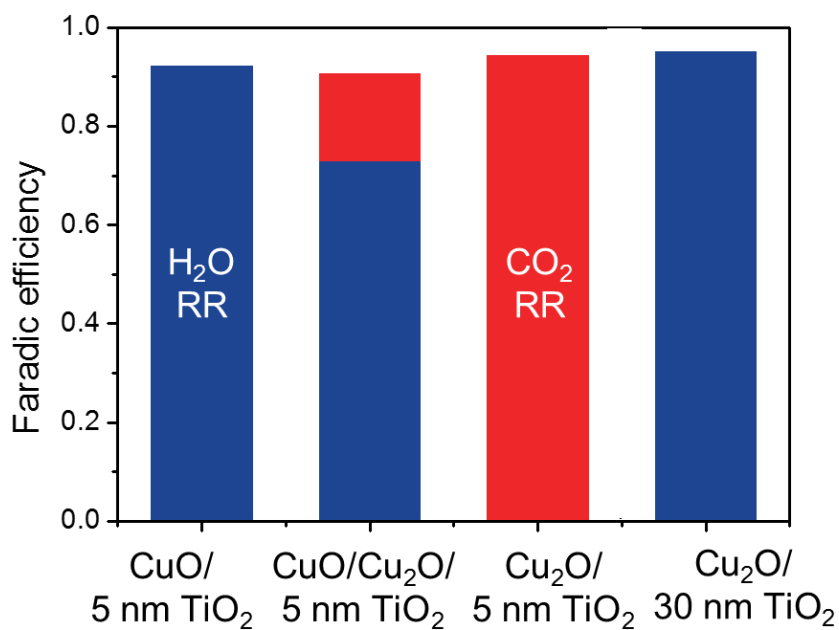


Figure 5.16 Faradic efficiency for the CO_2 reduction and the water reduction after bulk electrolysis at 0.4 V vs. RHE with the $\text{Cu}_2\text{O}/\text{TiO}_2$ system with TiO_2 thicknesses of 5 nm and 30 nm, and according to the phase of the copper oxides.

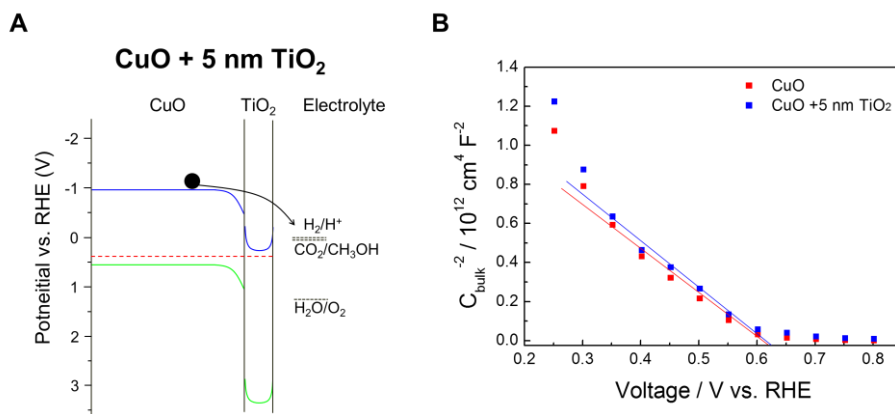


Figure 5.17 (A) Band diagram of CuO with 5 nm TiO₂ overlayer. (B) Mott-schottky plot for bare CuO nanofiber and CuO with 5 nm TiO₂ overlayer.

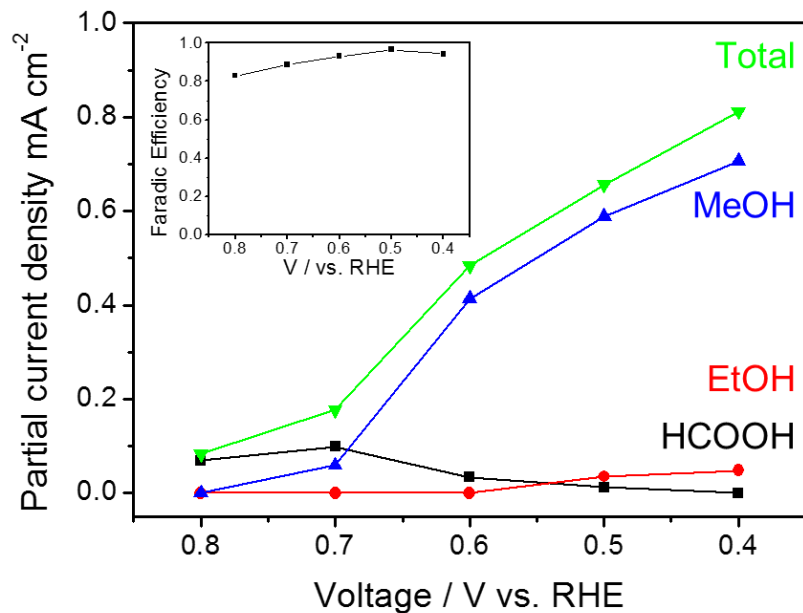


Figure 5.18 Partial current density for the major products of the CO_2 reduction by the mono-phase Cu_2O electrode. Inset is the faradic efficiency according to the applied bias.

5.3 Summary

The mono-phase Cu₂O nanofiber is fabricated by predictive synthesis based on thermodynamic and kinetic considerations. The hierarchical structure that consists of Cu₂O thin film underlayer, and TiO₂ passivation layer is developed to adopt Cu₂O nanofiber to the photocathode for CO₂ reduction. Thus, CO₂ is converted to methanol with selectivity over 90% in an aqueous electrolyte by precisely controlling the phase of copper oxide and the rational design of the nanostructure.

The Cu₂O thin film underlayer is essential for optimizing the photoactivity of nanostructured Cu₂O electrode. Without the underlayer, nanofiber electrode demonstrated very low photoactivity, however, after the adoption of underlayer, the photocurrent density is dramatically improved. The Cu₂O thin film underlayer effectively blocked the electron leakage from the FTO substrate which degrades photoactivity by shunting the device.

The TiO₂ overlayer is essential for the stability of Cu₂O electrode. Without the TiO₂ passivation, the photocurrent is degraded to nearly zero within a few seconds. The 5 nm thickness of TiO₂ passivation layer is deposited by ALD process. Cu₂O nanofiber electrode with as-deposited TiO₂ layer showed negligible photocurrent due to the surface defects in amorphous layer. After post-annealing of the electrode, it showed photocurrent density with improved stability.

The phase of copper oxide was crucial for the selectivity of CO₂ reduction. If the CuO phase is present in the Cu₂O, the selectivity for CO₂ is significantly degraded and hydrogen evolution reaction is favoured. In mono-phase Cu₂O, the major product was methanol which can be directly used as a chemical fuel in industrial process.

CHAPTER 6

Generation of Oxygen Vacancies in Fe₂O₃ Photoanode

(This chapter self-cites reference [6.1])

6.1. Introduction

The improvement of the electrical conductivity of hematite (α -Fe₂O₃) is one of the most important challenges in the development of high performance photoanodes for water oxidation. Because of the low electrical conductivity in pure hematite, the photoactivity is limited by the inefficient electron transport to the current collector and by the short diffusion length of holes around the electrolyte interface. To date, the conventional approach to overcome these drawbacks has been either to identify heterogeneous dopants or to fabricate nanostructured electrodes. Here, we investigate the role of the intrinsic dopant–oxygen vacancy and the interplay between the oxygen vacancy and an extrinsic dopant, such as tin (Sn). No previous reports have considered both intrinsic and extrinsic defects in the context of photoactivity. Based on this understanding, we demonstrate a significant enhancement of hematite photoactivity by identifying the intrinsic and extrinsic doping concentrations for maximal synergy. We found that the enhancement effect of intrinsic doping could be comparable or slightly better than that of extrinsic Sn-doping. This study emphasizes the importance of oxygen

vacancies as well as the context of multiple defects in the design of metal-oxide-based photoanodes.

Hematite can absorb sun light with wavelengths shorter than 560 nm. In addition, the valence-band position is lower than the redox potential for water oxidation (H_2O/O_2), which allows for the oxidation of water under visible light. Moreover, the natural abundance of iron, the environmentally benign synthesis process for hematite, and the good electrochemical stability in an aqueous environment make this material attractive and promising for implementation in a photoelectrochemical cell (PEC). However, the short diffusion length of holes [6.2, 3], the poor kinetics for water oxidation [6.4], a large requisite overpotential [6.5], and poor electrical conductivity [6.6, 7] limit the use of hematite as a practical photoanode. The low conductivity of polycrystalline hematite (ca. $10^{14} \Omega \cdot cm$) [6.8] is attributed to polaron hopping conduction through a Fe^{3+}/Fe^{2+} valence exchange mechanism involved in lattice distortion [6.9], which limits the photocurrent in hematite.

To improve the conductivity of hematite, researchers have primarily focused on extrinsic doping with, for example, Ti [6.10, 11], Sn [6.11, 12], Zr [6.13], Nb [6.7, 14], and Si [6.10, 15, and 16] as electron donors and Cu [6.17] and Mg [6.18, 19] as electron acceptors. Donor ions introduce electrons into neighboring Fe^{3+} sites and reduce Fe^{3+} to Fe^{2+} [6.20]. Because the conduction of hematite is due to the polaron hopping, the Fe^{2+} sites can improve the electrical conductivity. Indeed, Si-doped nanostructured hematite [6.21, 22] and Sn-doped hematite nanocorals [6.12] showed a remarkable improvement in the photocurrent density. In addition to the cation doping, previous studies from bulk hematite crystals show that oxygen vacancies can also act as donors to improve the conductivity [6.23-26]. Recently, Y. Ling et al. reported that oxygen-deficient annealing during the thermal decomposition of β - $FeOOH$ into Fe_2O_3 could improve the

photocurrent of hematite [6.27]. Previous studies have clearly suggested that the selection of dopants and the optimization of their concentrations are important. However, fundamental questions arise as how the effect of intrinsic and extrinsic dopants can be decoupled and how the synergistic interplay between them can be maximized. We firstly investigated the close relationship between PEC performance and electrical conductivity, based on the defect chemistry including Sn dopant and oxygen vacancy. In an effort to address this challenge, we developed a general platform that allows for the systematic control of intrinsic and extrinsic dopants.

6.2. Characterization of spray-coated Fe_2O_3 films

6.2.1. Microstructure of Fe_2O_3 films

The quantitative incorporation of extrinsic dopants was achieved through control of the ratio of each precursor during aerosol spray pyrolysis (ASP, Figure 6.1). To minimize the contamination from precursors such as carbon, chlorine-based precursors were adopted because inert chlorine gas can form immediately after decomposition and can be easily removed. In this study, Sn was chosen as an extrinsic dopant, and tin chloride ($SnCl_4$) precursor was quantitatively added to a ferric chloride ($FeCl_3$) precursor solution.

Oxygen vacancies, as the intrinsic dopant, were controlled through a two-step heating process composed of thermal reduction and subsequent oxidation. During thermal reduction under high vacuum ($\sim 10^{-6}$ Torr), an iron oxide film was first completely converted into magnetite (Fe_3O_4). Then, oxidative annealing under a controlled oxygen partial pressure (pO_2) resulted in the transformation of magnetite into oxygen-deficient hematite (Fe_2O_{3-x}). The oxygen partial pressure during this step determined the concentration of oxygen vacancies. This developed method enables precise control of the oxygen vacancies in hematite, irrespective of the initial oxidation quality and status.

The doping concentration in Sn-doped hematite was controlled by changing the ratio of $SnCl_4$ to $FeCl_3$ in the precursor solution. After the spraying, a hematite film uniformly formed on the crystal grain of FTO with a thickness of approximately 100 nm. SEM analyses revealed that the observed morphology is consistent with a Stranski-Krastanov growth (layer-plus-island growth, Figure 6.2). Hematite sheets were grown parallel and vertical to the surface of uniformly coated hematite films on the FTO surface. In thicker

films, which were formed by spraying precursor solutions of 60 mL or 90 mL, the grown nano-sheets completely covered the surface (Figure 6.2C-D).

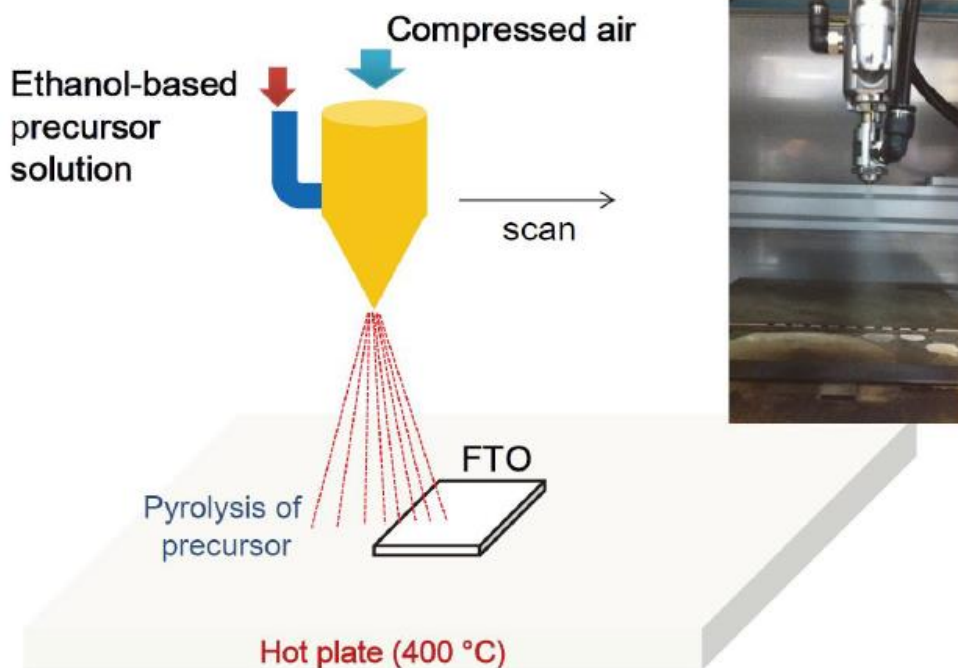


Figure 6.1 The aerosol spray pyrolysis method for the preparation of hematite films.

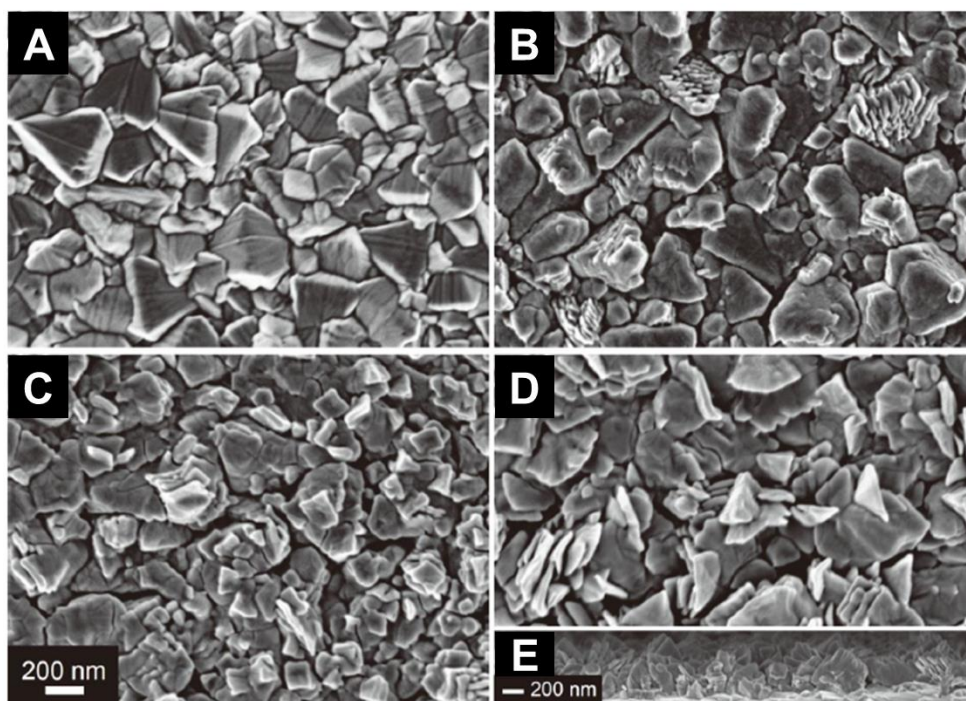


Figure 6.2 SEM images of (A) the FTO substrate and the hematite films formed by the spraying of an $FeCl_3$ solution with a volume of (B) 30 ml, (C) 60 ml, and (D) 90 ml. (E) Cross-sectional SEM of hematite films formed by the spraying of the 90ml-solution.

6.2.2. Phase of Fe₂O₃ films during annealing

The deposited hematite was reduced to magnetite through annealing at 550 °C for 1 h under high vacuum (HV annealing). After the reduction step, the color of the samples changed from red to black. X-ray diffraction (XRD) analysis confirmed that this black-colored film is magnetite (JCPDS 19-0629) (black line in Figure 6.3). The hematite films prepared from ferric nitrate (Fe(NO₃)₃) and ferric acetylacetonate (Fe(acac)₃) can also be reduced to magnetite (Figure 6.4), which indicates that chlorine does not act as a reductant. In the next step, the sample was re-oxidized to hematite through an annealing at 550 °C for 2 h under various *p*O₂. The XRD spectra in Figure 6.3 confirmed that all of the re-oxidized films in various *p*O₂ are completely transformed to hematite. For comparison purposes, a sample normally annealed at 550 °C for 3 h in ambient air without thermal reduction was also prepared.

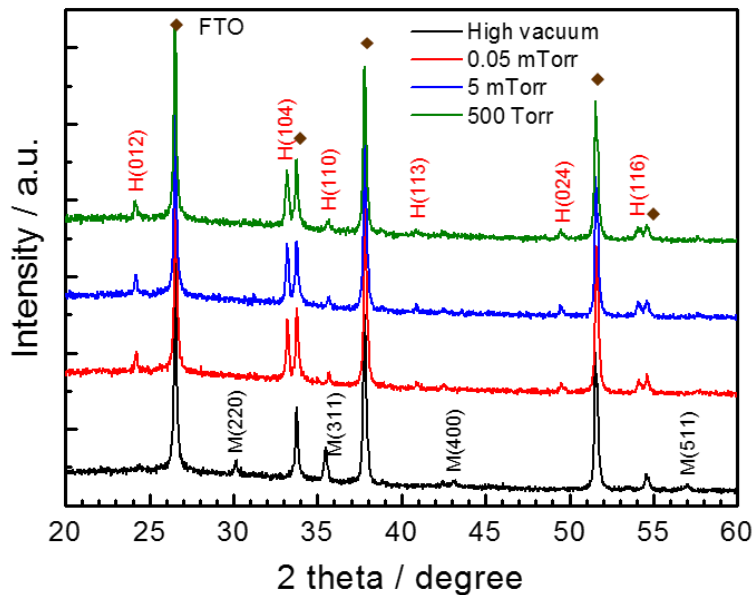
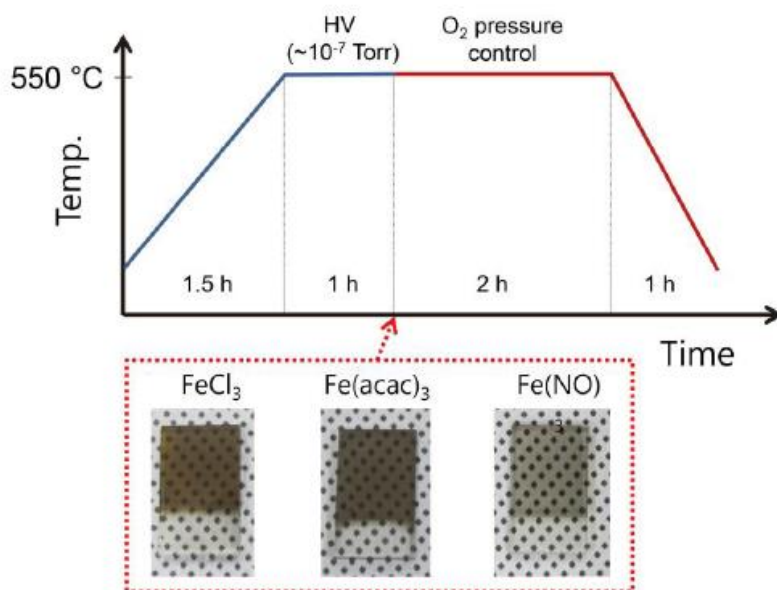


Figure 6.3 X-ray diffraction (XRD) spectra of hematite films after thermal reduction and oxidative annealing under various oxygen partial pressure.

Oxygen-partial-pressure-controlled annealing process



Normal annealing process

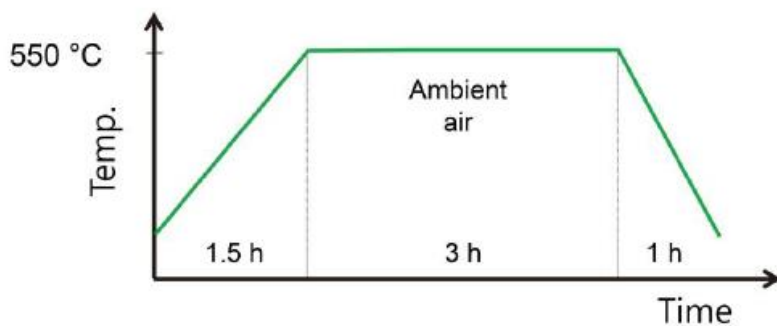


Figure 6.4 Annealing process and ambients for pO₂-controlled annealing and for normal annealing. Photographs for reduced magnetite films prepared from the different precursors and after vacuum annealing: FeCl₃, Fe(acac)₃, and Fe(NO₃)₃

6.3. Effect of oxygen vacancy generation on photoactivity

6.3.1. Generation of oxygen vacancy

In Figure 6.5, XPS analysis showed that the pO_2 during the annealing can control the amount of oxygen vacancies in hematite. By analyzing the XPS spectra, the existence and relative amount of Fe^{2+} could be monitored. Because the formation of oxygen vacancies introduces electrons into neighboring Fe^{3+} sites and reduces Fe^{3+} to Fe^{2+} , the quantity of Fe^{2+} sites corresponds to that of oxygen vacancies. The $Fe2p_{2/3}$ and $Fe2p_{1/2}$ peaks for Fe_2O_3/Fe_3O_4 were detected at a binding energy of approximately 710.5 eV, and 724 eV, respectively. It also confirmed that the phase of samples is Fe_2O_3 or Fe_3O_4 as observed in XRD analysis. A notable point is the difference in the intensity of peaks at the binding energy of 715.7 eV, which is a binding energy for a Fe^{2+} satellite in Fe_2O_3/Fe_3O_4 . The sample annealed at high vacuum clearly exhibited the peak corresponding to Fe^{2+} at 715.7 eV as shown in the black curve in Figure 6.5A. In contrary, the sample annealed at ambient air ($pO_2 = 150$ Torr) showed no peak from Fe^{2+} sites (blue line). As shown in Figure 6.5A, the peak intensity for Fe^{2+} satellite decreased with increasing oxygen partial pressure during oxidative annealing.

For a quantitative comparison, the peak area for the Fe^{2+} satellite was calculated from the XPS spectra (Figure 6.5B). The peak area was calculated through the integration from the baseline that was set as a straight line from 714.1 eV to 718 eV. The peak area for Fe^{2+} satellite decreased as the pO_2 was increased, which indicated an increase in the concentration of oxygen vacancies. Therefore, these results indicate that oxygen vacancy concentration can be controlled by controlling the oxygen partial pressure during the thermal annealing.

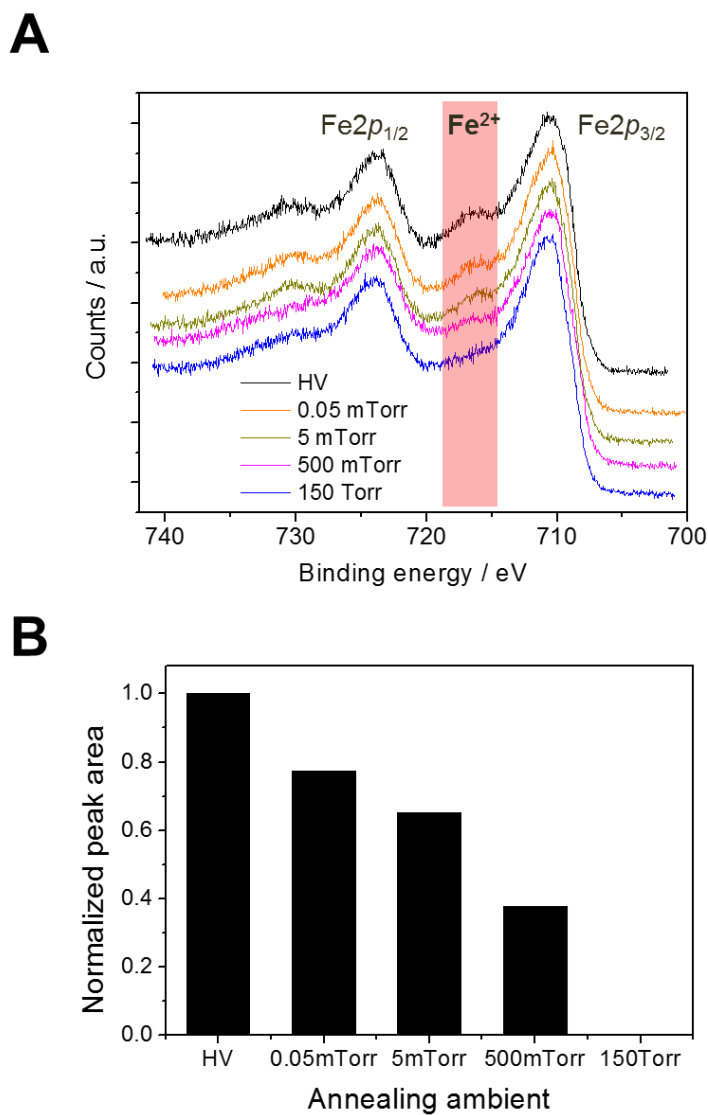


Figure 6.5 (A) XPS spectra of hematite films after thermal reduction and oxidative annealing under various pO_2 . (B) The area values for the Fe^{2+} satellite peak (715.7 eV) are normalized to the value for the reduced film under high vacuum..

6.3.2. Interplay with the external dopant

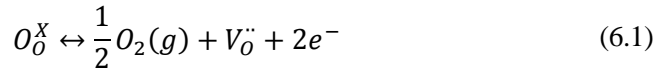
It is generally accepted that intrinsic defects in oxygen deficient ferric oxides are also donor centers, thereby enhancing the conductivity of hematite, which was observed in thermally reduced hematite [6.23-25]. In addition, when hematite is doped by aliovalent cations, the charge of dopants must be compensated for by the opposite charge in a lattice defect or by an electronic defect to preserve charge neutrality. Sn^{4+} ions in hematite introduce electrons into nearest Fe^{3+} sites and reduce Fe^{3+} to Fe^{2+} . Because the conduction of hematite is due to the polaron hopping, the Fe^{2+} sites can improve the electrical conductivity.

To confirm the effect of oxygen vacancies and Sn doping on the electrical property of hematite, we measured the changes in electrical conductance of hematite films on the quartz substrate in the variation of pO_2 and Sn-dopant concentration using I-V sweep. The dependence of the electrical conductance on pO_2 and Sn concentration is presented in Figure 6.6A. The conductance of hematite depended on both the pO_2 and the Sn concentration.

In the conductance of Sn-doped hematite, there is a maximum conductance at a certain concentration. Upon increasing the Sn concentration, the electrical conductance dramatically increased up to 1 at.%-Sn, but that decreased at the high concentration (10 at.%). In addition, the lower pO_2 during the oxidative annealing resulted in the higher electrical conductance. The maximum conductance was measured from the Sn-doped hematite annealed at 5×10^{-5} Torr- pO_2 .

The electrical conductivity of Sn-doped hematite is determined by the carrier concentration, based on the assumption that mobility is not a function of the doping conditions. Therefore, the interplay between the extrinsic dopant, Sn, and the intrinsic

dopant, $V_O^{\bullet\bullet}$, can be explained by the change in the carrier concentration (Figure 6.6B). The electron concentration (n) in pure hematite without Sn is determined by the concentration of oxygen vacancies. An increase in oxygen vacancies usually contributes to the carrier density, which is described below:



In the intrinsic region at low pO_2 , the oxygen vacancy concentration ($[V_O^{\bullet\bullet}]$) dominates in the electroneutrality condition, and then $n = 2[V_O^{\bullet\bullet}]$. It is a possible mechanism that interstitial Fe ions exist instead of oxygen vacancy in oxygen deficient hematite. It is experimentally difficult to determine whether the existing defects are oxygen vacancies or Fe interstitials. However, the same principles to explain the role as an electron donor can be applied to both cases. In Sn doped hematite, electron concentration is the sum of oxygen vacancies and the Sn concentration under low pO_2 , whereas that under high oxygen pressure is only the Sn concentration. When Sn^{4+} ions are introduced into the hematite lattice, the extra positive charge at the substitutional Sn ions (Sn_{Fe}^{\bullet}) can be compensated by a reducing cation (Fe_{Fe}' or Fe^{2+}) or by a cation/anion vacancy (V_{Fe}''' or $V_O^{\bullet\bullet}$) to preserve charge neutrality [6.28], and the expression for charge neutrality is:

$$n + 3[V_{Fe}'''] + [Fe_{Fe}'] = p + [Sn_{Fe}^{\bullet}] + 2[V_O^{\bullet\bullet}] \quad (6.2)$$

The electroneutrality condition for Sn-doped hematite annealed under controlled pO_2 is represented by $n = [Sn_{Fe}^{\bullet}] + 2[V_O^{\bullet\bullet}]$ because sufficient oxygen vacancies are formed

to affect the electron concentration. However, in the normally annealed Sn-doped hematite, the electrical conductivity of the hematite is determined by C_{Sn} ($n = [\text{Sn}'_{\text{Fe}}]$) because of the low oxygen vacancy concentration.

As the Sn doping concentration is increased, the conductivity reaches its maximum and starts to decrease with increasing C_{Sn} . At a high doping level (above the solubility of Sn), the nonionized Sn atoms, i.e., the neutral defects, such as $(\text{Sn}_2\text{O}_4'')$ or $(\text{Sn}_2\text{O}_4)^x$, act as scattering centers, which decrease the conductivity. The solubility of SnO₂ in bulk hematite is less than 1 mol% below 1073 K [6.29].

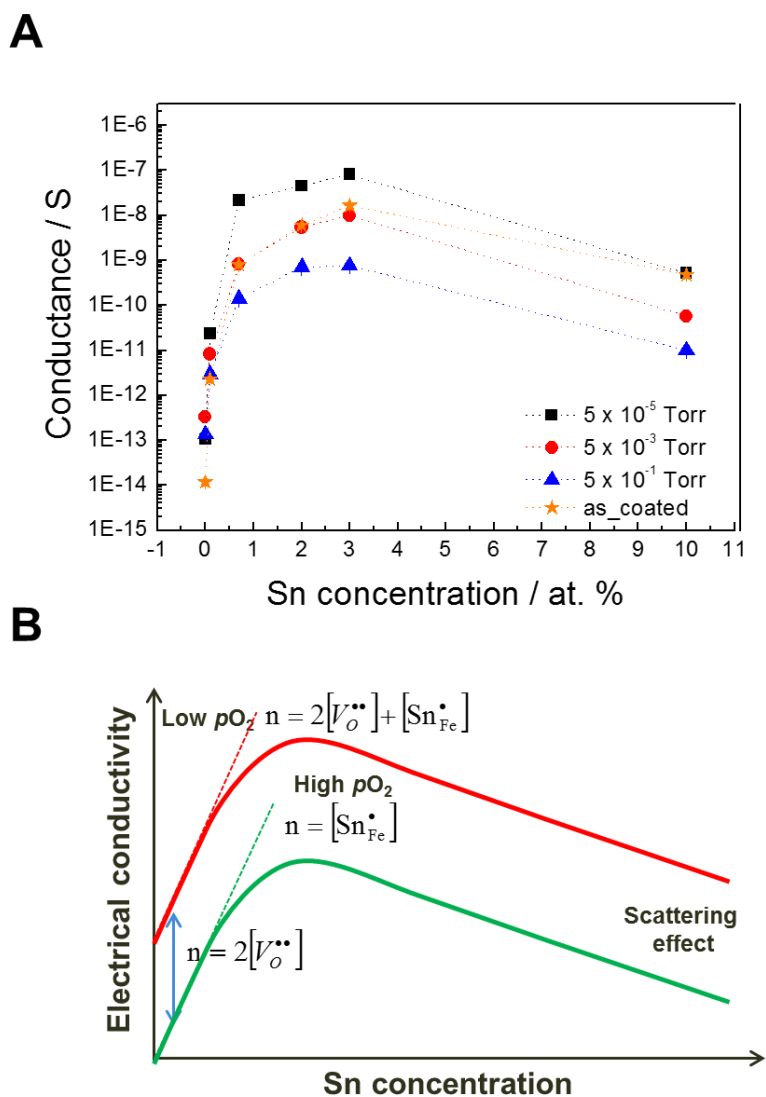


Figure 6.6 (A) Electrical conductance of post-annealed hematite films on quartz substrate with various Sn-concentration. (B) Schematic diagram that demonstrates the effects of doping and of pO_2 on the electrical conductivity of post-annealed hematite films.

6.3.3. Effect on photoelectrochemical performance

To investigate how the concentrations of oxygen vacancies affect the PEC performance of the hematite films, the anodic photocurrent was measured under standard global solar illumination (AM 1.5G, 100 mW cm^{-2}) in 1 M NaOH (pH 13.6) electrolyte. In Figure 6.7A, the hematite that was normally annealed under ambient air showed poor photoactivity. The photocurrent magnitude was limited to 0.1 mA cm^{-2} at 1.6 V with respect to reversible hydrogen electrode (RHE). Because pure polycrystalline hematite exhibits a low electrical conductivity, this poor photoactivity is reasonable for the hematite film without any dopant or residue from the precursor solution. However, as can be seen in Figure 6.7B, in the annealed hematite at 150 Torr (ambient air) after thermal reduction, the magnitude of the photocurrent density increased, and onset voltage of photocurrent was negatively shifted. The photocurrent in the hematite annealed under a pO_2 of 5×10^{-3} Torr increased to 1.14 mA cm^{-2} at 1.6 V vs. RHE. To confirm the effect of the pO_2 used during the annealing on the photoactivity, we compared the maximum anodic shown in the Figure 6.9B, the photocurrent density increased with decreasing pO_2 during the annealing process. The dependence of the photocurrent magnitude on the pO_2 coincides with the dependence of the electrical conductance and the concentration of Fe^{2+} sites determined from the XPS analysis.

The ability to control the concentration of oxygen vacancies can be further applied to boost the effects of extrinsic dopants. The same annealing process involved with reduction and oxidation was performed. The out-diffusion of Sn from FTO is negligible because Sn was not detected from XPS analysis after the annealing (Figure 6.8). One of the most interesting features is that the enhancement effect is strongly dependent on the Sn doping concentration and on the oxygen vacancy level. As shown in Figure 6.9A, the

photocurrent density of pO_2 -controlled hematite doped with 1.0 at.% Sn (solid green line) is higher than that of normally annealed hematite with 1.0 at.% Sn (dash-dotted green line). The increase ratio in the photocurrent was approximately 30 % at 1.23 V vs. RHE. The hematite doped with 0.1, 0.7, 1.0 at.%-Sn showed enhanced photocurrent density compared to that of undoped hematite (Figure 6.9B). The maximum photocurrent was observed in 0.7 at.% Sn-doped hematite (1.20 mA cm^{-2} at 1.6 V vs. RHE).

The influence of pO_2 on the photoactivity in Sn-doped hematite was extensively investigated through a comparison of the magnitude of the photocurrent density at 1.6 V vs. RHE (Figure 6.10). The J - V curves collected in all observed conditions for oxygen partial pressure and Sn concentration are presented in Figure 6.11. As previously discussed, a lower oxygen partial pressure during the annealing resulted in a higher oxygen vacancy concentration. The enhancement effect of oxygen vacancies is significantly greater for the sample with a lower pO_2 and a lower Sn doping concentration (< 0.5 at.%). The current density difference at 0.1 at.%-Sn between the sample prepared by annealing at 5×10^{-5} Torr $-pO_2$ and that prepared by annealing at 5×10^{-1} Torr $-pO_2$ is 0.2 mA cm^{-2} (increase of ca. 20 %). The difference becomes small at 0.5 at.%-Sn. The photocurrent in the 0.1 at.%-Sn hematite annealed at 5×10^{-5} Torr was the highest value observed in this work (1.21 mA cm^{-2} at 1.6 V vs. RHE). As the Sn doping concentration is increased, the photocurrent density reaches its maximum and starts to decrease with increasing the doping concentration. There is an optimum concentration of Sn dopant for maximum photoactivity of hematite photoanode.

As measured the electrical conductivity, the maximum photocurrent density also depends on the relative ratio of oxygen vacancies and Sn. Interestingly, the dependence of the conductivity and the photocurrent was very similar. Although the Sn concentration

for the maximum electrical conductance did not entirely coincide with that for the maximum photocurrent density, the conductivity is one of the major causes to determine the photocurrent in the various pO_2 and Sn concentration. The optical property of hematite films was merely dependent on the Sn doping and ambient during the oxidative annealing (Figure 6.12).

The decrease of the photocurrent density above a certain Sn concentration is also related to the reduction of the width of space-charge layer in semiconductor as well as the decrease of the conductivity. High doping results in the decrease of the number of photogenerated holes migrated toward the hematite/liquid junction to perform the water oxidation. This effect may lead to the small difference in the dependence of the electrical conductivity and the photocurrent density on the pO_2 and the doping. For example, in the case of 5×10^{-1} Torr- pO_2 , the highest current was observed at 0.7 at.%-Sn, whereas, in the case of 5×10^{-5} Torr- pO_2 , the highest current was observed in 0.1 at.%-Sn. In the hematite annealed at low pO_2 , the additional generation of conducting carrier by Sn doping has negatively affected the photocurrent density. In addition, the current level can be further improved by other causes such as nanostructuring and/or thickness optimization. Thicker hematite films with 1 at.%-Sn showed a higher photocurrent density (Figure 6.13).

Although the highest current density among the reported data was not achieved here, Figure 6.10 clearly shows the trend of how the extrinsic and intrinsic doping together influence the PEC performance. The variation of photocurrent density in Figure 6.10 implies that the optimum concentration for extrinsic doping should be decided based on the oxygen vacancy concentration. It is necessary to consider both intrinsic and extrinsic dopants together to achieve the maximum photocurrent. We believe that this design

principle can be generalized to other oxide-based photoelectrodes and different nanostructures.

The onset voltage is also dependent on the extrinsic and intrinsic doping ratio (Figure 6.14). Here, the onset potential was defined as the voltage where the photocurrent exceeds the dark current. For each sample, dark current was measured separately for the accuracy. A more negative shift in the onset potential was observed in samples annealed under lower pO_2 , and the lowest onset potential was observed in undoped hematite annealed at 5×10^{-5} Torr- pO_2 (0.76 V vs. RHE). It is interesting that oxygen vacancies can affect the onset potential and result in the negative shift of ca. 0.1 V. However, the onset voltage increased with increasing C_{Sn} . At pO_2 greater than 5×10^{-2} Torr, the onset voltage does not depend on the pO_2 , but rather shows a more negative shift with greater Sn-doping concentration. However, above 1.0 at.%, the onset voltage increased with increasing C_{Sn} . In particular, a more positive shift as a result of the increased C_{Sn} was observed in samples annealed at lower pO_2 (Figure 6.11). The exact mechanism how the onset potential is modified depending on the doping nature is under investigation.

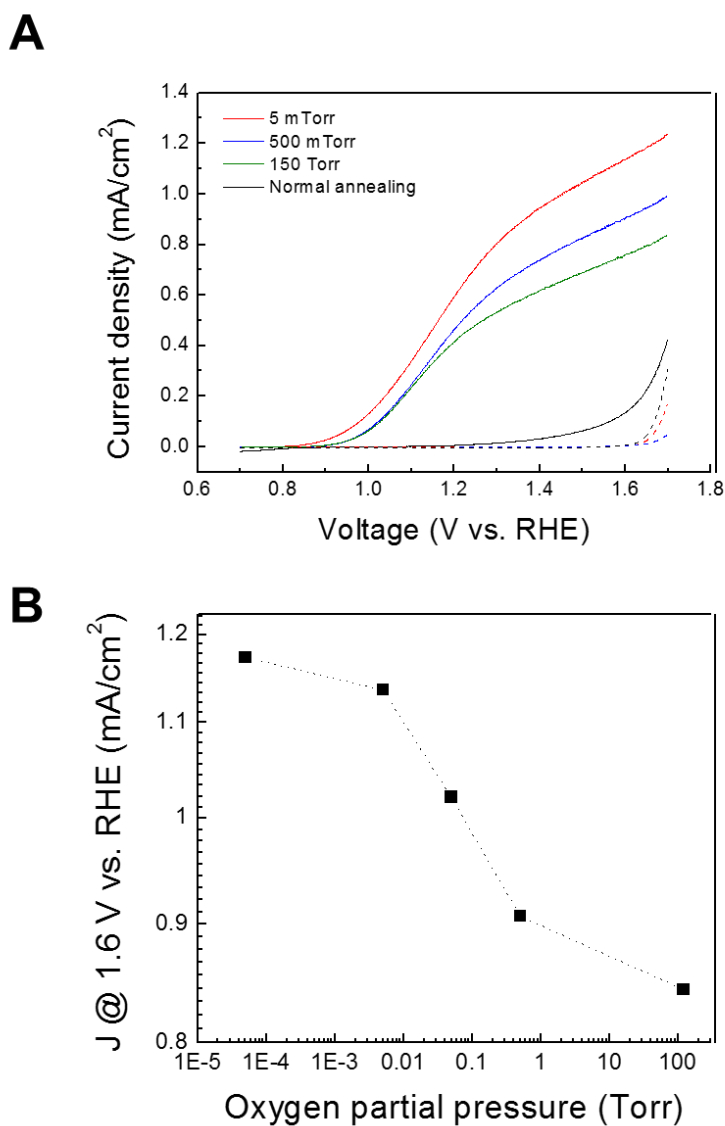


Figure 6.7 (A) Photocurrent density-voltage curves of a hematite film after pO_2 -controlled annealing under simulated solar illumination (solid line) and in the dark (dashed line), respectively. (B) Photocurrent density at 1.6 V vs. RHE for undoped hematite as a function of pO_2 .

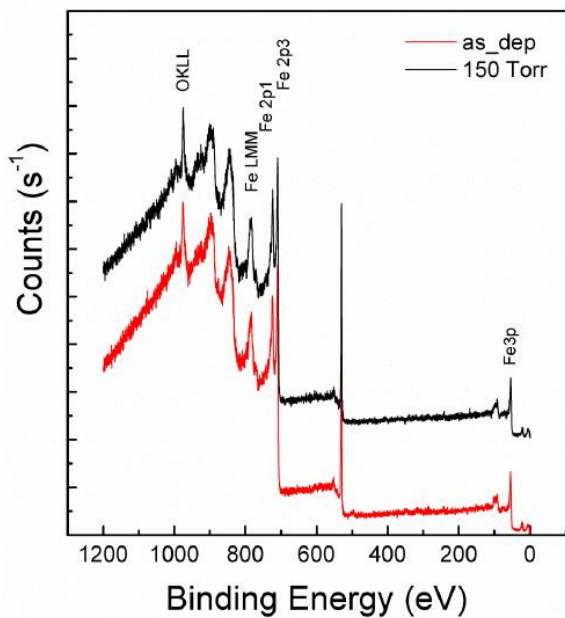


Figure 6.8 XPS spectra measured from the as-coated hematite (red) and from the hematite after thermal reduction and oxidative annealing at ambient air (black)

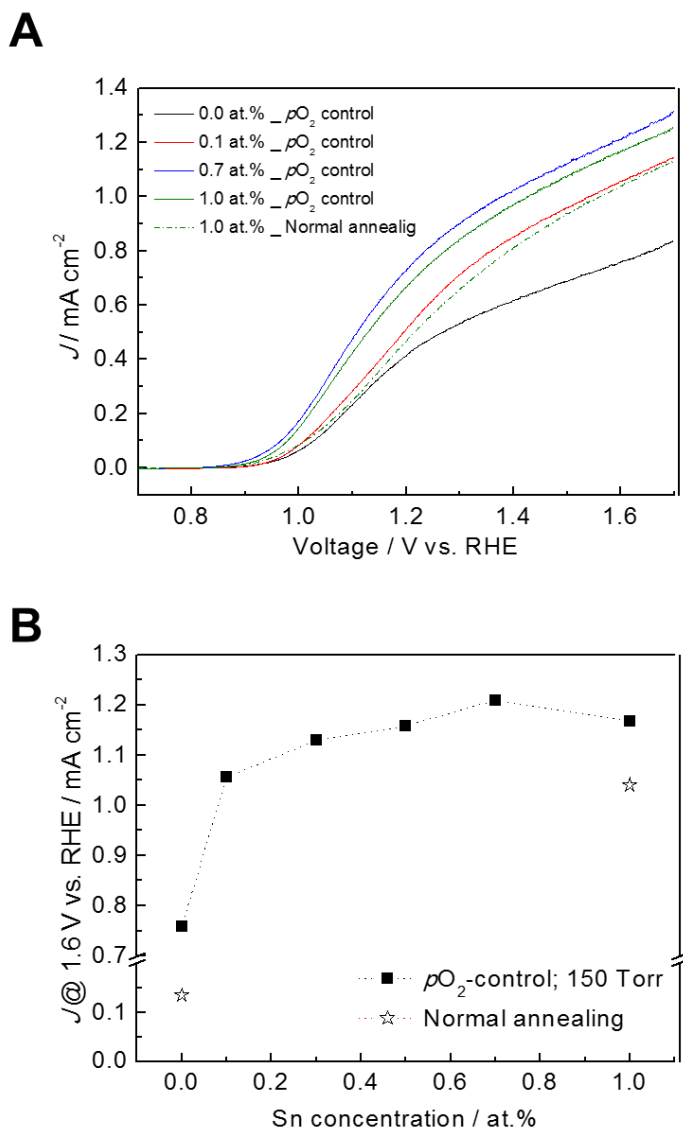


Figure 6.9 (A) Photocurrent density-voltage curves for Sn-doped hematite films and (B) photocurrent density at 1.6 V vs. RHE as a function of the doping concentration after $p\text{O}_2$ -controlled annealing in ambient air (solid line, full markers) and for after normal annealing (dash-dotted line, empty markers).

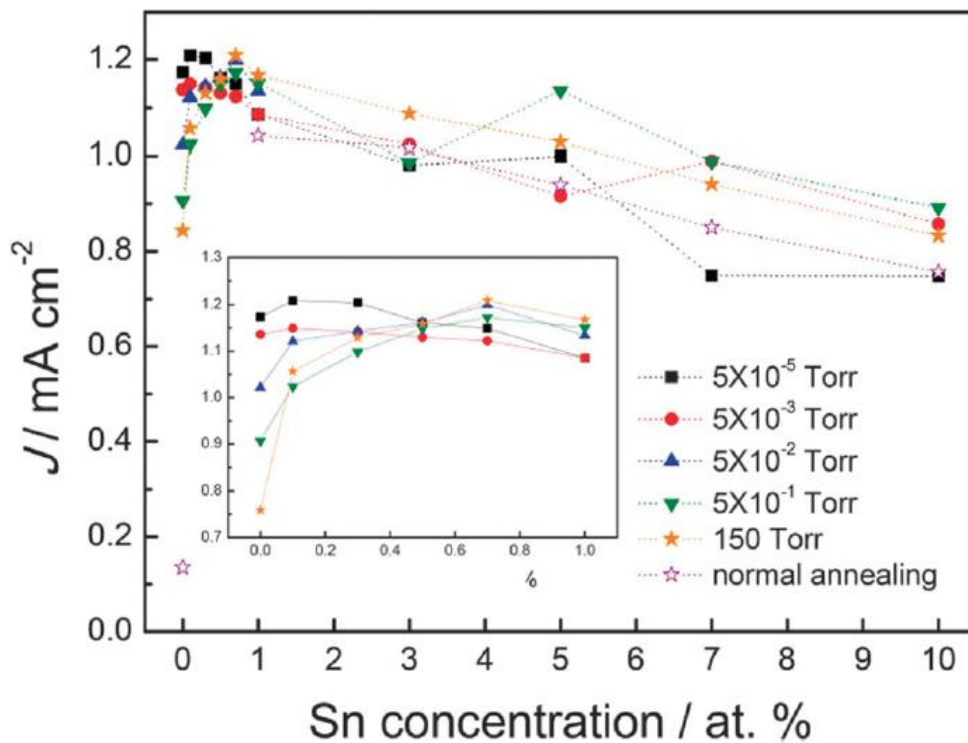


Figure 6.10 Photocurrent density at 1.6 V vs. RHE for hematite films as a function of the Sn concentration after pO_2 -controlled annealing under various pO_2 atmospheres. Inset: Enlarged graph situated between 0 ~ 1 at.% of Sn concentration.

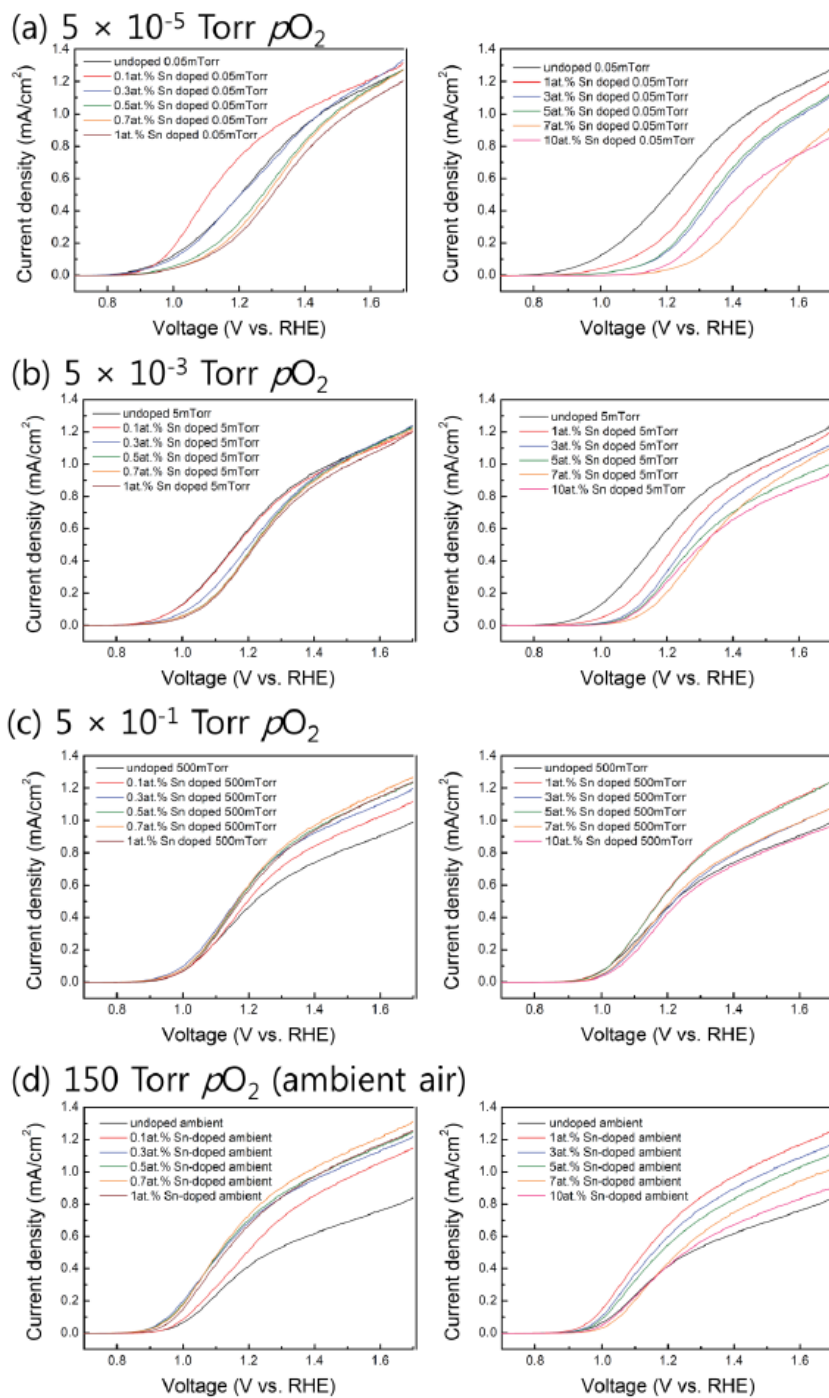


Figure 6.11 Photocurrent curves for various hematite films.

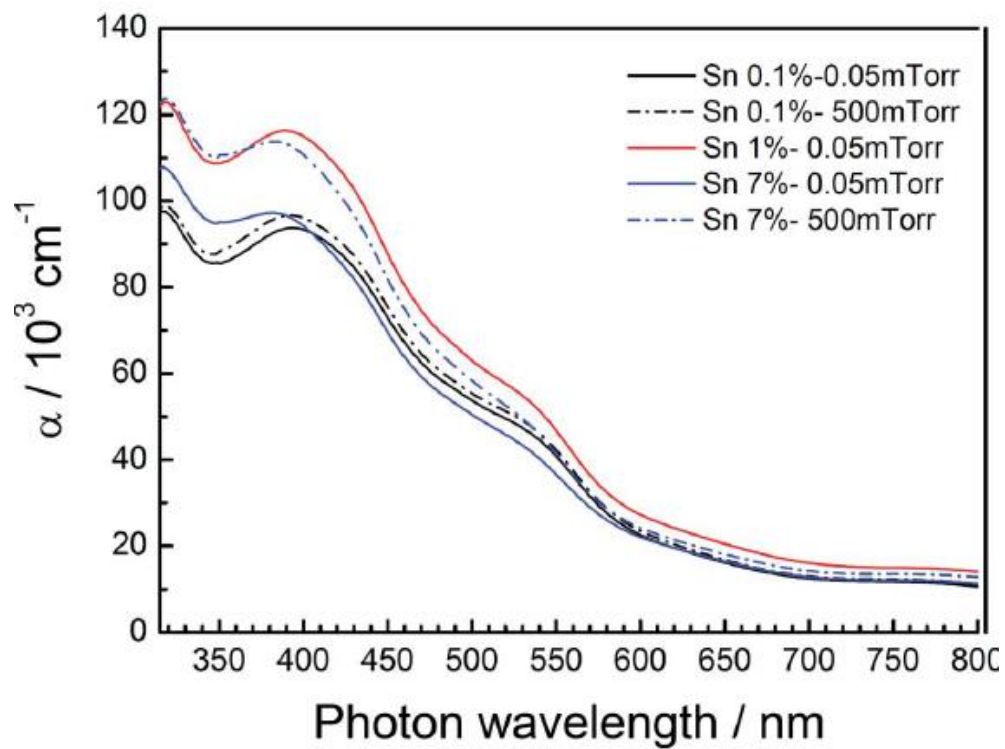


Figure 6.12 Optical property of hematite films in the various pO_2 and Sn concentration, which shows the absorption coefficient as a function of wavelength.

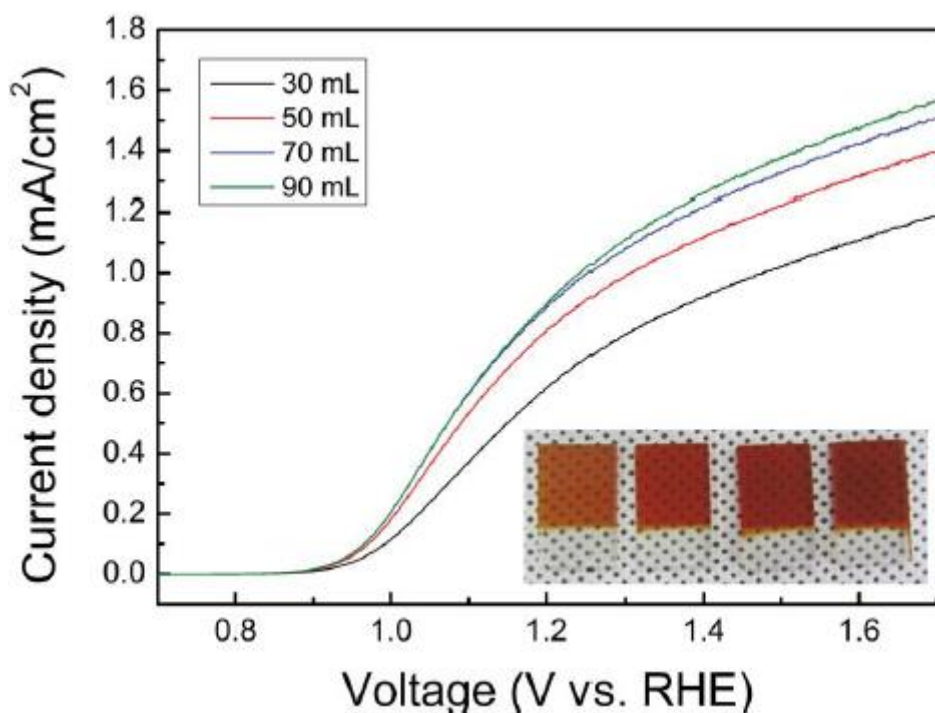


Figure 6.13 Photocurrent density for 1at.%-Sn-doped hematite film annealed at ambient air in various amount of precursor solution. Inset: photographs for hematite photoanode prepared by ASP using 30 ml, 50 ml, 70 ml, and 90 ml of precursor solution.

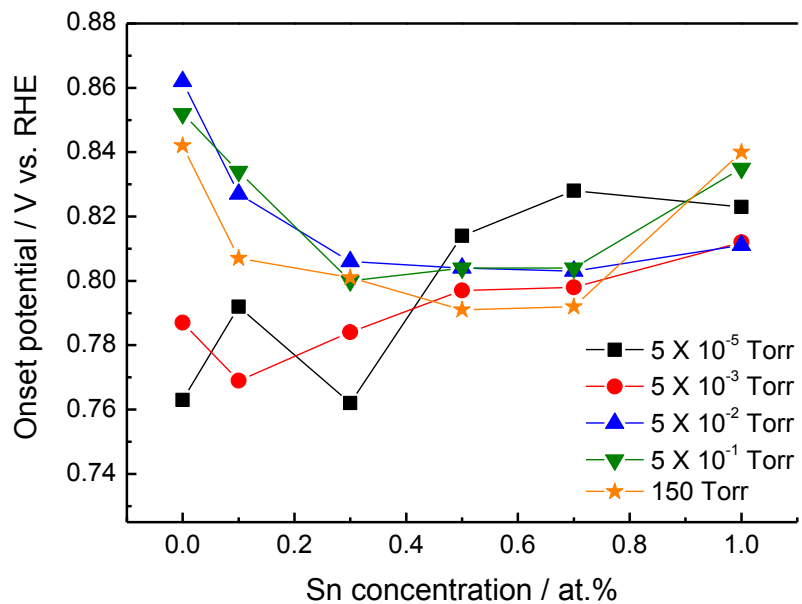


Figure 6.14 Photocurrent onset potential for hematite films as a function of the Sn concentration after pO_2 -controlled annealing under various pO_2 atmospheres.

6.4. Summary

By systematically varying the ratio between the oxygen vacancies and the Sn dopants, we demonstrated an enhancement in photoelectrochemical performance of hematite. High photocurrent and low overpotential were achieved using a newly developed, two-step process that enables the tuning of the concentration of oxygen vacancies. Hematite (α -Fe₂O₃) prepared through control of the oxygen partial pressure can exhibit a photocurrent that is significantly higher than that of normally annealed hematite. Furthermore, the enhancement effect is comparable to that of well-known Sn dopants under optimum condition. This enhancement can be explained by the improvement of electrical conductivity due to carrier generation from defects. These results suggest that control of the oxygen vacancy concentration in addition to control of extrinsic dopants represents another important route to improve the properties of oxide-based photoanodes. We expect that the design rule and controllability of nonstoichiometric defects presented here may be useful in the identification of the dopant and its activation.

CHAPTER 7

Development of Hierarchically Structured Fe₂O₃ Photoanode

(This chapter self-cites reference [7.1])

7.1. Introduction

Iron is one of the most abundant elements on the earth and can be processed or recycled via environmentally benign methods. In nature, iron readily exists as oxides, which have been regarded as useless materials. However, hematite (α -Fe₂O₃), the most common form of iron oxide, has recently attracted attention in photoelectrochemical water splitting as a photoanode material due to its small bandgap of approximately 2.0 eV that can absorb visible light [7.2] and its excellent chemical stability in aqueous solutions [7.3]. Despite these advantages, the performance of hematite photoanode is limited by low carrier conduction [7.4], the high recombination rate between electrons and holes [7.5], and the slow kinetics of the oxygen evolution reaction (OER) [7.6, 7].

Here, to overcome these intrinsic drawbacks of hematite, we designed a hierarchically nanostructured photoanode that is composed of the three types of iron-oxide: undoped hematite underlayer, Ti-doped hematite nanorods, and a β -FeOOH catalyst. We found that undoped hematite is an effective underlayer for improving both onset potential and photocurrent. Additionally, we demonstrated that the catalytic activity of β -FeOOH

reduces the resistance to charge transfer through the electrode/electrolyte interface.

Photoelectrochemical cell (PEC) is expected to offer the ability to sustainably produce hydrogen fuel from water by solar-driven water splitting. PEC mimics photosynthesis in nature using photoactive semiconductor electrodes, which can generate photo-excited carriers and transfer minority carriers to water to perform one half of the water splitting reaction. Oxidation (O₂ evolution, OER) occurs at the anode, and reduction (H₂ evolution, HER) occurs at the cathode [6.8]. The figures of merit to characterize the performance of the photoelectrode are the onset potential and the saturation current in the photocurrent curve. The value of the saturation current is determined by how many carriers can be generated by absorbed photons and how many photogenerated carriers can reach the electrode/electrolyte interface.

Hematite is an n-type semiconductor that can absorb photons with a wide range of energies, from near infrared to ultraviolet, through an indirect band-gap transition [6.3], which has the potential to convert 16.8 % of the sun's energy into hydrogen [6.9]. However, the lifetime of the excited carrier is very short, less than 100 ps, due to the fast recombination between holes and electrons and between holes and trap states. Additionally, charge carriers transported by polaron-hopping have very low mobility and thus, the diffusion length of excited carriers is short.

The low electron conductivity can be improved to a certain extent by increasing the carrier density through doping. Recently, we developed a strategy to tune the PEC performance of hematite by controlling the amount of oxygen vacancies and extrinsic dopants [6.10]. However, even the best well-known dopants, such as Si, Sn, and Ti, cannot sufficiently enhance the hole transport to make the photoanodic efficiency of hematite reach the theoretical limit. In planar hematite, the excited holes cannot fully participate in the OER because of the deep absorption depth compared to the space-

charge region and the hole-diffusion length [6.11, 12]. Nanostructuring is a viable solution to overcome this hole transfer problem because the relative volume of the space-charge layer increases with respect to that of bulk hematite. More photogenerated holes can reach the interface before recombination with electrons. For example, the best performance of hematite is obtained from nanostructured, Si-doped hematite [6.13].

Even in the well-defined nanostructured and doped hematite, the onset potential of approximately 0.9 V is substantially anodic compared to that of the flat-band potential (0.4 - 0.6 V vs. RHE) [6.14]. This large overpotential is associated with the slow kinetics for the OER on hematite and with the electronic and structural characteristic of the hematite/electrolyte and hematite/substrate interfaces [6.6, 15]. Because of the hole accumulation at the surface and the recombination in defects and surface states, a large overpotential is required for appreciable charge transfer from hematite to the electrolyte [6.16, 17]. Therefore, there have been much effort to reduce the hole accumulation by improving OER kinetics with electrocatalysts, such as Co-Pi [6.18] and IrO₂ [6.13]. To suppress the recombination at the semiconductor/substrate interface by improving crystallinity and blocking the back-diffusion of electrons, underlayers, such as SiO_x, Ga₂O₃, NbO₂, and TiO₂, have also been applied [6.19-21]. The improved charge transfer and reduced recombination at these two interfaces lower the overpotential for the OER and shifts the photocurrent curve in the cathodic direction.

To apply underlayers or catalysts on hematite with heterogeneous materials, the interface between the two materials with different crystal structures or unequal band gaps (heterojunction) is formed, but we developed a new strategy for the formation of the interface between the same types of or similar materials (homojunction) by employing iron-oxides as an underlayer and a catalyst. As with the improved hematite photoanode in our previous study, which was created by controlling only the intrinsic

defects with thermal treatments [6.10], we intend to improve the performance by designing a hierarchical nanostructure using only iron-oxides. By tuning the compositions and phases of the iron-oxides, the properties for an underlayer and catalyst activity can be achieved with iron oxides.

The hematite photoanode can be fabricated by a thermal treatment of β -FeOOH that is grown on an FTO substrate by hydrothermal synthesis, whereas without thermal treatment, β -FeOOH itself can be used for an electrocatalyst for the OER [6.22]. The catalytic activity of β -FeOOH on hematite for a photoelectrochemical OER has not yet been investigated. When the precursor for the dopant is excluded from the synthesis solution, undoped hematite is formed and can be employed as an underlayer. Although hematite without any dopants is an electrical insulator [6.4, 10], there has been no attempt to use undoped hematite as an underlayer for a hematite photoanode. This design strategy for an all-iron oxide based system assures homogeneity and low defect density at the interfaces, thus reducing the recombination centers in the electrode. The hydrothermal synthesis used in this study is a desirable method for fabricating an electrode for PEC. Inexpensive precursors and facilities can be used for the synthesis, and nanostructures with good crystallinity are easily obtained.

7.2. Fabrication of hierarchically nanostructured Fe₂O₃

The strategy for designing the photoanode is illustrated in Figure 7.1. The photoanode is composed of a hematite nanorod that is decorated with β -FeOOH catalyst branches. The hematite nanorod is doped with Ti to improve the electron conductivity. In addition, the diameter of the nanorod is comparable to the width of the space-charge region (w); therefore, most of the photogenerated holes can migrate to the surface before recombination. The catalyst on the surface accelerates the charge transport through the interface with the electrolyte. In addition, undoped hematite is coated on an FTO substrate as an insulating isomorphic underlayer to reduce the back-diffusion of electrons from the FTO and to improve the crystallinity at the interface between hematite and the FTO. The formation of crystalline defects from the lattice mismatch between the nanorod and the substrate can be suppressed.

Nanostructured iron-oxide photoanodes were prepared using the well-developed hydrothermal synthesis for oriented nanorod arrays of iron (III) oxide [6.23]. The [211]-oriented β -FeOOH nanorod arrays were uniformly formed on a substrate in an aqueous solution containing 0.15 M FeCl₃ and 1 M NaNO₃ during thermal treatment at 95 °C (Figure 7.2). The undoped underlayer was formed on an FTO substrate using this method with a reaction time of 50 min. As shown in Figure 7.2A, nanorods with heights of several tens of nanometers are uniformly grown on FTO surface. This undoped layer acts as a seed for the following formation of Ti-doped FeOOH nanorod as well as the underlayer. The Ti-doped nanorod array that was formed on the underlayer was prepared using the same synthesis method, except 1.5 mM titanium (IV) butoxide (Ti(OBu)₄) was also dissolved in the aqueous solution. To obtain the hematite phase through the dehydration of β -FeOOH, the prepared samples were annealed at 550 °C for 2 h in

ambient air. XPS spectra for Ti-doped hematite shows that Ti⁴⁺ ions are well incorporated in the lattice of hematite (Figure 7.3). The Ti/(Fe+Ti) atomic ratio in the Ti-doped hematite was measured to 1.7 at. % using inductively coupled plasma mass spectrometry (ICP-MS).

Figure 7.2B and 7.2D show the Ti-doped hematite nanorods grown on the undoped hematite underlayer (U/DH). The nanorod array uniformly covers the substrate but is not regularly aligned in the direction vertical to the substrate. The feature size of the Ti-doped nanorods is approximately 50 nm, which is similar to that of the undoped nanorods. However, the growth rate of the nanorod is decreased by more than a third. The synthesis should be maintained for 13 h to fabricate a Ti-doped nanorod array 500 nm in height, whereas similar height can be obtained after 4 h incubation in the case of undoped hematite.

Hematite nanorods prepared through this synthetic route have advantages for use as photoelectrodes; they not only have a small feature size and large surface area but also have high crystallinity. The small feature size and large surface area enable holes to easily transfer from the bulk to the surface. The diffraction pattern obtained during the TEM analysis (inset of Figure 7.2E) verified that the nanorod is a single crystal. In addition, a strong (110) peak in the X-ray diffraction pattern indicates that the nanorods are oriented in the [110] crystalline direction on the substrate (Figure 7.4). Because hematite has highly anisotropic electron transport with conduction within the (001) basal plane four orders of magnitude greater than the perpendicular directions, [110]-oriented nanorods are favorable for electron conduction to an FTO substrate. Because of these advantages, there have been attempts to form doped hematite nanorods for photoanodes using this hydrothermal synthetic method, but Sn-doping with SnCl₄ completely changed the morphology of the hematite from nanorods to nanocorals [6.24], and Ti-

doping with TiCN resulted in locally formed Ti-doped hematite nanorods [6.25]. However, in this study, we achieved uniformly Ti-doped hematite nanorods by adding a small amount of Ti(OBu)₄ in the FeCl₃ precursor solution. The uniform doping while maintaining the structure can be attributed to the preferential hydrolysis of titanium butoxide at a low rate in an aqueous solution due to its long alkyl group [6.26, 27]. The slow hydrolysis of titanium butoxide is favorable for incorporating Ti⁴⁺ ions into the Fe³⁺ sites in the hematite lattice with a uniform distribution.

When the Ti-doped hematite nanorod arrays were post-treated by hydrothermal conditioning for 20-50 min, β-FeOOH formed on the hematite surface in the shape of a branch. Figure 7.2C shows β-FeOOH nano-branches grown for 40 min on the Ti-doped hematite nanorod array (U/DH/A). The surface area increases by 14.3 % from 17.82 m²/g for U/DH to 20.36 m²/g for U/DH/A.

In the TEM images of Figure 7.2E and 7.2F, the β-FeOOH formed on the hematite nanorod is more clearly observed. From the high resolution TEM analysis, the β-FeOOH branches grow along the parallel direction to the (211) plane on a hematite nanorod (Figure 7.2F). The angle between the lattice fringes for (211)_{FeOOH} and (101)_{hematite} is 37.5°. When (211)_{FeOOH} is inclined at an angle of 37.5° to (110)_{hematite}, the interplanar spacing of (211)_{FeOOH} coincides with that of (101)_{hematite} (Figure S8), indicating that β-FeOOH branches epitaxially grow from the surface of a hematite nanorod. After 50 min of hydrothermal synthesis, the hierarchical structure with leaf-shaped β-FeOOH was observed (Figure 7.5). The β-FeOOH nano-branches grow on the hematite nanorods with either six-fold or two-fold symmetry.

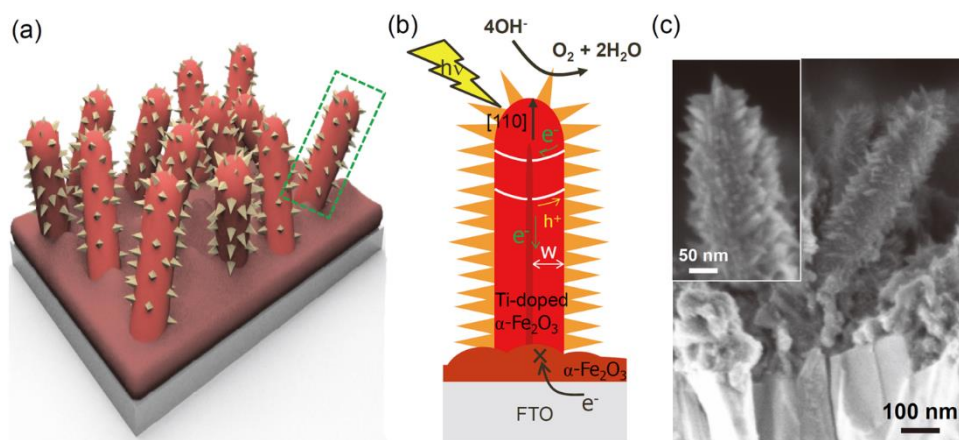


Figure 7.1 (A), (B) Scheme for a photoanode that consists of Ti-doped hematite nanorod arrays, an undoped hematite underlayer, and β -FeOOH-branched nanorods for a catalyst. (C) Cross-sectional images from the scanning electron microscope (SEM) for the photoanode with nanostructured triple layers that was synthesized by hydrothermal synthesis.

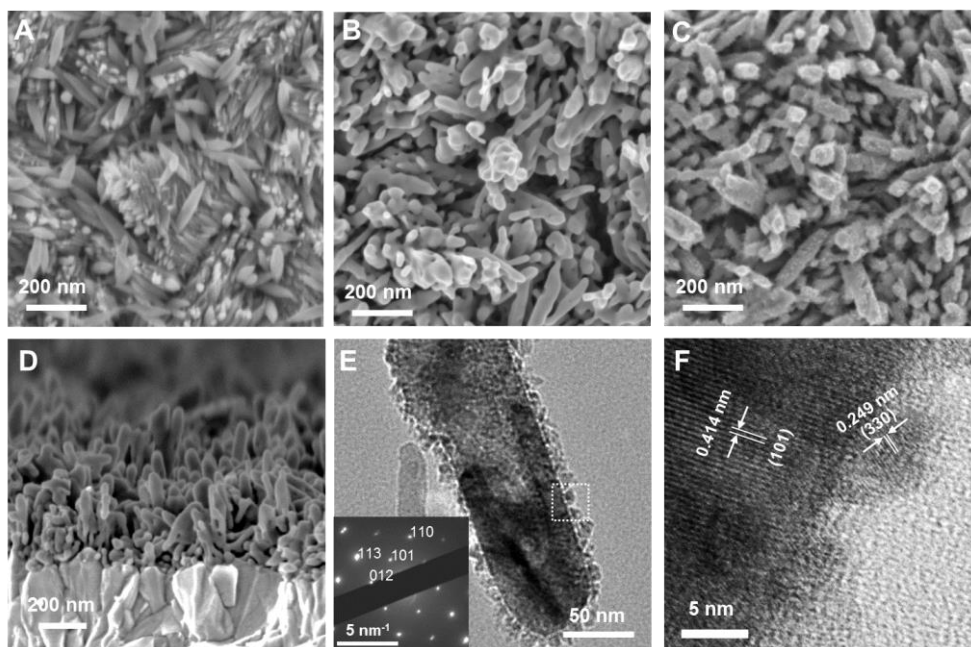


Figure 7.2 SEM top-view images of the hydrothermal-synthesized (A) undoped hematite underlayer, (B) Ti-doped hematite nanorods, and (C) β -FeOOH-branched nanorods. (D) SEM cross-sectional image of the Ti-doped hematite nanorods. (E) TEM image of the β -FeOOH-branched nanorods and (F) a higher resolution image.

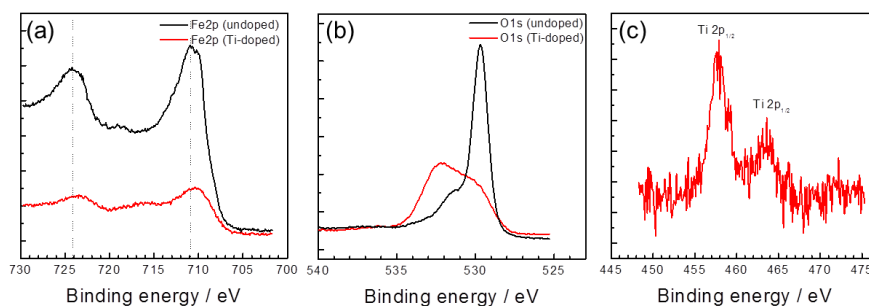


Figure 7.3 XPS spectra for (A) Fe2p, (B) Ti2p, and (C) O1s cores for undoped (black lines) and Ti-doped (red lines) hematite.

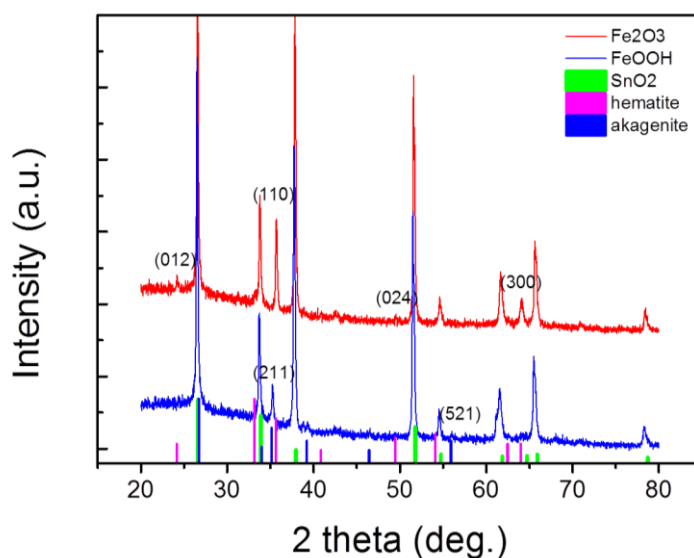


Figure 7.4 XRD patterns of β -FeOOH and hematite synthesized using hydrothermal method. The black line indicates hematite that has a preferred orientation of (110), and the red line indicates β -FeOOH that has a (211) orientation. The green dots indicate peaks from the FTO substrate.

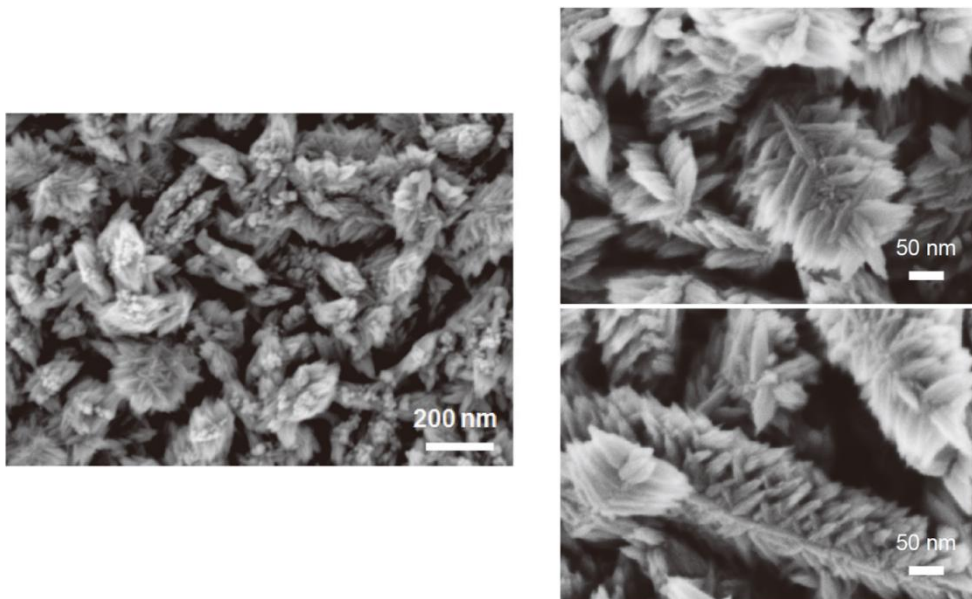


Figure 7.5 SEM images of hydrothermally synthesized hematite nanorods after additional hydrothermal synthesis for 50 min.

7.3. Effect of hierarchical structure on photocurrent density

Figure 7.6A presents the current density-potential (J - E) curves for the OER on the hematite photoanodes prepared using hydrothermal synthesis under light illumination (AM 1.5G, 100 mW cm⁻²) on the front side. All J - E curves for the nanostructured hematite electrodes in Figure 7.6A shows a stepwise shape. After onset, where the photocurrent exceeds the dark current, the photocurrent sharply increases as the anodic potential increases and then reaches a current plateau. When the potential reaches 1.60 V vs. RHE, the current starts to increase again due to the rising dark current (electrolysis of water). The onset potentials of the photocurrent and the saturated photocurrent density depend on the existence of the undoped underlayer and the β -FeOOH nano-branches.

Ti-doped hematite photoanodes (DH) show good performance in terms of photocurrent density and onset potential. In Figure 7.6A, the photocurrent starts to increase at 0.88 V vs. RHE and then rapidly increases to 1.20 V vs. RHE. The photocurrent density is saturated at approximately 1.30 V vs. RHE and is measured to be 1.37 mA cm⁻² at 1.40 V vs. RHE. The onset of dark current by water electrolysis is observed from 1.68 V vs. RHE. In comparison to the thin film of hematite (dash-dotted line in Figure 3a), which is a Sn-doped hematite film prepared by spray pyrolysis, the photocurrent from the hematite nanorod array shows a steeper increase and saturation at a lower potential. This difference in the shape of J - E curve results in the large difference in the photocurrent density at the potential before saturation. Although the saturated photocurrent density at 1.6 V vs. RHE is similar between the hematite nanorods (1.40 mA cm⁻²) and thin film hematite (1.43 mA cm⁻²), the current density at lower voltage (1.23 V vs. RHE) is considerably greater in the hematite nanorods (1.32 mA cm⁻²) than in the hematite film (0.87 mA cm⁻²).

This enhanced performance in nanostructured hematite is due not only to the enlarged surface area but also to the shortened transport distance of the photogenerated holes to the surface. The improvement in the rate of photocurrent increase is especially attributed to the small feature size of the nanorods. Because of the small feature size, the total volume of the nanorod can be within the space-charge region at a lower potential than with the film structure. This means that all of the photo-generated holes in the hematite nanorod can easily drift to the surface by the electric field from this potential. The photocurrent can be saturated and independent on the applied potential before the appearance of dark current. Therefore, the photocurrent curve shows a stepwise-shape.

The current density of 1.43 mA cm⁻² in DH indicates that the doping chemistry used in this study resulted in the effective incorporation of Ti-dopant in the hematite lattice. From Mott-Schottky plot (Figure 7.7), the increase in electron density more than 4 times was observed in Ti-doped hematite with a dielectric constant of 80 (Table 7.1). Despite the nanostructure, hematite nanorod array without dopant cannot generate photocurrent under the same test conditions as shown in Figure 3a (black line). Ti-dopants are activated by only the thermal treatment at 550 °C that is generally performed to transform the phase from β-FeOOH to hematite. In previous studies, the doped hematite photoanodes were annealed at temperatures greater than 700 °C to obtain considerable photocurrent density [6.24, 25], but such high temperature can induce the deformation of substrate and hematite nanostructure. The activation of the dopant at a lower temperature is another benefit of the Ti(OBu)₄ precursor for fabricating a doped hematite nanostructure. The easy activation also indicates that titanium(IV) ions are readily incorporated into the substitution sites of iron(III) ions during the growth of hematite.

Additional improvement in both the photocurrent density and the onset potential is achieved by adding the underlayer of undoped hematite. The saturated photocurrent

density at 1.40 V vs. RHE increases to 1.64 mA cm⁻² in U/DH, which is a 20 % larger photocurrent density than the photocurrent from DH. The onset potential of U/DH is negatively shifted by 40 mV (0.84 V vs. RHE) from that of DH, which is comparable to the onset from the catalyst-assisted hematite photoanode. When the onset potentials are defined by extrapolation to zero current from the linear portion of the *J-E* curve, the onset potential of U/DH is 0.90 V vs. RHE and that of cobalt-phosphate (Co-Pi)-assisted dendritic mesostructures of hematite is also 0.90 V vs. RHE [6.18].

The role of the underlayer is the suppression of electron diffusion from FTO, which would reduce the recombination of photo-generated holes near the hematite/FTO interface [6.20, 21]. Because undoped hematite has high electrical resistivity, the thin undoped hematite underlayer works as an effective barrier to the electron diffusion. In addition, unlike previous underlayer materials that form a heterojunction, the undoped hematite underlayer forms a homojunction with the hematite nanorods, thereby reducing recombination sites induced by the lattice mismatch between hematite and an underlayer. The reduced recombination of photogenerated holes can result in a cathodic shift of the onset potential and an increase of photocurrent density. The formation of an underlayer also increases the absorption coefficient of the hematite photoanode. (Figure 7.8).

When β-FeOOH nano-branches are formed on Ti-doped hematite nanorods (U/DH/A), the saturated photocurrent density is further improved. The maximum photocurrent density of 1.83 mA cm⁻² at 1.40 V vs. RHE is observed from the U/DH/A electrode in which β-FeOOH is grown for 20 min. The onset potential is positively shifted compared to the onset of U/DH, but the photocurrent density from U/DH/A becomes larger than that from U/DH at potentials over 1.20 V vs. RHE. Therefore, at 1.23 V vs. RHE and after saturation, the U/DH/A shows higher photocurrent density than the U/DH. Because the β-FeOOH activity of β-FeOOH with improved electron transport through Ti-doping

as well as improved photon absorption and suppressed recombination at the hematite/FTO interface using the underlayer.

However, the positive shift of the onset potential is contrast to a simple expectation to the catalytic effect of β -FeOOH. Generally, the catalysts for OER shift the onset potential to more negative potential. Indeed, as shown in Figure 7.6B, β -FeOOH induces a negative shift in the onset potential of the dark-current that is generated by electron transfer from electrolyte to hematite. In the U/DH/A in which β -FeOOH is grown for 40 min, the onset potential of dark current is negatively shifted to 1.5 V vs. RHE.

This onset potential of dark-current is comparable to that from the hematite decorated by Co-Pi which is one of the best catalysts for OER [6.18]. The positive shift of the onset potential seems to relate to the increase of flat-band potential by the β -FeOOH formation. The Mott-Schottky plot in Figure 7.7 shows that the flat-band potential of an electrode increases by approximately 0.2 V when β -FeOOH is grown on hematite (Table 7.1). Therefore, higher positive potential is required to form depletion layer that enables the separation of photogenerated holes from electrons. To clarify the origin of increasing the onset potential, more investigations on the electronic structure at electrolyte/ β -FeOOH and β -FeOOH/hematite interfaces are required.

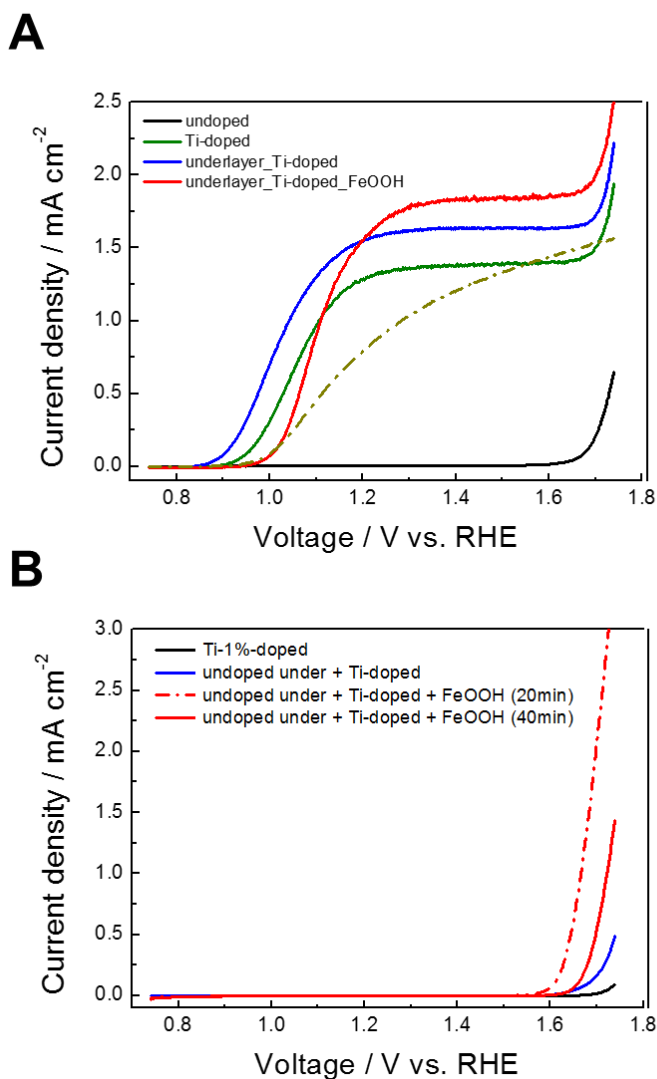


Figure 7.6 (A) Plots of the photocurrent for the undoped hematite nanorod array, DH, U/DH and U/DH/A with respect to the applied potential on the electrode. The photocurrent from the hematite film prepared by spray pyrolysis (dash-dotted line) is presented to show the effect of nanostructuring. (B) Current density for DH, U/DH, and U/DH/A measured in the dark.

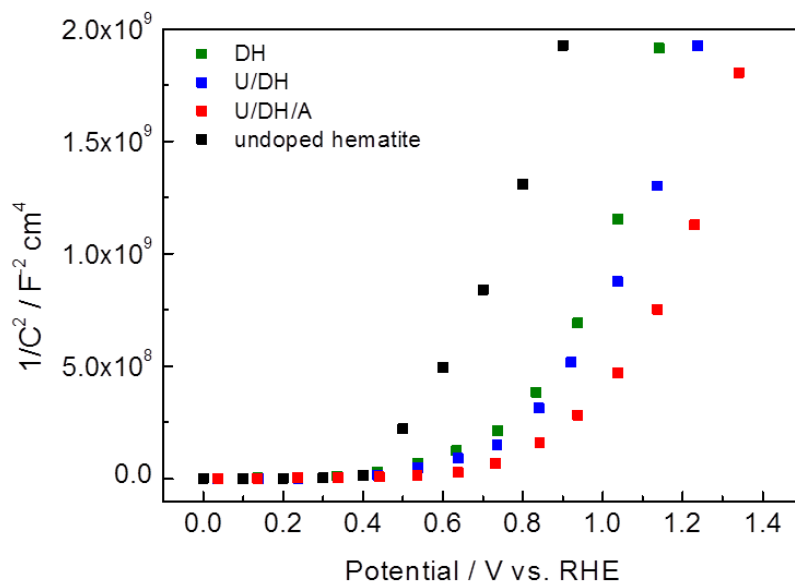


Figure 7.7 Mott-Schottky plot of DH, U/DH, U/DH/A, and undoped hematite nanorods measured under dark condition.

Table 7.1 Donor density and flat band potential from Mott-Schottky plot.

	Undoped hematite	DH	U/DH	U/DH/A
Donor density (cm ⁻²)	5.50×10^{20}	2.06×10^{21}	2.55×10^{21}	1.62×10^{21}
Flatband V (V vs. RHE)	0.42	0.44	0.46	0.65

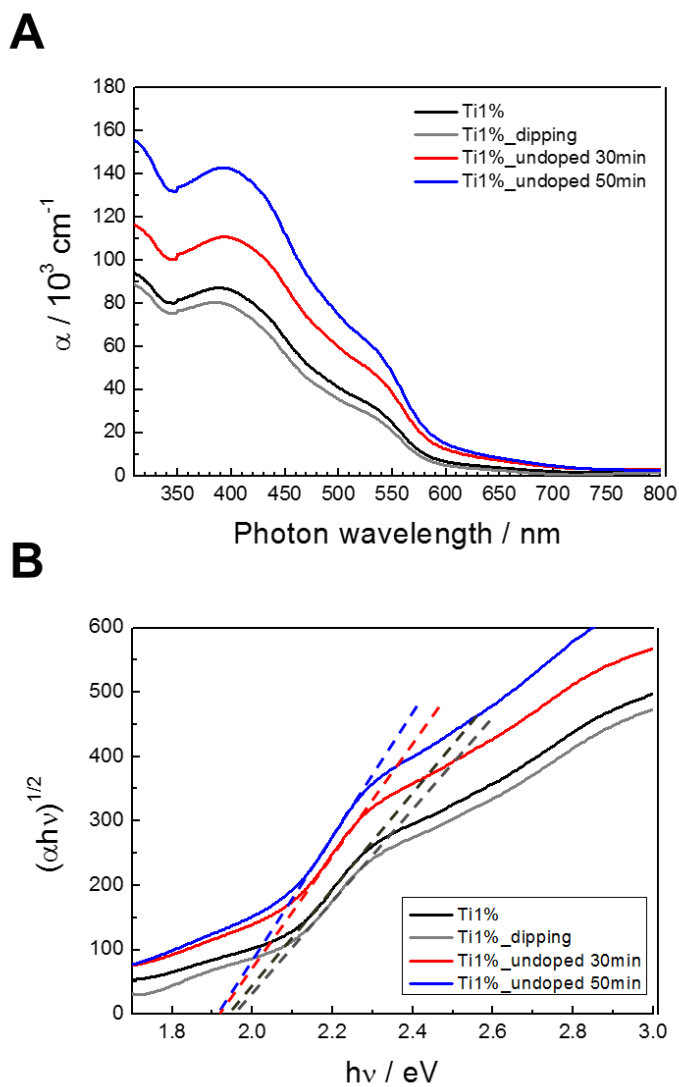


Figure 7.8 Absorbance of DH, U/DH, and U/DH/A from UV-visible spectroscopy.

7.4. Effects of β -FeOOH on charge transfer kinetics

7.4.1. Investigation of the transient photocurrent

To compare the charge transfer kinetics at the surface between the U/DH and U/DH/A, the transient photocurrents were measured (Figure 7.9). The poor kinetics leads to the charge accumulation at the surface and the recombination in the space charge layer [6.28, 29]. An anodic photocurrent transient when light is turned on corresponds to the recombination of holes near the reaction of electrons with the accumulated holes. The amount of accumulated photogenerated holes can be obtained by integrating the cathodic transient [6.30, 31].

Figure 7.9A and 7.9B show the *J-E* curves measured in the U/DH and U/DH/A under chopped light conditions. The anodic and cathodic transient peaks appear from the onset potentials and reach the maximum near the first inflection point of the photocurrents. Then, the disappearance of the transient peaks is observed from the voltage at which the photocurrents are saturated. The steady state photocurrent under light chopping well agrees with the photocurrent under constant illumination. The anodic and cathodic transient peak shows the similar intensity and voltage-dependence in both U/DH and U/DH/A. Therefore, it can be argued that the accumulated hole is the main recombination mechanism in our hematite photoanode.

The photocurrent transients in the U/DH and U/DH/A were quantitatively compared at 1.03 V and 1.23 V vs. RHE under a light pulse for 120 s, as shown in Figure 4c and 4d, respectively. In U/DH, photocurrent continuously decreases, which means the increase of hole accumulation near the surface with time. However, in U/DH/A, photocurrent reaches a steady state photocurrent after a short anodic transient. At 1.03

V vs. RHE, the density of accumulated holes obtained by integrating a cathodic transient curve is $12.34 \times 10^{-5} \text{ C cm}^{-2}$ and $7.55 \times 10^{-5} \text{ C cm}^{-2}$ in U/DH and U/DH/A, respectively. The accumulated charge densities of at 1.23 V vs. RHE are $6.19 \times 10^{-5} \text{ C cm}^{-2}$ and $3.64 \times 10^{-5} \text{ C cm}^{-2}$ in U/DH and U/DH/A, respectively. The accumulated hole near the surface in U/DH/A is less than that in U/DH. These results indicates that β -FeOOH stimulates the hole transfer from the electrode to the electrolyte and reduce the recombination in space charge layer.

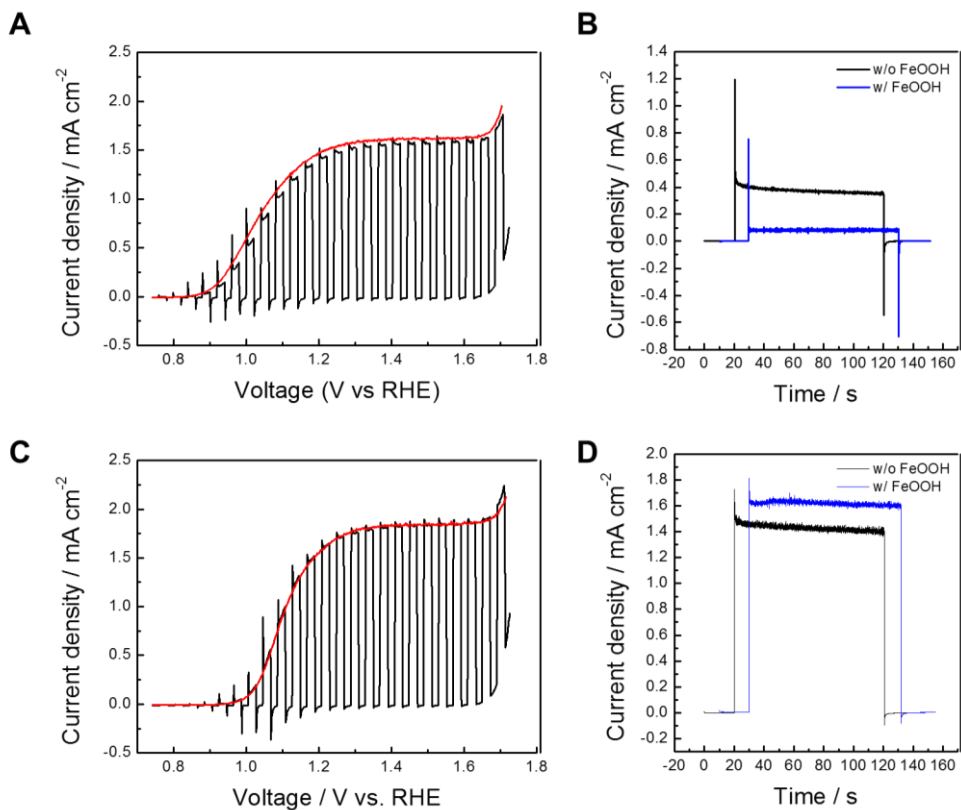


Figure 7.9 *J-E* curve during the chopping illumination for (A) without β -FeOOH catalyst branches and (B) with β -FeOOH catalyst branches. The *J-E* curves under constant illumination (red dashed line) and in the dark (green dash-dotted line) during the linear sweep are indicated. The transient curve of the photocurrent when the light is turned on and turned off at (C) 1.03 V vs. RHE and (D) 1.23 V vs. RHE.

7.4.2. Analysis by electrochemical impedance spectroscopy

The influences of the undoped underlayer and the β -FeOOH on the charge transport in the photoanode were further investigated using analyzing electrochemical impedance spectroscopy (EIS). Nyquist plots were constructed by measuring the frequency response of impedance with increasing applied potential under illumination. Figure 7.10B and 7.10C show the Nyquist plots of DH, U/DH, and U/DH/A at the applied potentials of 1.03 V and 1.23 V vs. RHE. Two semicircles are clearly observed in all types of photoanodes at 1.03 V vs. RHE. The small semicircle at high-frequency reflects the recombination of charges in bulk, and the other semicircle at low-frequency arises from the surface states of the electrodes. When the applied potential increases, the semicircle at the high-frequency is maintained but the large semicircle at the low-frequency is reduced. At more positive potentials, 1.23 V vs. RHE, the two semicircles are merged into a single semicircle.

The equivalent circuit parameters, which are described in Figure 7.10A based on previous EIS studies for hematite electrodes [7.32, 33], are extracted from fitting the EIS data (Figure 7.10D-F). As shown in Figure 7.10D, the resistance to electrons recombining with holes, R_{rec} , slightly changes in the same order, whereas the charge transfer resistance from surface state, R_{ss} , decreases an order of magnitude with increasing applied potentials until R_{ss} reaches a low value of several hundred ohms. The R_{ss} value of the U/DH/A is larger than those of DH and U/DH until 1.03 V vs. RHE, whereas the R_{ss} of U/DH/A shows the smallest value among the electrodes at potentials greater than 1.13 V vs. RHE. The higher R_{ss} value of U/DH/A at lower potential could be explained by the formation of energy barrier at hematite/ β -FeOOH interface. On the

contrary, the smallest value of R_{ss} of U/DH/A at higher potentials results in faster hole transfer at the surface, which relates to the catalytic activity of β -FeOOH.

The capacitance of the surface state, C_{ss} , show peaks at 1.03 V vs. RHE in DH and U/DH but at 1.13 V vs. RHE in U/DH/A. The peak value of C_{ss} is higher in U/DH/A compared to DH and U/DH. The value of C_{ss} is related to not only the amount of accumulated charge at surface but also surface area. Because the measurements of photocurrent denote that β -FeOOH reduces the hole accumulation, the highest value of C_{ss} in U/DH/A can be attributed to the increased surface area due to the formation of nano-branches.

Additionally, in Figure 7.10F, the effect of nanostructures on the hole transfer in bulk hematite can be discussed from evaluating the capacitance of the bulk hematite, C_{bulk} . The plot in Figure 7.10F corresponds to the Mott-Schottky plot (C^{-2} vs. potential) under illumination. In common with the Mott-Schottky in dark, U/DH/A shows larger intercept with the potential axis than the others, which reveals the increased flat-band potential by β -FeOOH. Above 1.2 V vs. RHE, C_{bulk} does not decrease any more, which argues that the width of space charge layer is fixed because entire volume of nanorods becomes the space-charge region. The advantage of nanostructure on the transport of photogenerated holes can be also confirmed from EIS analysis.

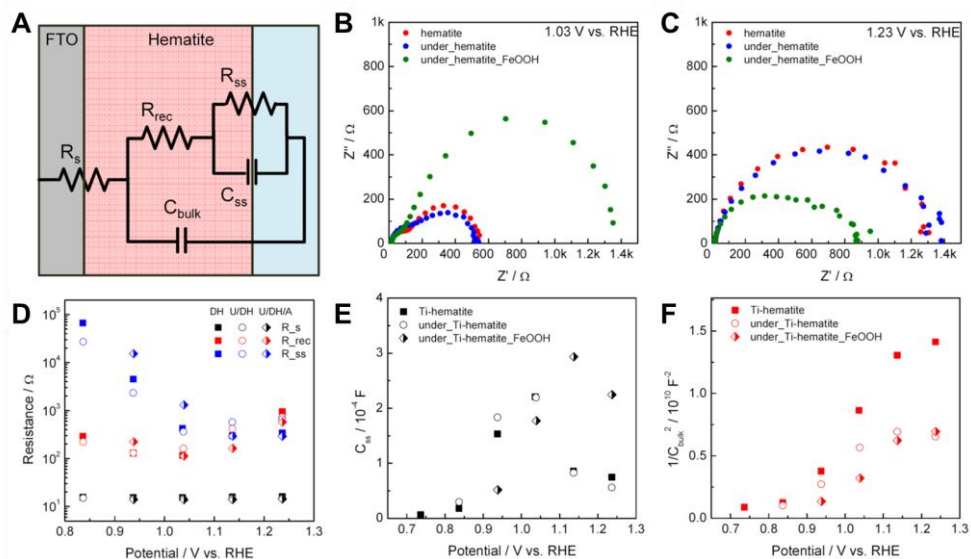


Figure 7.10 (A) Equivalent circuit for a hematite photoanode in aqueous electrolyte. Nyquist plots for DH, U/DH, and U/DH/A at (B) 1.03 V and (C) 1.23 V vs. RHE. (D) R_s (black symbols), R_{rec} (red symbols), and R_{ss} (blue symbols); (E) C_{ss} values; (F) Mott-Schottky plots from C_{bulk} for DH (closed square), U/DH (opened circle), and U/DH/A (half-opened diamond).

7.5. Summary

In this chapter, improvements in the photoelectrochemical performances of hematite photoanodes by applying iron oxide materials as an underlayer (undoped hematite) and as a catalyst for OER (β -FeOOH) are demonstrated. This all iron-based photoanode has a hierarchical nanostructure that enhances the transfer of photogenerated holes from the bulk hematite to the surface.

A Ti-doped hematite nanorod array is successfully fabricated by a hydrothermal synthesis and a thermal treatment under an acceptable temperature. The DH has high crystallinity and a small feature size, that leads to a low onset potential (~ 0.9 V vs. RHE) and the saturation of the photocurrent at a low potential (~ 1.2 V vs. RHE). The insertion of undoped hematite between the Ti-doped hematite nanorods and an FTO substrate results in a cathodic shift of the onset potential by 40 mV and an increase of photocurrent density by 20 %. The thin underlayer of undoped hematite has sufficient low conductivity to block the back-diffusion of electrons from the FTO and forms a homogeneous interface with low defect concentrations. The β -FeOOH nano-branches grown on the hematite nanorods induce a further increase in the photocurrent density to 1.83 mA cm^{-2} at 1.40 V vs. RHE. From electrochemical analyses including photocurrent transients, and EIS analysis, we found that β -FeOOH has catalytic activity that stimulates the charge transfer at the surface. However, the onset of photocurrent is anodically shifted by β -FeOOH. Our approaches for a high-performed photoanode show the effective way to minimize the recombination. Further research should focus on a catalyst layer to shift the onset potential more negatively with considering interfacial electronic structure as well as structural defects and chemical stability.

CHAPTER 8

Conclusion

8.1. Summary of results

The aim of this study is to develop a methodology that can precisely control the oxidation state of transition metal oxides, which is used as the photoelectrode for the photoelectrochemical CO₂ reduction. Controlling the oxidation state of transition metal oxide is critical to the performance of the photoelectrode because it controls the band structure by transformation of phase, and it also controls the intrinsic defects which can enhance the electrical conductivity and the surface activity. To control the oxidation state precisely, a thermodynamic calculation is performed to derive the thermodynamic and kinetic parameter of calcination, and we developed the system that can precisely control the gas atmosphere.

For the fabrication of mono-phase Cu₂O nanofiber photocathode for CO₂ reduction, electrospinning process is optimized to fabricate the nanofiber structure on FTO substrate. Using a high-boiling point solvent for the precursor solution of electrospinning and controlling the electrospinning time to 5 minutes was the key to enhance the adhesion of nanofiber to FTO substrate. After optimization of

electrospinning process, the reaction path of calcination of as-spun nanofibers to be transformed into copper oxide nanofibers is designed and optimized. Among the available reaction paths, only the reaction path that routes the CuO phase was successful of fabricating the copper oxide with nanofiber structure. Then the phase of copper oxide nanofiber is precisely controlled to mono-phase by thermodynamically programmed calcination process. The thermodynamic and kinetic parameter of calcination is predicted by the thermodynamic calculation, which derives the stability of each phase and the driving force of phase transformation at the given oxygen partial pressure. Interestingly, by varying the oxygen partial pressure and the calcination time, the mono-phase Cu₂O was formed at the condition where Cu₂O is metastable. At that condition, the kinetically processable window of mono-phase Cu₂O is discovered, which the condition that metastable Cu₂O is kinetically stable. To use the mono-phase Cu₂O nanofiber into the photocathode, a hierarchical structure is developed to optimize the photoactivity and photostability. A thin film Cu₂O improved the photoactivity of Cu₂O nanofiber electrode by blocking electron leakage from the FTO substrate. TiO₂ passivation layer prevents the photocorrosion of Cu₂O into metallic Cu, which improved the stability. By developing the mono-phase Cu₂O photocathode, CO₂ is photoelectrochemically converted to methanol with the faradic efficiencies over 90% in the aqueous electrolyte.

For the fabrication of nanostructured hematite photoanode for water oxidation, the oxygen vacancies are effectively generated by the annealing process that routes the Fe₃O₄ phase. The oxygen vacancies are systematically controlled by controlling the oxygen partial pressure during the annealing process, and it enhances the photocurrent density by giving rise to the electrical conductivity. Also, the interplay between the oxygen vacancy and the external dopant, Sn, is investigated. The photocurrent density

is further improved by optimizing the concentration of oxygen vacancy and external dopant. The hierarchical structure of hematite photoanode with the undoped-Fe₂O₃ underlayer and β-FeOOH co-catalyst. The undoped-Fe₂O₃ underlayer blocked the electron back transfer which recombines with the photogenerated holes in hematite which results in increase of overpotential. Therefore, by blocking the electron back transfer, undoped-Fe₂O₃ underlayer enhanced the onset potential of hematite photoanode. The β-FeOOH co-catalyst improved the OER kinetics at the surface of hematite. However, the β-FeOOH co-catalyst was effectively activated over a potential of 1.1 V vs. RHE. This behavior is analyzed by the photocurrent transient and the impedance spectroscopy.

It is expected that the methodology for rational design of the calcination strategy and the technique of precisely controlling the oxidation states of the transition metal oxide is broadly applicable to transition metal compounds that can be adopted to various catalytic applications.

8.2. Future works and suggested research

For the photocathode material for CO₂ reduction, a new material that is stable in aqueous condition is very promising. CuFeO₂, a natural p-type transition metal oxide is stable in aqueous condition even in the reducing environment. CuFeO₂ has a band gap about 1.7 eV, and quite negative conduction band edge position similar to Cu₂O which makes it a promising candidate material for a photocathode.

However, the nanostructured CuFeO₂ has not yet been developed, because it is very difficult to control both the nanostructure and the phase of transition metal oxide especially for the multinary oxide. Here, we are currently developing the CuFeO₂ with nanorod structure by first constructing the copper and iron oxide structure and followed by the thermodynamically programmed calcination to transform the phase of copper and iron oxide phase into the CuFeO₂. Also, the effect of defects (metal vacancy, metal substitution by dopant, and oxygen interstitial) in the CuFeO₂ on the photoactivity will also be investigated.

References

- [1.1] Cubasch, U. *et al.* Introduction. In *Climate Change 2013: The Physical Science Basis. Contribution of Working Group I to the Fifth Assessment Report of the Intergovernmental Panel on Climate Change*; Stocker, T. F., *et al.*, Eds; Cambridge University Press: Cambridge, United Kingdom and New York, NY, USA, (2013); pp 119-158.
- [1.2] G., V. D. *et al.* Introductory Chapter. In *Climate Change 2014: Mitigation of Climate Change. Contribution of Working Group III to the Fifth Assessment Report of the Intergovernmental Panel on Climate Change*; Edenhofer, O., *et al.*, Eds; Cambridge University Press: Cambridge, United Kingdom and New York, NY, USA, (2014); pp 111-150.
- [1.3] Chang, X. *et al.*, "CO₂ photo-reduction: insights into CO₂ activation and reaction on surfaces of photocatalysts." *Energy Environ. Sci.*, **9**, 2177-2196, (2016)
- [1.4] Kunkel, C. *et al.*, "Transition metal carbides as novel materials for CO₂ capture, storage, and activation." *Energy Environ. Sci.*, **9**, 141-144, (2016)
- [1.5] Halmann, M., "Photoelectrochemical reduction of aqueous carbon dioxide on p-type gallium phosphide in liquid junction solar cells." *Nature*, **275**, 115, (1978)
- [1.6] Inoue, T. *et al.*, "Photoelectrocatalytic reduction of carbon dioxide in aqueous suspensions of semiconductor powders." *Nature*, **277**, 637, (1979)
- [1.7] Kumar, B. *et al.*, "Photochemical and photoelectrochemical reduction of CO₂." *Annu. Rev. Phys. Chem.*, **63**, 541-569, (2012)

- [1.8] Walter, M. G. *et al.*, "Solar Water Splitting Cells." *Chem. Rev.*, **110**, 6446-6473, (2010)
- [1.9] Liu, X. W. *et al.*, "Cathodic catalysts in bioelectrochemical systems for energy recovery from wastewater." *Chem. Soc. Rev.*, **43**, 7718-7745, (2014)
- [1.10] Sivula, K. *et al.*, "Solar water splitting: progress using hematite α -Fe₂O₃ photoelectrodes." *ChemSusChem*, **4**, 432-449, (2011)
- [1.11] Lu, N. *et al.*, "CuO/Cu₂O nanofibers as electrode materials for non-enzymatic glucose sensors with improved sensitivity." *RSC Adv.*, **4**, 31056, (2014)
- [1.12] Luo, J. *et al.*, "Cu₂O Nanowire Photocathodes for Efficient and Durable Solar Water Splitting." *Nano Lett.*, **16**, 1848-1857, (2016)
- [1.13] Nakaoka, K. *et al.*, "Photoelectrochemical Behavior of Electrodeposited CuO and Cu₂O Thin Films on Conducting Substrates." *J. Electrochem. Soc.*, **151**, C661, (2004)
- [1.14] Ghadimkhani, G. *et al.*, "Efficient solar photoelectrosynthesis of methanol from carbon dioxide using hybrid CuO-Cu₂O semiconductor nanorod arrays." *Chem. Commun.*, **49**, 1297-1299, (2013)
- [1.15] Won, D. H. *et al.*, "Photoelectrochemical production of formic acid and methanol from carbon dioxide on metal-decorated CuO/Cu₂O-layered thin films under visible light irradiation." *Appl. Catal., B*, **158-159**, 217-223, (2014)
- [1.16] Rajeshwar, K. *et al.*, "Tailoring copper oxide semiconductor nanorod arrays for photoelectrochemical reduction of carbon dioxide to methanol." *ChemPhysChem*, **14**, 2251-2259, (2013)

- [1.17] Yu, J. *et al.*, "Solution-processed p-type copper oxide thin-film transistors fabricated by using a one-step vacuum annealing technique." *J. Mater. Chem. C*, **3**, 9509-9513, (2015)
- [1.18] Harilal, M. *et al.*, "Environment-Modulated Crystallization of Cu₂O and CuO Nanowires by Electrospinning and Their Charge Storage Properties." *Langmuir*, **34**, 1873-1882, (2018)
- [1.19] Li, J. *et al.*, "Nucleation and growth of Cu₂O in the reduction of CuO thin films." *Phys. Rev. B*, **45**, 5683-5686, (1992)
- [1.20] Li, J. *et al.*, "Oxidation and reduction of copper oxide thin films." *Mater. Chem. Phys.*, **32**, 1-24, (1992)
- [1.21] Kim, J. Y. *et al.*, "Reduction of CuO and Cu₂O with H₂: H Embedding and Kinetic Effects in the Formation of Suboxides." *J. Am. Chem. Soc.*, **125**, 10684-10692, (2003)
- [1.22] Rodriguez, J. A. *et al.*, "Reduction of CuO in H₂: *In Situ* Time-Resolved XRD Studies." *Catal. Lett.*, **85**, 247-254, (2003)
- [1.23] Paracchino, A. *et al.*, "Highly active oxide photocathode for photoelectrochemical water reduction." *Nat. Mater.*, **10**, 456-461, (2011)
- [1.24] de Jongh, P. E. *et al.*, "Photoelectrochemistry of Electrodeposited Cu₂O " *J. Electrochem. Soc.*, **147**, 486-489, (2000)
- [1.25] de Jongh, P. E. *et al.*, "Cu₂O: Electrodeposition and Characterization." *Chem. Mater.*, **11**, 3512-3517, (1999)
- [1.26] Sculfort, J. L. *et al.*, "Photoelectrochemical characterization of the p-Cu₂O-non aqueous electrolyte junction." *Electrochimica Acta*, **29**, 459-465, (1984)

- [1.27] Engel, C. J. *et al.*, "Photoelectrochemistry of Porous p-Cu₂O Films." *J. Electrochem. Soc.*, **155**, F37, (2008)
- [1.28] Sivula, K. *et al.*, "Photoelectrochemical Water Splitting with Mesoporous Hematite Prepared by a Solution-Based Colloidal Approach." *J. Am. Chem. Soc.*, **132**, 7436-7444, (2010)
- [1.29] Zboril, R. *et al.*, "Iron(III) Oxides from Thermal Processes Synthesis, Structural and Magnetic Properties, Mössbauer Spectroscopy Characterization, and Applications." *Chem. Mater.*, **14**, 969-982, (2002)
- [1.30] Morin, F. J., "Electrical Properties of α -Fe₂O₃ and α -Fe₂O₃ Containing Titanium." *Phys. Rev.*, **83**, 1005-1010, (1951)
- [1.31] Morin, F. J., "Electrical Properties of α -Fe₂O₃." *Phys. Rev.*, **93**, 1195-1199, (1954)
- [1.32] Goodenough, J. B., "Metallic oxides." *Prog. Solid State Chem.*, **5**, 145-399, (1971)
- [1.33] Rosso, K. M. *et al.*, "An ab initio model of electron transport in hematite (α -Fe₂O₃) basal planes." *J. Chem. Phys.*, **118**, 6455-6466, (2003)
- [1.34] Kennedy, J. H. *et al.*, "Photooxidation of Water at α -Fe₂O₃ Electrodes." *J. Electrochem. Soc.*, **125**, 709-714, (1978)
- [1.35] Itoh, K. *et al.*, "Stacked thin-film photoelectrode using iron oxide." *J. Appl. Phys.*, **56**, 874-876, (1984)
- [1.36] Itoh, K. *et al.*, "Thin Film Photoelectrochemistry: Iron Oxide." *J. Electrochem. Soc.*, **131**, 1266-1271, (1984)
- [2.1] Peter L.M., "Semiconductor Electrochemistry. In: Photoelectrochemical Solar Fuel Production.", Springer, Chambridge, (2016)

- [2.2] Doyle R.L. *et al.*, “The Oxygen Evolution Reaction: Mechanistic Concepts and Catalyst Design. In: Photoelectrochemical Solar Fuel Production.”, Springer, Chambridge, (2016)
- [2.3] Sudhagar P. *et al.*, “Hydrogen and CO₂ Reduction Reactions: Mechanisms and Catalysts. In: Photoelectrochemical Solar Fuel Production.”, Springer, Chambridge, (2016)
- [2.4] Wurfel, P. *et al.*, “Physics of solar cells. From basic principles to advanced concepts”, Wiley, Weinheim, (2009)
- [2.5] Sze SM, “Physics of semiconductor devices”, John Wiley & Sons Inc, New York, (1981)
- [2.6] Bard AJ, Faulkner LR, “Electrochemical methods: fundamentals and applications”, John Wiley & Sons Inc, New York, (2001)
- [2.7] Degryse, R. *et al.*, “Interpretation of Mott-Schottky plots determined at semiconductor-electrolyte systems.”, *J. Electrochem. Soc.*, **122**, 711-712, (1975)
- [2.8] Gartner WW, “Depletion layer photoeffects in semiconductors.”, *Phys. Rev.*, **116**, 84-87, (1959)
- [2.9] Butler MA, “Photoelectrolysis and physical properties of semiconducting electrode WO₃.”, *J. Appl. Phys.*, **48**, 1914-1920, (1977)
- [2.10] Reichman, J. “The current-voltage characteristics of semiconductor-electrolyte junction photovoltaic cells.”, *Appl. Phys. Lett.*, **36**, 574-577, (1980)

- [2.11] Li, J. *et al.*, “Surface recombination at semiconductor electrodes. 2. Photoinduced near-surface recombination centers in p-GaP.”, *J. Electroanal. Chem.*, **165**, 41-59, (1984)
- [2.12] Peter LM *et al.*, “Surface recombination at semiconductor electrodes. 1. Transient and steady-state photocurrents.”, *J. Electroanal. Chem.*, **165**, 29-40, (1984)
- [2.13] Li, J. *et al.*, “Surface recombination at semiconductor electrodes. 3. Steady-state and intensity modulated photocurrent response.”, *J. Electroanal. Chem.*, **193**, 27-47, (1985)
- [2.14] Li, J. *et al.*, “Surface recombination at semiconductor electrodes. 4. Steady-State and Intensity modulated photocurrents at normal GaAs electrodes.”, *J. Electroanal. Chem.*, **199**, 1-26, (1986)
- [2.15] Indrakanti, P. *et al.*, “Photoinduced activation of CO₂ on Ti-based heterogeneous catalysts: Current state, chemical physics-based insights and outlook.”, *Energy Environ. Sci.*, **2**, 745-758, (2009)
- [2.16] Yang, C. *et al.*, “Artificial Photosynthesis over Crystalline TiO₂-Based Catalysts: Fact or Fiction?”, *J. Am. Chem. Soc.*, **132**, 8398-8406, (2010)
- [2.17] Mao, J. *et al.*, “Recent advances in the photocatalytic CO₂ reduction over semiconductors.”, *Catal. Sci. Technol.*, **3**, 2481-2498, (2013)
- [2.18] Tahir, M. *et al.*, “Advances in visible light responsive titanium oxide-based photocatalysts for CO₂ conversion to hydrocarbon fuels.”, *Energy. Convers. Manag.*, **76**, 194-214, (2013)
- [2.19] Koci, K. *et al.*, “Photocatalytic reduction of CO₂ over TiO₂ based catalysts.”, *Chem. Pap.*, **62**, 1-9, (2008)

- [2.20] Habisreutinger SN *et al.*, "Photocatalytic reduction of CO₂ on TiO₂ and other semiconductors." *Angew. Chem. Int. Ed.*, **52**, 7372-7408, (2013)
- [2.21] Kumar, B. *et al.*, "Photochemical and photoelectrochemical reduction of CO₂." *Annu. Rev. Phys. Chem.*, **63**, 541-569, (2012)
- [2.22] Fu, J. *et al.*, "Enhanced photocatalytic CO₂-reduction activity of electrospun mesoporous TiO₂ nanofibers by solvothermal treatment.", *Dalton Trans.*, **43**, 9158-9165, (2014)
- [2.23] Xie, S. J. *et al.*, "Photocatalytic reduction of CO₂ with H₂O: significant enhancement of the activity of Pt-TiO₂ in CH₄ formation by addition of MgO.", *Chem. Commun.*, **49**, 2451-2453, (2013)
- [2.24] Zhai, Q. G. *et al.*, "Photocatalytic conversion of carbon dioxide with water into methane: platinum and copper(I) oxide co-catalysts with a core-shell structure.", *Angew. Chem. Int. Ed.*, **52**, 5776-5779, (2013)
- [2.25] Xu, H. *et al.*, "Porous-structured Cu₂O/TiO₂ nanojunction material toward efficient CO₂ photoreduction.", *Nanotechnology*, **25**, 165402, (2014)
- [2.26] Wang, Y. *et al.*, "Ordered mesoporous CeO₂-TiO₂ composites: Highly efficient photocatalysts for the reduction of CO₂ with H₂O under simulated solar irradiation.", *Appl. Catal., B*, **130**, 277-284, (2013)
- [2.27] Liu, L. J. *et al.*, "Porous microspheres of MgO-patched TiO₂ for CO₂ photoreduction with H₂O vapor: temperature-dependent activity and stability.", *Chem. Commun.*, **49**, 3664-3666, (2013)
- [2.28] Krejčíková, S. *et al.*, "Preparation and characterization of Ag-doped crystalline titania for photocatalysis applications.", *Appl. Catal. Environ.*, **111**, 119-125, (2012)

- [2.29] Zhang, X. *et al.*, “Photocatalytic conversion of diluted CO₂ into light hydrocarbons using periodically modulated multiwalled nanotube arrays.”, *Angew. Chem. Int. Ed.*, **51**, 12732-12735, (2012)
- [2.30] Zhang, Z. *et al.*, “Au/Pt Nanoparticle-Decorated TiO₂ Nanofibers with Plasmon-Enhanced Photocatalytic Activities for Solar-to-Fuel Conversion.”, *J. Phys. Chem. C*, **117**, 25939-25947, (2013)
- [2.31] Tu, W. *et al.*, “Versatile Graphene-Promoting Photocatalytic Performance of Semiconductors: Basic Principles, Synthesis, Solar Energy Conversion, and Environmental Applications.”, *Adv. Func. Mater.*, **23**, 4996-5008, (2013)
- [2.32] Gui, M. *et al.*, “Modification of MWCNT@TiO₂ core-shell nanocomposites with transition metal oxide dopants for photoreduction of carbon dioxide into methane.”, *Appl. Surf. Sci.*, **319**, 37-43, (2014)
- [2.33] Yan, S. *et al.*, “Zinc Gallogermanate Solid Solution: A Novel Photocatalyst for Efficiently Converting CO₂ into Solar Fuels.”, *Adv. Funct. Mater.*, **23**, 1839-1845, (2013)
- [2.34] Teramura, K. *et al.*, “A doping technique that suppresses undesirable H₂ evolution derived from overall water splitting in the highly selective photocatalytic conversion of CO₂ in and by water.”, *Chem. Eur. J.*, **20**, 9906-9909, (2014)
- [2.35] Liu, Q. *et al.*, “Controllable Hydrothermal Synthesis of Cd₂Ge₂O₆ Nanostructures.”, *Adv. Mater. Phys. Chem.*, **4**, 134-140, (2014)
- [2.36] Li, P. *et al.*, “The Effects of Crystal Structure and Electronic Structure on Photocatalytic H₂ Evolution and CO₂ Reduction over Two Phases of Perovskite-Structured NaNbO₃.”, *J. Phys. Chem. C*, **116**, 7621-7628, (2012)

- [2.37] Lu, Y. *et al.*, “Exfoliated carbon nitride nanosheets decorated with NiS as an efficient noble-metal-free visible-light-driven photocatalyst for hydrogen evolution.”, *Phys. Chem. Chem. Phys.*, **17**, 17355-17361, (2015)
- [2.38] Teramura, K. *et al.*, “Photocatalytic conversion of CO₂ in water over layered double hydroxides.”, *Angew. Chem. Int. Ed.*, **51**, 8008-8011, (2012)
- [2.39] An, C. *et al.*, “Strongly visible-light responsive plasmonic shaped AgX:Ag (X = Cl, Br) nanoparticles for reduction of CO₂ to methanol.”, *Nanoscale*, **4**, 5646-5650, (2012)
- [2.40] Xi, G. *et al.*, “Ultrathin W₁₈O₄₉ nanowires with diameters below 1 nm: synthesis, near-infrared absorption, photoluminescence, and photochemical reduction of carbon dioxide.”, *Angew. Chem. Int. Ed.*, **51**, 2395-2399, (2012)
- [2.41] Lekse, J. *et al.*, “Synthesis, characterization, electronic structure, and photocatalytic behavior of CuGaO₂ and CuGa_{1-x}Fe_xO₂ (x = 0.05, 0.10, 0.15, 0.20) Delafossites.”, *J. Phys. Chem. C*, **116**, 1865-1872, (2012)
- [2.42] Stock, M. *et al.*, “LiNbO₃-a polar material for solid-gas artificial photosynthesis.”, *Ferroelectrics.*, **419**, 9-13, (2011)
- [2.43] Zhou, Y. *et al.*, “High-yield synthesis of ultrathin and uniform Bi₂WO₆ square nanoplates benefitting from photocatalytic reduction of CO₂ into renewable hydrocarbon fuel under visible light.”, *ACS Appl. Mater. Interfaces*, **3**, 3594-3601, (2011)
- [2.44] Liu, Y. *et al.*, “Selective ethanol formation from photocatalytic reduction of carbon dioxide in water with BiVO₄ photocatalyst.”, *Catalysis Commun.*, **11**, 210-213, (2009)

- [2.45] Yuliati, L. *et al.*, "Photocatalytic conversion of methane and carbon dioxide over gallium oxide.", *Chem. Phys. Lett.*, **452**, 178-182, (2008)
- [2.46] Lo, C. *et al.*, "Photoreduction of carbon dioxide with H₂ and H₂O over TiO₂ and ZrO₂ in a circulated photocatalytic reactor.", *Sol. Energ. Mat. Sol. Cells*, **91**, 1765-1774, (2007)
- [2.47] Teramura, K. *et al.*, "Photocatalytic reduction of CO₂ to CO in the presence of H₂ or CH₄ as a reductant over MgO.", *J. Phys. Chem. B*, **108**, 346-354, (2004)
- [2.48] Yahaya, A. *et al.*, "Selective laser enhanced photocatalytic conversion of CO₂ into methanol.", *Chem. Phys. Lett.*, **400**, 206-212, (2004)
- [2.49] Bockris, J. *et al.*, "Mechanism of oxygen evolution on perovskites.", *J. Phys. Chem.*, **87**, 2960-2971, (1983)
- [2.50] Krasil'shchikov, A. *et al.*, "Intermediate stages in the anodic evolution of oxygen.", *Zh. Fiz. Khim.*, **37**, 531, (1963)
- [2.51] Kobussen, A. *et al.*, "The oxygen evolution on La_{0.5}Ba_{0.5}CoO₃: theoretical impedance behavior for a multi-step mechanism involving two adsorbates.", *J. Electroanal. Chem.*, **126**, 221-240, (1981)
- [2.52] Willems, H. *et al.*, "The oxygen evolution reaction on cobalt. Part 1. Reaction order experiments and impedance measurements.", *J. Electroanal. Chem.*, **170**, 227-242, (1984)
- [2.53] O'Grady, W. *et al.*, In *Proceedings of the symposium on electrocatalysis*; Breiter, M., Eds; The Electrochemical Society Inc.: Pennington, NJ, (1974); p 286.

- [2.54] Rossmeisl, J. *et al.*, “Electrolysis of water on oxide surfaces.”, *J. Electroanal. Chem.*, **607**, 83-89, (2004)
- [2.55] Rossmeisl, J. *et al.*, “Electrolysis of water on (oxidized) metal surfaces.”, *Chem. Phys.*, **319**, 178-184, (2005)
- [2.56] Dau, H. *et al.*, “The mechanism of water oxidation: from electrolysis via homogeneous to biological catalysis.”, *ChemCatChem*, **2**, 724-761, (2010)
- [2.57] Koper, M. *et al.*, In *Fuel cell science: theory, fundamentals and bio-catalysis*; Wiekowski, J., Eds; Wiley: New York, (2010); pp 71-110.
- [2.58] Rossmeisl, J., In *Chemical energy storage*; Schlogl, R, Eds; De Gruyter Graduate: Berlin, (2013); pp 151-162.
- [2.59] Dumesic, J. *et al.*, In *Handbook of heterogeneous catalysis*; Ertl, G., *et al.*, Eds; Wiley: Weinheim, (2008); p 1445.
- [2.60] Koper, M. *et al.*, “Analysis of electrocatalytic reaction schemes: distinction between rate-determining and potential-determining steps.”, *J. Solid State Electrochem.*, **17**, 339-344, (2013)
- [2.61] Sabatier, P. *et al.*, “Hydrogenation and dehydrogenation by catalysis.”, *Ber. Dtsch. Chem. Ges.*, **44**, 1984-2001, (1911)
- [2.62] Trasatti, S. *et al.*, “Electrocatalysis by oxides – attempt at a unifying approach.”, *J. Electroanal. Chem.*, **111**, 125-131, (1980)
- [2.63] Trasatti, S. *et al.*, “Electrocatalysis in the anodic evolution of oxygen and chlorine.”, *Electrochim. Acta*, **29**, 1503-1512, (1984)
- [3.1] Yang, T. *et al.*, “A new hematite photoanode doping strategy for solar water splitting: oxygen vacancy generation.”, *Phys. Chem. Chem. Phys.*, **15**, 2117-2124, (2013)

- [3.2] Yang, T. *et al.*, "An iron oxide photoanode with hierarchical nanostructure for efficient water oxidation.", *J. Mater. Chem. A*, **2**, 2297-2305, (2014)
- [4.1] Cubasch, U. *et al.* Introduction. In *Climate Change 2013: The Physical Science Basis. Contribution of Working Group I to the Fifth Assessment Report of the Intergovernmental Panel on Climate Change*; Stocker, T. F., *et al.*, Eds; Cambridge University Press: Cambridge, United Kingdom and New York, NY, USA, 2013; pp 119-158.
- [4.2] G., V. D. *et al.* Introductory Chapter. In *Climate Change 2014: Mitigation of Climate Change. Contribution of Working Group III to the Fifth Assessment Report of the Intergovernmental Panel on Climate Change*; Edenhofer, O., *et al.*, Eds; Cambridge University Press: Cambridge, United Kingdom and New York, NY, USA, 2014; pp 111-150.
- [4.3] Chang, X. *et al.*, "CO₂ Photo-Reduction: Insights into CO₂ Activation and Reaction on Surfaces of Photocatalysts." *Energy Environ. Sci.*, **9**, 2177-2196, (2016)
- [4.4] Kunkel, C. *et al.*, "Transition Metal Carbides as Novel Materials for CO₂ Capture, Storage, and Activation." *Energy Environ. Sci.*, **9**, 141-144, (2016)
- [4.5] Inoue, T. *et al.*, "Photoelectrocatalytic Reduction of Carbon Dioxide in Aqueous Suspensions of Semiconductor Powders." *Nature*, **277**, 637, (1979)
- [4.6] Halmann, M., "Photoelectrochemical Reduction of Aqueous Carbon Dioxide on p-type Gallium Phosphide in Liquid Junction Solar Cells." *Nature*, **275**, 115, (1978)

- [4.7] Jang, Y. J. *et al.*, "Selective CO Production by Au Coupled ZnTe/ZnO in the Photoelectrochemical CO₂ Reduction System." *Energy Environ. Sci.*, **8**, 3597-3604, (2015)
- [4.8] Azuma, M. *et al.*, "Electrochemical Reduction of Carbon Dioxide on Various Metal Electrodes in Low-Temperature Aqueous KHCO₃ Media." *J. Electrochem. Soc.*, **137**, 1772, (1990)
- [4.9] Benson, E. E. *et al.*, "Electrocatalytic and Homogeneous Approaches to Conversion of CO₂ to Liquid Fuels." *Chem. Soc. Rev.*, **38**, 89-99, (2009)
- [4.10] Kumar, B. *et al.*, "Photochemical and Photoelectrochemical Reduction of CO₂." *Annu. Rev. Phys. Chem.*, **63**, 541-569, (2012)
- [4.11] Schreier, M. *et al.*, "Efficient and Selective Carbon Dioxide Reduction on Low Cost Protected Cu₂O Photocathodes Using a Molecular Catalyst." *Energy Environ. Sci.*, **8**, 855-861, (2015)
- [4.12] Mott, N. F., "A Discussion of the Transition Metals on the Basis of Quantum Mechanics." *Proc. Phys. Soc.*, **47**, 571, (1935)
- [4.13] Walter, M. G. *et al.*, "Solar Water Splitting Cells." *Chem. Rev.*, **110**, 6446-6473, (2010)
- [4.14] Raj, I. A. *et al.*, "Transition Metal-Based Hydrogen Electrodes in Alkaline Solution-Electrocatalysis on Nickel Based Binary Alloy Coatings." *J. Appl. Electrochem.*, **20**, 32-38, (1990)
- [4.15] Brown, D. E. *et al.*, "Low Overvoltage Electrocatalysts for Hydrogen Evolving Electrodes." *Int. J. Hydrogen Energy*, **7**, 405-410, (1982)

- [4.16] Wendt, H. *et al.*, "Electrocatalytic and Thermal Activation of Anodic Oxygen- and Cathodic Hydrogen-Evolution in Alkaline Water Electrolysis." *Electrochim. Acta*, **28**, 27-34, (1983)
- [4.17] Raj, I. A., "Nickel-Based, Binary-Composite Electrocatalysts for the Cathodes in the Energy-Efficient Industrial Production of Hydrogen from Alkaline-Water Electrolytic Cells." *J. Mater. Sci.*, **28**, 4375-4382, (1993)
- [4.18] Hou, J. *et al.*, "High-Performance p-Cu₂O/n-TaON Heterojunction Nanorod Photoanodes Passivated with an Ultrathin Carbon Sheath for Photoelectrochemical Water Splitting." *Energy Environ. Sci.*, **7**, 3758-3768, (2014)
- [4.19] Kim, H.-i. *et al.*, "N-Doped TiO₂ Nanotubes Coated with a Thin TaO_xN_y Layer for Photoelectrochemical Water Splitting: Dual Bulk and Surface Modification of Photoanodes." *Energy Environ. Sci.*, **8**, 247-257, (2015)
- [4.20] Ning, F. *et al.*, "TiO₂/Graphene/NiFe-Layered Double Hydroxide Nanorod Array Photoanodes for Efficient Photoelectrochemical Water Splitting." *Energy Environ. Sci.*, **9**, 2633-2643, (2016)
- [4.21] Shen, S. *et al.*, "Hematite Heterostructures for Photoelectrochemical Water Splitting: Rational Materials Design and Charge Carrier Dynamics." *Energy Environ. Sci.*, **9**, 2744-2775, (2016)
- [4.22] Lu, N. *et al.*, "CuO/Cu₂O Nanofibers as Electrode Materials for Non-enzymatic Glucose Sensors with Improved Sensitivity." *RSC Adv.*, **4**, 31056, (2014)
- [4.23] Luo, J. *et al.*, "Cu₂O Nanowire Photocathodes for Efficient and Durable Solar Water Splitting." *Nano Lett.*, **16**, 1848-1857, (2016)

- [4.24] Nakaoka, K. *et al.*, "Photoelectrochemical Behavior of Electrodeposited CuO and Cu₂O Thin Films on Conducting Substrates." *J. Electrochem. Soc.*, **151**, C661, (2004)
- [4.25] Liu, X. W. *et al.*, "Cathodic Catalysts in Bioelectrochemical Systems for Energy Recovery from Wastewater." *Chem. Soc. Rev.*, **43**, 7718-7745, (2014)
- [4.26] Ghadimkhani, G. *et al.*, "Efficient Solar Photoelectrosynthesis of Methanol From Carbon Dioxide Using Hybrid CuO-Cu₂O Semiconductor Nanorod Arrays." *Chem. Commun.*, **49**, 1297-1299, (2013)
- [4.27] Won, D. H. *et al.*, "Photoelectrochemical Production of Formic Acid and Methanol from Carbon Dioxide on Metal-decorated CuO/Cu₂O-Layered Thin Films Under Visible Light Irradiation." *Appl. Catal., B*, **158-159**, 217-223, (2014)
- [4.28] Rajeshwar, K. *et al.*, "Tailoring Copper Oxide Semiconductor Nanorod Arrays for Photoelectrochemical Reduction of Carbon Dioxide to Methanol." *ChemPhysChem*, **14**, 2251-2259, (2013)
- [4.29] Yu, J. *et al.*, "Solution-Processed p-type Copper Oxide Thin-Film Transistors Fabricated by Using a One-Step Vacuum Annealing Technique." *J. Mater. Chem. C*, **3**, 9509-9513, (2015)
- [4.30] Harilal, M. *et al.*, "Environment-Modulated Crystallization of Cu₂O and CuO Nanowires by Electrospinning and Their Charge Storage Properties." *Langmuir*, **34**, 1873-1882, (2018)
- [4.31] Li, J. *et al.*, "Nucleation and Growth of Cu₂O in the Reduction of CuO Thin Films." *Phys. Rev. B*, **45**, 5683-5686, (1992)

- [4.32] Li, J. *et al.*, "Oxidation and Reduction of Copper Oxide Thin Films." *Mater. Chem. Phys.*, **32**, 1-24, (1992)
- [4.33] Kim, J. Y. *et al.*, "Reduction of CuO and Cu₂O with H₂: H Embedding and Kinetic Effects in the Formation of Suboxides." *J. Am. Chem. Soc.*, **125**, 10684-10692, (2003)
- [4.34] Rodriguez, J. A. *et al.*, "Reduction of CuO in H₂: *In Situ* Time-Resolved XRD Studies." *Catal. Lett.*, **85**, 247-254, (2003)
- [4.35] Paracchino, A. *et al.*, "Highly Active Oxide Photocathode for Photoelectrochemical Water Reduction." *Nat. Mater.*, **10**, 456-461, (2011)
- [4.36] Nam, D.-H. *et al.*, "One-Step Structure Modulation of Electrospun Metal-Loaded Carbon Nanofibers: Redox Reaction Controlled Calcination." *Carbon*, **82**, 273-281, (2015)
- [4.37] Park, J. *et al.*, "Phase Diagram Reassessment of Ag–Au System Including Size Effect." *Calphad*, **32**, 135-141, (2008)
- [4.38] Nam, D. H. *et al.*, "Controlled Molybdenum Disulfide Assembly inside Carbon Nanofiber by Boudouard Reaction Inspired Selective Carbon Oxidation." *Adv. Mater.*, **29**, 1605327 (2017)
- [4.39] Nam, D.-H. *et al.*, "One-Step Structure Modulation of Electrospun Metal-Loaded Carbon Nanofibers: Redox Reaction Controlled Calcination." *Carbon*, **82**, 273-281, (2015)
- [4.40] Park, J. *et al.*, "Phase Diagram Reassessment of Ag–Au System Including Size Effect." *Calphad*, **32**, 135-141, (2008)

- [4.41] Nam, D. H. *et al.*, "Controlled Molybdenum Disulfide Assembly inside Carbon Nanofiber by Boudouard Reaction Inspired Selective Carbon Oxidation." *Adv. Mater.*, **29**, 1605327 (2017)
- [4.42] Yang, T. Y. *et al.*, "A New Hematite Photoanode Doping Strategy for Solar Water Splitting: Oxygen Vacancy Generation." *Phys. Chem. Chem. Phys.*, **15**, 2117-2124, (2013)
- [4.43] Lee, S. Y. *et al.*, "Copper Oxide Reduction Through Vacuum Annealing." *Appl. Surf. Sci.*, **206**, 102-109, (2003)
- [4.44] Poulston, S. *et al.*, "Surface Oxidation and Reduction of CuO and Cu₂O Studied Using XPS and XAES." *Surf. Interface Anal.*, **24**, 811-820, (1996)
- [4.45] Wu, F. *et al.*, "Indirect Phase Transformation of CuO to Cu₂O on a Nanowire Surface." *Langmuir*, **32**, 4485-4493, (2016)
- [4.46] Qiu, J. *et al.*, "Artificial Photosynthesis on TiO₂-Passivated InP Nanopillars." *Nano Lett.*, **15**, 6177-6181, (2015)
- [4.47] Zeng, G. *et al.*, "CO₂ Reduction to Methanol on TiO₂-Passivated GaP Photocatalysts." *ACS Catal.*, **4**, 3512-3516, (2014)
- [4.48] Zhang, Z. *et al.*, "Electrochemical Reduction Induced Self-Doping of Ti³⁺ for Efficient Water Splitting Performance on TiO₂ Based Photoelectrodes." *Phys. Chem. Chem. Phys.*, **15**, 15637-15644, (2013)
- [4.49] Amano, F. *et al.*, "Effect of Ti³⁺ Ions and Conduction Band Electrons on Photocatalytic and Photoelectrochemical Activity of Rutile Titania for Water Oxidation." *J. Phys. Chem. C*, **120**, 6467-6474, (2016)
- [4.50] Chen, Y. W. *et al.*, "Atomic Layer-Deposited Tunnel Oxide Stabilizes Silicon Photoanodes for Water Oxidation." *Nat. Mater.*, **10**, 539, (2011)

- [5.1] Luo, J. *et al.*, "Cu₂O Nanowire Photocathodes for Efficient and Durable Solar Water Splitting." *Nano Lett.*, **16**, 1848-1857, (2016)
- [5.2] Yang, T.-Y. *et al.*, "An Iron Oxide Photoanode with Hierarchical Nanostructure for Efficient Water Oxidation." *J. Mater. Chem. A*, **2**, 2297-2305, (2014)
- [5.3] Gelderman, K. *et al.*, "Flat-Band Potential of a Semiconductor: Using the Mott-Schottky Equation." *J. Chem. Educ.*, **84**, 685, (2007)
- [5.4] Alén, P. *et al.*, "Diffusion Barrier Properties of Atomic Layer Deposited Ultrathin Ta₂O₅ and TiO₂ Films." *J. Electrochem. Soc.*, **153**, G304, (2006)
- [6.1] Yang, T. Y. *et al.*, "A New Hematite Photoanode Doping Strategy for Solar Water Splitting: Oxygen Vacancy Generation." *Phys. Chem. Chem. Phys.*, **15**, 2117-2124, (2013)
- [6.2] Bosman, A. *et al.*, "Small-Polaron Versus Band Conduction in Some Transition-Metal Oxides." *Adv. Phys.*, **19**, 1-177, (1970)
- [6.3] Kennedy, J. *et al.*, "Photooxidation of Water at α -Fe₂O₃ Electrodes." *J. Electrochem. Soc.*, **125**, 709-714, (1978)
- [6.4] Lindgren, T. *et al.*, "Aqueous Photoelectrochemistry of Hematite Nanorod Array." *Sol. Energy Mater. Sol. Cells*, **71**, 231-243, (2002)
- [6.5] Dare-Edwards, M. *et al.*, "Electrochemistry and photoelectrochemistry of iron(III) oxide." *J. Chem. Soc. Faraday Trans. 1*, **79**, 2027-2041, (1983)
- [6.6] Horowitz, G. *et al.*, "Capacitance voltage measurements and flat-band potential determination on Zr-doped α -Fe₂O₃ single-crystal electrodes." *J. Electroanal. Chem.*, **159**, 421-436, (1983)
- [6.7] Sanchez, K. *et al.*, "The photoelectrochemistry of niobium doped α -Fe₂O₃." *J. Electroanal. Chem.*, **252**, 269-290, (1988)

- [6.8] Morin, F. *et al.*, "Electrical Properties of $\alpha\text{Fe}_2\text{O}_3$ and $\alpha\text{Fe}_2\text{O}_3$ Containing Titanium." *Phys. Rev.*, **83**, 1005-1010, (1951)
- [6.9] Chang, R. *et al.*, "Direct-Current Conductivity and Iron Tracer Diffusion in Hematite at High Temperature." *J. Am. Ceram. Soc.*, **55**, 211-213, (1988)
- [6.10] Glasscock, J. *et al.*, "Enhancement of Photoelectrochemical Hydrogen Production from Hematite Thin Films by the Introduction of Ti and Si." *J. Phys. Chem. C*, **111**, 16477-16488, (2007)
- [6.11] Hahn, N. *et al.*, "Photoelectrochemical Performance of Nanostructured Ti- and Sn-Doped $\alpha\text{-Fe}_2\text{O}_3$ Photoanodes." *Chem. Mater.*, **22**, 6474-6482, (2010)
- [6.12] Ling, Y. *et al.*, "The Influence of Oxygen Content on the Thermal Activation of Hematite Nanowires." *Nano Lett.*, **11**, 2119-2125, (2011)
- [6.13] Kumari, S. *et al.*, "Enhanced Photoelectrochemical Response of Zn-Dotted Hematite." *Int. J. Photoenergy*, **2007**, 87467, (2007)
- [6.14] Hisatomi, T. *et al.*, "ChemInform Abstract: Enhancement in the Performance of Ultrathin Hematite Photoanode for Water Splitting by an Oxide Underlayer." *Adv. Mater.*, **24**, 2699-2702, (2012)
- [6.15] Cesar, I. *et al.*, "Influence of Feature Size, Film Thickness, and Silicon Doping on the Performance of Nanostructured Hematite Photoanodes for Solar Water Splitting." *J. Phys. Chem. C*, **113**, 772-782, (2009)
- [6.16] Saremi-Yarahmadi, K. *et al.*, "Nanostructured $\alpha\text{-Fe}_2\text{O}_3$ Electrodes for Solar Driven Water Splitting: Effect of Doping Agents on Preparation and Performance." *J. Phys. Chem. C*, **113**, 4768-4778, (2009)
- [6.17] Meng, X. *et al.*, "Enhanced photoelectrochemical activity for Cu and Ti doped hematite: The first principles calculations." *Appl. Phys. Lett.*, **98**, 112104, (2011)

- [6.18] Gaudon, M. *et al.*, "Influence of Sn⁴⁺ and Sn⁴⁺/Mg²⁺ doping on structural features and visible absorption properties of α -Fe₂O₃ Hematite." *J. Solid State Chem.*, **183**, 2101-2109, (2010)
- [6.19] Ingler, W. *et al.*, "Photoresponse of Spray Pyrolytically Synthesized Magnesium-doped Iron (III) oxide (p-Fe₂O₃) Thin Films under Solar Simulated Light Illumination." *Thin Solid Films*, **461**, 301-308, (2004)
- [6.20] Velev, J. *et al.*, "Electronic and magnetic structure of transition-metal-doped α -hematite." *Phys. Rev. B: Condens. Matter Mater. Phys.*, **71**, 205208, (2005)
- [6.21] Cesar, I. *et al.*, "Translucent Thin Film Fe₂O₃ Photoanodes for Efficient Water Splitting by Sunlight: Nanostructure-Directing Effect of Si-Doping." *J. Am. Chem. Soc.*, **128**, 4582-4583, (2006)
- [6.22] Kay, A. *et al.*, "New Benchmark for Water Photooxidation by Nanostructured α -Fe₂O₃ Films." *J. Am. Chem. Soc.*, **128**, 15714-15721, (2006)
- [6.23] De Wit, J. *et al.*, "Surface instability and nonstoichiometry of α -Fe₂O₃." *J. Solid State Chem.*, **37**, 242-247, (1981)
- [6.24] Gardner, R. *et al.*, "The electrical properties of alpha ferric oxide-II." *J. Phys. Chem. Solids*, **24**, 1183-1186, (1963)
- [6.25] Merchant, P. *et al.*, "The electrical, optical and photoconducting properties of Fe_{2-x}Cr_xO₃ (0 \leq x \leq 0.47)." *J. Solid State Chem.*, **27**, 307-315, (1979)
- [6.26] Nagarajan, L. *et al.*, "A chemically driven insulator-metal transition in non-stoichiometric and amorphous gallium oxide." *Nat. Mater.*, **7**, 391-398, (2008)
- [6.27] Ling, Y. *et al.*, "The Influence of Oxygen Content on the Thermal Activation of Hematite Nanowires." *Angew. Chem., Int. Ed.*, **51**, 4074-4079, (2012)

- [6.28] Berry, F. *et al.*, "Rationalisation of defect structure of tin- and titanium-doped α -Fe₂O₃ using interatomic potential calculations." *Solid State Commun.*, **109**, 207-211, (1998)
- [6.29] Takano, M. *et al.*, "Characterization of fine particles of the α -Fe₂O₃-SnO₂ system with residual SO₄²⁻ ions on the surface." *J. Solid State Chem.*, **68**, 153-162, (1987)
- [6.30] Formal, F. *et al.*, "Controlling Photoactivity in Ultrathin Hematite Films for Solar Water-Splitting." *Adv. Funct. Mater.*, **20**, 1099-1107, (2010)
- [7.1] Yang, T.-Y. *et al.*, "An Iron Oxide Photoanode with Hierarchical Nanostructure for Efficient Water Oxidation." *J. Mater. Chem. A*, **2**, 2297-2305, (2014)
- [7.2] Bjorksten, U. *et al.*, "Photoelectrochemical Studies on Nanocrystalline Hematite Films." *Chem. Mater.*, **6**, 858-863, (1994)
- [7.3] Kennedy, J. H. *et al.*, "Photooxidation of Water at α -Fe₂O₃ Electrodes." *J. Electrochem. Soc.*, **125**, 709-714, (1978)
- [7.4] Morin, F. J., "Electrical Properties of α -Fe₂O₃ and α -Fe₂O₃ Containing Titanium." *Phys. Rev.*, **83**, 1005-1010, (1951)
- [7.5] Cherepy, N. *et al.*, "Ultrafast Studies of Photoexcited Electron Dynamics in γ - and α -Fe₂O₃ Semiconductor Nanoparticles." *J. Phys. Chem. B*, **102**, 770-776, (1998)
- [7.6] Dare-Edwards, M. *et al.*, "Electrochemistry and photoelectrochemistry of iron(III) oxide." *J. Chem. Soc. Faraday Trans. 1*, **79**, 2027-2041, (1983)
- [7.7] Lindgren, T. *et al.*, "Aqueous Photoelectrochemistry of Hematite Nanorod Array." *Sol. Energy Mater. Sol. Cells*, **71**, 231-243, (2002)
- [7.8] Gratzel, M., "Photoelectrochemical cells." *Nature*, **414**, 338-344, (2001)

- [7.9] Murphy, A. *et al.*, "Efficiency of solar water splitting using semiconductor electrodes." *Int. J. Hydrogen Energy*, **31**, 1999-2017, (2006)
- [7.10] Yang, T. *et al.*, "A new hematite photoanode doping strategy for solar water splitting: oxygen vacancy generation.", *Phys. Chem. Chem. Phys.*, **15**, 2117-2124, (2013)
- [7.11] Itoh, K. *et al.*, "Stacked thin-film photoelectrode using iron oxide." *J. Appl. Phys.*, **56**, 874-876, (1984)
- [7.12] Itoh, K. *et al.*, "Thin Film Photoelectrochemistry: Iron Oxide." *J. Electrochem. Soc.*, **131**, 1266-1271, (1984)
- [7.13] Tilley, S. *et al.*, "Light-Induced Water Splitting with Hematite: Improved Nanostructure and Iridium Oxide Catalysis." *Angew. Chem., Int. Ed.*, **49**, 6405-6408, (2010)
- [7.14] Dotan, H. *et al.*, "Probing the photoelectrochemical properties of hematite (α -Fe₂O₃) electrodes using hydrogen peroxide as a hole scavenger." *Energy Environ. Sci.*, **4**, 958-964, (2011)
- [7.15] Glasscock, J. *et al.*, "Enhancement of Photoelectrochemical Hydrogen Production from Hematite Thin Films by the Introduction of Ti and Si." *J. Phys. Chem. C*, **111**, 16477-16488, (2007)
- [7.16] Formal, F. *et al.*, "Passivating surface states on water splitting hematite photoanodes with alumina overlayers." *Chem. Sci.*, **2**, 737-743, (2011)
- [7.17] Wilhelm, S. *et al.*, "Semiconductor Properties of Iron Oxide Electrodes." *J. Electrochem. Soc.*, **126**, 419-423, (1979)

- [7.18] Zhong, D. *et al.*, "Photo-assisted electrodeposition of cobalt-phosphate (Co-Pi) catalyst on hematite photoanodes for solar water oxidation." *Energy Environ. Sci.*, **4**, 1759-1764, (2011)
- [7.19] Formal, F. *et al.*, "Controlling Photoactivity in Ultrathin Hematite Films for Solar Water-Splitting." *Adv. Funct. Mater.*, **20**, 1099-1107, (2010)
- [7.20] Hisatomi, T. *et al.*, "A Ga₂O₃ underlayer as an isomorphic template for ultrathin hematite films toward efficient photoelectrochemical water splitting." *Faraday Discuss.*, **155**, 223-232, (2012)
- [7.21] Hisatomi, T. *et al.*, "ChemInform Abstract: Enhancement in the Performance of Ultrathin Hematite Photoanode for Water Splitting by an Oxide Underlayer." *Adv. Mater.*, **24**, 2699-2702, (2012)
- [7.22] Seabold, J. *et al.*, "Efficient and Stable Photo-Oxidation of Water by a Bismuth Vanadate Photoanode Coupled with an Iron Oxyhydroxide Oxygen Evolution Catalyst." *J. Am. Chem. Soc.*, **134**, 2186-2192, (2012)
- [7.23] Vayssieres, L. *et al.*, "Controlled Aqueous Chemical Growth of Oriented Three-Dimensional Crystalline Nanorod Arrays: Application to Iron(III) Oxides." *Chem. Mater.*, **13**, 233-235, (2001)
- [7.24] Ling, Y. *et al.*, "The Influence of Oxygen Content on the Thermal Activation of Hematite Nanowires." *Nano Lett.*, **11**, 2119-2125, (2011)
- [7.25] Deng, J. *et al.*, "Ti-doped hematite nanostructures for solar water splitting with high efficiency." *J. Appl. Phys.*, **112**, 084312, (2012)
- [7.26] Golubko, N. *et al.*, "Hydrolysis of Titanium Alkoxides: Thermochemical, Electron Microscopy, Saxs Studies." *J. Sol-Gel Sci. Technol.*, **20**, 245-262, (2001)

- [7.27] Yoldas, B. *et al.*, "Hydrolysis of Titanium Alkoxide and Effect of Hydrolytic Polycondensation Parameters." *J. Mater. Sci.*, **21**, 1087-1092, (1986)
- [7.28] Iwanski, P., "The Photoelectrochemical Behavior of Ferric Oxide in the Presence of Redox Reagents." *J. Electrochem. Soc.*, **128**, 2128-2133, (1981)
- [7.29] Peter, L. *et al.*, "Kinetics of light-driven oxygen evolution at α -Fe₂O₃ electrodes." *Faraday Discuss.*, **155**, 309, (2012)
- [7.30] Formal, F. *et al.*, "The Transient Photocurrent and Photovoltage Behavior of a Hematite Photoanode under Working Conditions and the Influence of Surface Treatments." *J. Phys. Chem. C*, **116**, 26707-26720, (2012)
- [7.31] Peter, L. *et al.*, "Surface recombination at semiconductor electrodes: Part I. Transient and steady-state photocurrents." *J. Electroanal. Chem.*, **165**, 29-40, (1984)
- [7.32] Klahr, B. *et al.*, "Water Oxidation at Hematite Photoelectrodes: The Role of Surface States." *J. Am. Chem. Soc.*, **134**, 4294-4302, (2012)
- [7.33] Riha, S. *et al.*, "Atomic Layer Deposition of a Sub-Monolayer Catalyst for the Enhanced Photoelectrochemical Performance of Water Oxidation with Hematite." *ACS Nano*, **7**, 2396-2405, (2013)

요약(국문초록)

전이 금속은 오비탈 간에 작은 에너지 준위 차이를 보이는 d-오비탈에 전자를 가지고 있어 다양한 산화 수를 갖는다. 따라서 전이금속은 전자를 쉽게 잃거나 얻을 수 있는 산화/환원 특성을 지닌다. 이들 금속은 다양한 음이온과 결합하여 산화물, 질화물 및 황화물을 형성하며 다양한 재료 특성을 나타내는 다양한 조성을 갖는다. 특히 전이 금속 산화물은 산화 상태에 따라 다양한 밴드 구조를 나타내므로 광전기화학적 촉매로 널리 사용되고 있다. 전이금속 산화물의 산화 상태는 에너지 밴드의 위치에 의해 결정되는 광 생성전자의 포텐셜과 연결되어 있기 때문에 광전기화학적 촉매의 선택성과 활성에 결정적인 영향을 미친다. 광전기화학 에너지 변환 반응 중에서도 자연 광합성 과정을 모방하는 것이 빛과 물을 통하여 이산화탄소(CO_2)를 환원하여 연료를 생성하기 때문에 지구 온난화 문제의 궁극적인 해결책으로 여겨져 왔다. 그러나 수중 조건에서 CO_2 의 환원을 수행 할 때, CO_2 의 환원반응은 수소 발생반응과 경쟁해야 한다. 하지만, CO_2 환원의 반응속도 결정단계가 수소 발생반응보다 더 높은 산화/환원 전위를 갖기 때문에 CO_2 의 환원반응을 선택적으로 수행하는 것은 어렵다.

본 학위논문의 목적은 광전기화학적 CO_2 의 환원반응을 선택적으로 수행하기 위해서 전이금속 산화물의 산화 상태를 정확하게 제어하는 것이고, 활성물질의 활성도와 안정성을 최적화하기 위한 나노구조를 설계하는 것이다.

먼저 선택적인 CO_2 환원을 위한 1 차원 나노구조를 갖는 단일상 Cu_2O 나노섬유 광양극이 전기방사공정과 열역학적으로 프로그래밍된 소성 공정을 통하여 제작되었다. CO_2 환원 반응을 수소발생반응에 대하여 선택적으로 수행하기 위해서는 Cu_2O 나노섬유의 상을 CuO 와 같은 불순물 상이 없는 단일상으로 정밀하게 제어하여야 한다. 현재까지는 소성 공정 동안의 기상분위기는 정밀하게

제어되지 않았으며, 산화분위기는 대기압, 환원반응은 Ar 이나 H₂ 가스분위기의 양극단에서만 제어되었으며 이는 CuO 의 상이 섞이는 결과를 초래했다. 따라서, 본 연구에서 산화구리 나노섬유의 상은 열역학과 속도론을 고려한 나노스케일에서의 기상-고상 반응에 의하여 제어되었다. 구리의 산화상태간의 상 변화 구동력은 각 산화상태의 깃스 자유 에너지를 비교함으로써 계산된다. 계산으로부터, 단일상 Cu₂O 가 현실적인 시간 범위 내에서 형성될 수 있는 속도론적 공정 윈도우를 발견하였다. 또한, Cu₂O 나노섬유 전극의 광활성 및 안정성을 최적화하기 위해 Cu₂O 박막 하부 층과 TiO₂ 보호 층의 계층적 구조가 개발되었다. 결과적으로, 산화구리 나노섬유 전극의 산화상태를 조절하고 적절한 나노구조를 설계함으로써 수증 전해질에서 CO₂ 를 알코올로 93%의 패러데이 효율로 전환할 수 있었다.

다음으로, 나노구조화된 적철광(α -Fe₂O₃)의 산화상태를 제어하고 계층적 구조를 갖는 광음극을 개발하여 광전기화학적 CO₂ 환원반응의 짝반응인 물 산화반응(OER)을 효과적으로 수행하고자 하였다. 물 산화반응을 위한 적철광 광음극의 가장 중요한 과제 중 하나는 전기 전도도의 향상이다. 현재까지는 단점을 극복하기 위한 종래의 접근법은 이중의 도펀트를 도입하는 것이었다. 우리는 새로운 내부 도펀트 소스로서 산소 공공을 체계적으로 제어하고 주석(Sn)과 같은 외부 도펀트와의 상호작용을 연구했다. 이러한 이해를 바탕으로, 우리는 산소 공공의 생성이 적철광의 광활성을 현저하게 활성화시킬 수 있음을 보였다. 또한 우리는 적철광의 광활성을 더욱 개선하기 위하여 도핑되지 않은 적철광 하부층, 타이타늄(Ti)이 도핑된 적철광 나노로드, β 상 산화수산화철 상부층으로 구성된 계층적 구조를 개발하였다. 도핑되지 않은 적철광 하부층은 온셋 전위를 40 mV (0.84 V vs. RHE)만큼 음의 방향으로 이동시켰고, β 상 산화수산화철 상부층은 1.4 V vs. RHE 에서의 광전류 밀도를 1.83 mA cm⁻² 까지 향상시켰다.

본 연구는 전이금속 산화물의 산화 상태를 정밀하게 제어하기 위한 방법론과 나노구조 전극의 합리적인 설계방법 및 이들의 광전기 화학 반응의 활성 및 선택성에 대한 영향에 대한 유용한 정보를 제공한다.

표제어: CO₂ 환원, 물 산화, 산화(I) 구리, 산화(III) 철, 열역학적 계산, 상 제어, 계층적 구조, 나노구조

학 번: 2012-24154

Curriculum Vitae

Ho-Young Kang

EDUCATION

- 2012 ~2018 **Seoul National University, South Korea**
Seoul, Korea
Integrated course of mater's and the doctor's
Department of Materials science and Engineering
Advisor: Young-Chang Joo, Professor
- 2008~2012 **Seoul National University, South Korea** Seoul, Korea
B.S., Department of Materials science and Engineering

RESEARCH EXPERIENCES

- **Department of Materials Science and Engineering, Seoul National University**
Advisor: Young-Chang Joo
- ✓ Photoelectrochemical properties of transition metal oxide-based electrodes
 - Investigation of photoactivity and stability of photocathode and photoanode.
 - Electrochemical impedance spectroscopy for identification of equivalent circuit parameter of electrode.
 - Investigation of photocurrent transient to analyze the charge transfer.
- ✓ Synthesis process of nanostructured transition metal oxide photoelectrode
 - Electrospinning process for copper oxide

- Controlling the uniform nanofiber structure.
- Sputtering and ALD process for the underlayer and passivation layer.
- Spray pyrolysis process for the iron oxide
 - Fabrication of transition metal oxide with vertical nanosheet structure.
 - Conformal coating of transition metal oxide on nanorod structure.
- Hydrothermal process for iron oxyhydroxide
 - Hierarchical vertical nanorod structure with the underlayer and nano-dot.
 - Elemental doping process by modifying the precursor solution.
- ✓ Designing the redox reaction during the calcination
 - Thermodynamic calculation for each oxidation state of transition metal oxide.
 - Hierarchical vertical nanorod structure with the underlayer and nano-dot.
 - Elemental doping process by modifying the precursor solution.
 - Oxygen partial pressure control during calcination for the control of phase transformation.

AWARDS AND HONORS

2015	Outstanding Presentation Awards, SNU Materials Fair, Korea
2015	Best Poster Awards, Nano Korea 2015, Korea
2016	Silver Medal, Samsung HumanTech Paper Award, Korea
2018	Best Poster Awards, Nano Korea 2018, Korea

PROFESSIONAL ACTIVITIES

Feb. 2015 ~ Feb. 2018 **Mandatory Military Service**
 Technical Research Personnel

PUBLICATIONS

- **Ho-Young Kang**, Dae-Hyun Nam, Ki Dong Yang, Wonhyo Joo, Hoyoung Kwak, Hyung-Ho Kim, Sung Hyeon Hong, Ki Tae Nam, and Young-Chang Joo, “Synthetic Mechanism Discovery of Mono-Phase Cuprous Oxide for Record High Photoelectrochemical Conversion of CO₂ to Methanol in Water”, *In revision at ACS Nano*
- Dae-Hyun Nam, **Ho-Young Kang**, Jun-Hyun Jo, Byung Kyu Kim, Sekwon Na, Uk Sim, In-Kyoung Ahn, Kyung-Woo Yi, Ki Tae Nam, and Young-Chang Joo, “Controlled Molybdenum Disulfide Assembly inside Carbon Nanofiber by Boudouard Reaction Inspired Selective Carbon Oxidation”, *Advanced Materials*, 1605327 (2017)
- Han-Wool Yeon, Janghyun Jo, Hochul Song, Youngho Kang, Sekwon Na, Hyobin Yoo, Seung-Yong Lee, Haelim Cho, **Ho-Young Kang**, Jung-Kyu Jung, Seungwu Han, Miyoung Kim, Young-Chang Joo, “Cu Diffusion-Driven Dynamic Modulation of the Electrical Properties of Amorphous Oxide Semiconductors”, *Advanced Functional Materials*, 1700336 (2017)
- Yoo-Yong Lee, **Ho-Young Kang**, Seok Hyeon Gwon, Gwang Mook Choi, Seung-Min Lim, Jeong-Yun Sun, and Young-Chang Joo, “A Strain-Intensive Stretchable Electronic Conductor: PEDOT-PSS/Acrylamide Organogels”, *Advanced Materials*, **28**, 1636 (2016)
- Han-Wool Yeon, Seung-Min Lim, Jung-Kyu Jung, Hyobin Yoo, Young-Joo Lee, **Ho-Young Kang**, Young-Jin Park, Miyoung Kim, and Young-Chang Joo, “Structural-Relaxation-Driven Electron Doping in Amorphous Oxide

Semiconductors through the Increase in Concentration of Oxygen Vacancies in the Shallow-Donor State”, *NPG Asia Materials*, **8**, e250 (2016)

- Ji-Hoon Lee, Ji Woo Kim, **Ho-Young Kang**, Seul Cham Kim, Sang Sub Han, Kyu Hwan Oh, Se-Hee Lee, and Young-Chang Joo, “The effect of energetically coated ZrOx on enhanced electrochemical performances of Li(Ni_{1/3}Co_{1/3}Mn_{1/3})O₂ cathodes using modified radio frequency (RF) sputtering”, *Journal of Materials Chemistry A*, **24**, (2015)
- Ji-Hoon Lee, Tae-Youl Yang, **Ho-Young Kang**, Dae-Hyun Nam, Na-Rae Kim, Yoo-Yong Lee, Se-Hee Lee, and Young-Chang Joo, “Designing Thermal and Electrochemical Oxidation Processes for δ -MnO₂ Nanofibers for High-performance Electrochemical Capacitors”, *Journal of Materials Chemistry A*, **20**, (2014)
- Tae-Youl Yang[†], **Ho-Young Kang**[†], Kyoungsuk Jin, Ji-Hoon Lee, Uk Sim, Hui-Yun Jeong, Young-Chang Joo, and Ki Tae Nam, “An Iron Oxide Photoanode with Hierarchical nanostructure for Efficient Water Oxidation”, *Journal of Materials Chemistry A*, **2**, (2013)
- Tae-Youl Yang, **Ho-Young Kang**, Uk Sim, Young-Joo Lee, Ji-Hoon Lee, Byungjin Koo, Ki Tae Nam, Young-Chang Joo, “A New Hematite Photoanode Doping Strategy for Solar Water Splitting: Oxygen Vacancy Generation” *Physical Chemistry Chemical Physics*, **15**, 2117 (2013).

PRESENTATIONS IN INTERNATIONAL CONFERENCES

- **Ho-Young Kang**, Tae-Youl Yang, Uk Sim, Ki Tae Nam, Young-Chang Joo, “A New Hematite Photoanode Doping Strategy for Solar Water Splitting: Oxygen Vacancy Generation”, Materials Research Society (2012 MRS fall meeting), Boston, MA, USA (2013).
- **Ho-Young Kang**, Tae-Youl Yang, Kyoungsuk Jin, Young-Chang Joo, and Ki Tae Nam, “An Iron Oxide Photoanode with Hierarchical nanostructure for Efficient Water Oxidation”, Electrochemical Society (223th meeting), San Francisco, CA, USA (2013).
- **Ho-Young Kang**, Dae-Hyun Nam, Ki Tae Nam, Young-Chang Joo, “Synthetic Mechanism Discovery of Mono-Phase Cuprous Oxide for Record High Photoelectrochemical Conversion of CO₂ to Methanol in Water”, Materials Research Society (2018 MRS spring meeting), Pheonix, AZ, USA (2018).